NSF/CEE-82105

PB84-177120

PREDICTION OF FREE FIELD MOTIONS IN LARGE-SCALE EARTHQUAKE SIMULATIONS USING HIGH EXPLOSIVES

APPLIED RESEARCH ASSOCIATES, INC.

Engineering and Applied Science

50272-101

REPORT DOCUMENTATION PAGE	1. REPORT NO. NSF/CEE-82105	2.	3. Recipient's Accession No. PB84 177120

4. Title and Subtitle
Prediction of Free Field Motions in Large-Scale Earthquake Simulations Using Explosives

5. Report Date
October 1982

6.

7. Author(s)
D.W. Steedman, C.J. Higgins

8. Performing Organization Rept. No.

9. Performing Organization Name and Address
Applied Research Associates*
2101 San Pedro Boulevard N.E.
Suite A
Albuquerque, NM 87110

10. Project/Task/Work Unit No.

11. Contract(C) or Grant(G) No.
(C)
(G) CEE7923500

12. Sponsoring Organization Name and Address
Directorate for Engineering (ENG)
National Science Foundation
1800 G Street, N.W.
Washington, DC 20550

13. Type of Report & Period Covered

14.

15. Supplementary Notes
*Formerly Higgins, Auld & Associates, Inc.

16. Abstract (Limit: 200 words)

Procedures used to design large-scale earthquake ground motion simulations using high explosives are investigated. Results of finite difference wave propagation calculations are combined with previous results to better define the ground motion environment as a function of explosive array height and homogeneous site material properties. Further improvement is achieved through development of a technique by which shock response spectra, for both simulation and prototype earthquakes, may be estimated. The results of these analyses are used to synthesize data from the recent SIMQUAKE events. These events employed explosive arrays to expose large-scale structural models to an earthquake-like environment. Predictions and actual large-scale test data are compared and adjustments to and verifications of the phenomenology are made. The ability to predict the ground motion environment during such tests is thus improved.

17. Document Analysis a. Descriptors

Predictions
Earthquakes
Buildings
Earthquake resistant structures
Dynamic structural analysis
Explosives
Simulation

b. Identifiers/Open-Ended Terms

Ground motion
C.J. Higgins, /PI

c. COSATI Field/Group

18. Availability Statement	19. Security Class (This Report)	21. No. of Pages
NTIS	20. Security Class (This Page)	22. Price

(See ANSI-Z39.18) *See Instructions on Reverse*

OPTIONAL FORM 272 (4-77)
(Formerly NTIS-35)
Department of Commerce

TABLE OF CONTENTS

LIST OF FIGURES

Conversion factors for U.S. customary to metric (SI) units of measurements.

To Convert From	To	Multiply By
angstrom	meters (m)	1.000 000 X E -10
atmosphere (normal)	kilo pascal (kPa)	1.013 25 X E +2
bar	kilo pascal (kPa)	1.000 000 X E +2
barn	meter^2 (m^2)	1.000 000 X E -28
British thermal unit (thermochemical)	joule (J)	1.054 350 X E +3
calorie (thermochemical)	joule (J)	4.184 000
cal (thermochemical)/cm^2	mega joule/m^2 (MJ/m^2)	4.184 000 X E -2
curie	*giga becquerel (GBq)	3.700 000 X E +1
degree (angle)	radian (rad)	1.745 329 X E -2
degree Fahrenheit	degree kelvin (K)	$t_K = (t°f + 459.67)/1.8$
electron volt	joule (J)	1.602 19 X E -19
erg	joule (J)	1.000 000 X E -7
erg/second	watt (W)	1.000 000 X E -7
foot	meter (m)	3.048 000 X E -1
foot-pound-force	joule (J)	1.355 818
gallon (U.S. liquid)	meter^3 (m^3)	3.785 412 X E -3
inch	meter (m)	2.540 000 X E -2
jerk	joule (J)	1.000 000 X E +9
joule/kilogram (J/kg) (radiation dose absorbed)	Gray (Gy)	1.000 000
kilotons	terajoules	4.183
kip (1000 lbf)	newton (N)	4.448 222 X E +3
kip/inch^2 (ksi)	kilo pascal (kPa)	6.894 757 X E +3
ktap	newton-second/m^2 ($N-s/m^2$)	1.000 000 X E +2
micron	meter (m)	1.000 000 X E -6
mil	meter (m)	2.540 000 X E -5
mile (international)	meter (m)	1.609 344 X E +3
ounce	kilogram (kg)	2.834 952 X E -2
pound-force (lbs avoirdupois)	newton (N)	4.448 222
pound-force inch	newton-meter (N·m)	1.129 848 X E -1
pound-force/inch	newton/meter (N/m)	1.751 268 X E +2
pound-force/foot^2	kilo pascal (kPa)	4.788 026 X E -2
pound-force/inch^2 (psi)	kilo pascal (kPa)	6.894 757
pound-mass (lbm avoirdupois)	kilogram (kg)	4.535 924 X E -1
pound-mass-foot^2 (moment of inertia)	kilogram-meter^2 ($kg \cdot m^2$)	4.214 011 X E -2
pound-mass/foot^3	kilogram/meter^3 (kg/m^3)	1.601 846 X E +1
rad (radiation dose absorbed)	**Gray (Gy)	1.000 000 X E -2
roentgen	coulomb/kilogram (C/kg)	2.579 760 X E -4
shake	second (s)	1.000 000 X E -8
slug	kilogram (kg)	1.459 390 X E +1
torr (mm Hg, 0° C)	kilo pascal (kPa)	1.333 22 X E -1

*The becquerel (Bq) is the SI unit of radioactivity; 1 Bq = 1 event/s.
**The Gray (Gy) is the SI unit of absorbed radiation.

A more complete listing of conversions may be found in "Metric Practice Guide E 380-74," American Society for Testing and Materials.

SECTION I

INTRODUCTION

The design of structures to withstand the effects of earthquake-induced ground motion remains a major task facing the engineering profession. Such design may significantly reduce the loss of life and property which is expected should a large magnitude earthquake occur in a major metropolitan area. The primary approach to such design is, and should remain, analytical. However, current design techniques must be verified and/or improved through large-scale testing. Although such tests on all structures would prove to be infeasible, a more limited series of tests, on a range of generic facilities, would provide invaluable data concerning the dynamic analysis of engineering structures.

One method of determining response characteristics is through measurements during and observations after actual earthquakes. Such data has been obtained in the past and has, in many instances, uncovered serious deficiencies in design. An example of these deficiencies is provided by the failure of the Imperial County Services Building in the 15 October 1979 El Centro, California earthquake. This modern (c. 1971) structure failed to withstand a moderate (M_L = 6.6) earthquake to the degree expected (ref. 1).

However, the use of earthquakes to obtain data is severely limited due to the inability to control the location, time and frequency of their occurance. A program including active experimentation is the only means of obtaining a sufficient quantity of data to adequately enhance design methods. Through experimentation one may not only control the time and

place of events, but test event parameters may also be controlled. This would allow for the definition of the effects of changes in these parameters.

Recent workshops (refs. 2, 3, 4) have acknowledged the need for large-scale testing for the simulation of earthquake loads. Furthermore, a recent study (ref. 5) has underscored this need and has demonstrated the feasibility of maintaining a national program to meet this testing need. Simulation methods include field shaking mechanisms, shake tables, snap-back methods and explosives. This report deals with the latter of these methods.

Explosive simulation is particularly well suited for investigation of soil and soil-structure systems. Furthermore, previous analytical studies performed for the National Science Foundation (NSF) (ref. 6) and a series of field tests supported by the Electric Power Research Institute (EPRI) (refs. 7, 8) have shown this method to be a technically and economically feasible means for reproducing earthquake-like environments. However, continued application of the high explosvie technique requires that existing simulation design methods be verified and, where needed, improved. This improvement will help to insure that future experiments will achieve optimum results. Simulation design includes the determination of desired motion characteristics with regard to model scale, site characteristics and charge configuration.

The primary objective of this study is the improvement of high explosive earthquake simulation design techniques. The results of recent finite difference calculations and the analysis of data from the aforementioned EPRI experiments supplement the findings of previous studies (ref. 6) regarding the simulation design process. This report presents the resulting improvements in the understanding of earthquake simulation using

high explosives.

Section II of this report discusses the analysis of two-dimensional finite difference calculations. Section III addresses the synthesis of large-scale simulation data and calculations. Section IV introduces a technique for estimating earthquake and simulation shock response spectra. Concluding remarks are contained in Section V.

SECTION II

CALCULATION STUDIES

1. BACKGROUND

Much of the basis for the design of experiments using high explosives to create earthquake-like environments is discussed in reference 6. That study combined data from several explosive events with the results of numerous finite difference calculations to define simulation criteria and methods for predicting the simulation environment.

Two important characteristics of reference 6 must be noted when applying its results. The first is that all events referenced in the study occurred in a similar geologic setting, which may be described as homogeneous dry alluvium. The related finite difference analysis employed a material model representing this geology. This becomes an important limitation when applying these results to other sites.

The second characteristic of note is that all events but one were defense related. The simulation criteria for these events are considerably different than for earthquake simulation and the test design and resulting phenomonology are not fully characteristic of those required. The exception is the MINI-SIMQUAKE (MSQ) event which was designed for earthquake simulation. However, this was a small-scale event and since previous work in the defense industry has revealed many modeling inadequacies, direct extrapolation to the large-scale is not recommended without verification of phenomena.

This section of this report addresses the first of these shortcomings.

In the paragraphs that follow, the results of several finite difference calculations will be presented. These results partially address the problem of site applicability through the employment of several variations of the material property model. In addition, the results of the previous calculations were further analyzed in light of the newly available information. This analysis will also be presented.

The second shortcoming is addressed in a later section through analysis of a set of recently available data. These data are taken from measurements from a series of tests, SIMQUAKE (SQ) (refs. 7, 8). These tests, sponsored by the Electric Power Research Institute, were the first explosive events conducted expressly for subjecting large-scale models to simulated earthquake motions.

2. CALCULATIONAL ANALYSIS

a. Basis for Analysis - The computational analysis involved studies of the results of finite difference wave propagation calculations. TOODY (ref. 9), a two-dimensional finite continuum code, was utilized to perform these calculations. Although TOODY and similar computer programs possess inherent shortcomings due to their two-dimensional nature, they may still provide invaluable assistance in the analysis of complex problems. The results of such calculations will not be viewed as quantitatively accurate. However, if carried out properly, and if reasonable judgement is applied, such calculations can yield relevant information concerning the relative effects of parametric variations.

The large number of parameters involved in this class of problem (for example, those related to simulation geometry, explosive input and material

model) dictates the calculation approach. On the one hand, clear analytic relationships are not evident where many parameters are involved, thus suggesting the need for experimentation. On the other hand, the expense in time and money required to field individual tests make it prohibitive to perform significant parametric analyses. Calculational analysis is viewed as an alternative approach to experimentation.

If, as suggested above, proper judgement is maintained, numerical results from computer calculations can be considered to yield data. This "calculational data" can then be treated as though it were experimental data to obtain adequate qualitative results in parametric analyses. That is, the form and relative magnitudes of the results will yield correct information regarding the effects of those parameters studied. These results can then be correlated with actual test data, such as that from SIMQUAKE, to provide quantitative corrections.

b. Dimensional Analysis - The experimental approach to investigation attempts to determine physical relationships through the controlled variation of important parameters. Insight into the parameters which govern those relationships may be gained through the technique of dimensional analysis. This technique is discussed in detail in references 10, 11 and 12 and only a brief discussion is presented here.

Dimensional analysis considers that, in general, most of the parameters dealt with in the physical sciences depend in magnitude upon the scale used to measure them. Such parameters are classed as dimensional quantities. In addition to these, another class of quantities, called dimensionless quantities, are independent of the system of measurement. It is the aim of dimensional analysis to express the parameters of a given situation in terms

of these independent, dimensionless quantities.

This goal may be achieved by first noting that, generally, the establishment of units for three physical quantities is sufficient to define all others. These three quantities are force (F), length (L) and time (T). (A fourth quantity, temperature, is sometimes included. However, this quantity does not affect the situation under study here and is neglected.) These three quantities are termed fundamental units. Other units, called derived units, are a combination of these fundamental units. For example, velocity may be expressed in terms of length and time, i.e. L/T^2.

Physical laws are functions of the parameters involved and are independent of the system of measurement. It follows that they may be represented by dimensionless quantities. These dimensionless quantities are determined through combinations of the basic physical parameters which characterize the situation. These combinations may be found to be of the form

$$\text{dimension of quantity} \stackrel{d}{=} [F]^a [L]^b [T]^c \qquad (1)$$

where $\stackrel{d}{=}$ indicates dimensional equivalence, [ ] indicate the dimension of a quantity and the exponents, a, b and c, are equal to zero. Buckingham's Pi theorem (ref. 13) then states that for n independent parameters governing a problem, there exist m dimensionless, or π, terms which are independent products of the original n parameters. It is further shown that the value m varies from n by a value k, where k is the number of fundamental units, i.e. $m = n - k$.

The formulation of a complete set of dimensionless terms requires the inclusion of all parameters involved in the phenomena, even those which are constant. The full set of π-terms may then be derived either by inspection or through use of the statement of dimensional homogeneity (equation 2).

$$[A_1]^{a_1}\,[A_2]^{a_2}\ldots[A_n]^{a_n} \stackrel{d}{=} [F]^0\,[L]^0\,[T]^0 \qquad (2)$$

This statement says that a set of terms may be derived from the original parameters which are equivalent as a set and are dimensionless. A particular list of π-terms will change as the specific situation changes. For example, different explosive geometries, illustrated in figure 1, are described by different sets of physical quantities. Furthermore, it is considered that any combination of dimensionless terms provides additional dimensionless terms beyond the original m independent quantities.

The study of reference 6 identified the planar explosive case as the most effective for earthquake simulation. Table 1 lists the parameters which were identified for this case. The parameters are defined in figures 2, 3 and 4 which illustrate, respectively, test geometry, explosive source and material parameters. Identification of these parameters allows for the derivation of a list of π-terms as presented in table 2. These are the terms which guide the formulation of calculational experiments and data analysis.

c. Previous Calculations - In addition to identifying the applicability of the planar explosive geometry, previous work has determined other important parametric relationships. Using WONDY (ref. 14), a

TABLE 1

LIST OF PARAMETERS DEFINING EARTHQUAKE SIMULATION ENVIRONMENT

Parameter	Symbol	Dimensions
Source		
Yield	W, γ or α	FL, FL/L or FL/L^2
Pressure	P_o	F/L^2
Geometry		
Array Height	H	L
Surcharge Height	S	L
Range to Target	R	L
Depth to Target	Z	L
Soil		
Density	ρ	FT^2/L^4
Elastic Wave Speed	C_1	L/t
Elastic Limit	ρ_1	E/L^2
Loading Wave Speed	C_2	L/T
Unloading Wave Speed	C_3	L/T
Poisson's Ratio	ν	---
Cohesion Intercept	K	F/L^2
Yield Surface Slope	β	---
Von Mises Limit	Y_M	F/L^2
Tensile Cutoff	P_T	F/L^2
Dependent Variables		
Peak Stress	σ	F/L^2
Peak Particle Acceleration	a	L/T^2
Peak Particle Velocity	v	L/T
Peak Displacement	d	L
Characteristic Times	t	T

TABLE 2

LIST OF π-TERMS FOR EARTHQUAKE SIMULATION

Source and Geometry	Target Point Location
$H\ (\frac{P_o}{\alpha})$	$R\ (\frac{P_o}{\alpha})$
$\frac{S}{H}$	$\frac{Z}{H}$
Soil Model	**Dependent Parameters**
$\frac{\rho C_1^2}{P_o}$	$\frac{\sigma}{P_o}$
$\frac{P_1}{P_o}$	$\frac{a}{C_1^2}\ (\frac{\alpha}{P_o})$
$\frac{C_2}{C_1}$	$\frac{\rho C_1 v}{P_o}$
$\frac{C_3}{C_1}$	or $\frac{\rho C_1^2 d}{\alpha}$
ν	$C_1 t\ (\frac{P_o}{\alpha})$
$\frac{K}{P_o}$	
β	
$\frac{Y_M}{P_o}$	
$\frac{P_I}{P_o}$	

one-dimensional finite difference wave propagation code, and TOODY, spherical and cylindrical, as well as planar, geometries were calculationally simulated to study several parameters.

For example, spherical calculations verified standard explosive scaling relationships as suggested by Crowley (ref. 15). The scaling term in this case is $W^{1/3}$ where W is the explosive yield in, for example, kg of TNT. (In the strict sense, charge is actually an energy term [FL] rather than a mass. However, energy is related to the charge amount by a constant which varies for different explosive types and the charges discussed in this report have been normalized to TNT. It may be noted in tables 1 and 2, though, that the dimensional analysis included energy units.) These calculations also defined spherical attenuation rates.

Cylindrical calculations, similarly, verified charge scaling and defined cylindrical attenuation rates. For this geometry, the lineal charge density, $\gamma \stackrel{d}{=}$ [FL/L], scales to the one-half power, $\gamma^{1/2}$. These calculations also determined source coupling effects where changes in cavity radius caused a change in initial energy per unit mass and an accompanying change in peak cavity pressure. Effects of a finite explosive length were also studied. Material property scaling relationships were determined and are summarized below:

Radial Stress: $\frac{\sigma}{P_o}$

Radial Velocity: $\frac{\rho C_L v}{P_o}$

Radial Displacement: $\frac{\rho C_L^2 d}{\gamma^{1/2}}$

Range: $R/\gamma^{1/2}$

where

σ = radial stress

v = radial partial velocity

d = radial displacement

ρ = material mass density

C_L = material loading wave speed

γ = lineal charge density

P_o = peak source pressure

The third explosive configuration, the planar array, was the subject of extensive analysis. The charge in this case is expressed as areal charge density, $\alpha \triangleq \frac{d}{} [FL/L^2]$, and scales to the first power. Yield scaling, array height effects, and motion away from the array centerline were studied. Free surface effects received preliminary review but a more indepth analysis was performed in this more recent study and will be presented later.

d. Synthesis of Data and Calculations - The results of the planar calculations were compared to the data from MINI-SIMQUAKE (MSQ). This test was a double array planar explosive event and, although small-scale, the event provided data generated with the aim of simulating an earthquake environment. The data from this event were cast in forms determined by the calculations and were compared to predictions based on the calculations.

The calculations were shown to reasonably predict the form of the data. Slight adjustments in magnitude were needed for the relationships to agree with the data and these adjusted fits, along with the MSQ data, are presented in figures 5 through 7. Equations 3 through 5 below define these fits and were, to this point, considered as predicting array middepth peak horizontal motions in dry alluvium. Details of the material model used in these calculations to represent the MSQ test site, McCormick Ranch, will be provided later.

$$a \cdot \alpha = 1197\ (R/\alpha)^{-0.89} \qquad \text{for } R/\alpha \leq 0.659\ (H/\alpha)^{0.6} \tag{3a}$$

$$a \cdot \alpha = 525.2\ (H/\alpha)^{1.21}\ (R/\alpha)^{-2.9} \qquad \text{for } R/\alpha > 0.659\ (H/\alpha)^{0.6} \tag{3b}$$

$$v = 9.58\ (R/\alpha)^{-0.16} \qquad \text{for } R/\alpha \leq 0.687\ (H/\alpha)^{0.52} \tag{4a}$$

$$v = 4.51\ (H/\alpha)\ (R/\alpha)^{-2.1} \qquad \text{for } R/\alpha > 0.687\ (H/\alpha)^{0.52} \tag{4b}$$

$$d/\alpha = 0.078\ (R/\alpha)^{-0.12} \qquad \text{for } R/\alpha \leq 0.575\ (H/\alpha)^{0.75} \tag{5a}$$

$$d/\alpha = 0.031\ (H/\alpha)^{1.28}\ (R/\alpha)^{-1.82} \qquad \text{for } R/\alpha > 0.575\ (H/\alpha)^{0.75} \tag{5b}$$

where

a = acceleration, g's

v = velocity, m/s

d = displacement, m

R = range, m

α = areal charge density, kg/m^2 of TNT

Note that the terms in the equations are not dimensionless and that terms which were constant in all calculations (e.g. P_o) were omitted.

e. Discussion of Past Results - Prior to the presentation and discussion of recent findings, some general observations of these past

results deserve mention. These relate to the trends which reveal themselves in the calculational results and in the test data. Specifically, the results indicate distinct portions of data with increasing scaled range. These portions are manifestations of differing rates of attenuation of the propagating loading waves.

The first, near range, change in slope is believed to be due to relief effects. Figures 8 and 9 will aid in understanding this concept. Figure 8 illustrates the wavefronts which will be generated by the explosion of a planar array with the arrows indicating the direction of particle motion upon arrival of a particular wavefront. (The fronts would be similar when viewing the array in a length cross-section). In near range, the initial wave fronts control motion and the environment most nearly represents a planar propagating wave. This planar region is represented by the first slope in figure 9.

With range, however the relief waves from the bottom of the array will come to have a significant effect on the motion as they overtake the loading wave. This phenomenon occurs in inelastic media where the P-wave propagates at the material loading wave speed. The P-relief wave, however, propagates at the seismic wave speed, generally about double the loading velocity (ref. 16). One may deduce by inspection that the effect will be to reduce the peak motion. At this point, the motion is indicative of the effects of finite explosive height. Thus, the second region of the plot is denoted as the cylindrical region. In the dimension along the width of the array, a similar effect would occur as related to finite explosive width and a spherical region, in this hypothetical case, would be observed. One would not expect to note this spherical region in two-dimensional calculations.

However, a third region of attenuation does appear in the two-dimensional results. This region, though, shows decreased, rather than increased, rates of attenuation. This phenomenon is believed to be caused by elastic effects. In this case, the loading beyond some range will be fully elastic for the material. The consequence would be less dissipation of energy and, hence, reduced rates of attenuation. This reasoning is supported by inspection of computed velocity waveforms. Figure 10 shows velocity waveforms computed by the TOODY code within the second and third regions, respectively. Note that in figure 10b, in contrast to figure 10a, the loading portion remains within the initial elastic slope of the material. Additionally, the velocity magnitude at the second transition range may be shown to agree with the relation

$$P_1 = \rho C_i v \tag{6}$$

found in, for example, reference 16. In this relation, P_1 is the material elastic cutoff in the hydrostat and the other parameters are as defined previously.

Finally, it should be noted that the data plots fail to reveal this third attenuation region. It is hypothesized that in the actual, three-dimensional case, the spherical relief phenomenon is superimposed by the opposing effect of elastic attenuation. Therefore, motion prediction equations 3 through 5 provide models for only the planar and cylindrical regions and neglect the third region of attenuation evident only in the calculations. These results encouraged continued application of this method

of analysis. Hence, it was employed in the study discussed in the ensueing paragraphs.

3. RECENT STUDY

The parametric analysis begun in previous work was continued in this study. The prospect of the continued use of the explosive simulation technique dictates the need for a more general definition of the ground motion environment. In particular, an understanding of the effects of geologic setting on this environment is critical to the development of the test method. This section describes the analysis of the results of several TOODY calculations in which the material model was varied through a range of probable properties. Additional calculations were performed to check and improve past results by repeating the symmetric cases studying array height effects.

a. Calculation Check - The calculation duplication was performed to ensure a common base between past and present analyses. The details of the calculations are discussed thoroughly in reference 6 and only a brief discussion will be presented here. The primary calculation input variables relate to the element mesh, the explosive source and the material model.

The general case of element mesh for two-dimensional planar array calculations is illustrated in figure 11. The basic charateristics of this set-up are:

- The mesh is symmetric about the array middepth to avoid the effects of a free surface
- The mesh in the region nearest the array provides a sufficient density of target points in both range and depth

- The overall dimensions of the grid are sufficiently large to avoid the effects of boundary reflections on the motions of interest

The second input variable, explosive source, was modeled in TOODY by a pressure boundary. Through this pressure boundary, a specified loading is applied to the elements adjacent to that boundary thus causing a loading wave to be propagated, numerically, through the mesh. The calculations discussed herein employed a pressure-time history to load the elements along the simulated explosive length. This loading history was derived through studies using the WONDY code by modeling ideal gas in cavities to achieve loading histories related to explosive densities. Pressure-time histories calculated within the cavities were modified to account for two-dimensional effects. The loading used in this study is as shown in figure 3 setting P_o = 15.77 MPa and t_o = .07 sec.

Further definition of the pressure boundary was required. A calculation time step problem arises in the zones immediately below the explosive where a loading discontinuity occurs. A rapid decrease in time step prevents the calculations from continuing through to the late times of interest. The instability was overcome by applying a pressure along the remainder of this boundary equal to the stress calculated within the adjacent material element along that boundary in the previous time step.

Finally, the material model must be developed for TOODY in the form of a loading hydrostat and a failure envelope of the Mohr-Coulomb type. These were defined in figures 4a and 4b regarding dimensional analysis. A brief discussion of these follows.

Figure 4a represents the Drucker-Prager generalization of the Mohr-Coulomb failure envelope. The envelope relates the square root of the

second invariant of the stress deviator tensor, $\sqrt{J_2'}$, to the pressure, p. These parameters may be computed from the standard triaxial test by

$$\sqrt{J_2'} = \frac{1}{\sqrt{3}} (\sigma_1 - \sigma_3) \tag{7}$$

$$p = \frac{1}{3} (\sigma_1 + 2\ \sigma_3) \tag{8}$$

where σ_1 = vertical stress in the triaxial test

σ_3 = confining stress in the triaxial test

These parameters are related by the expression

$$\sqrt{J_2'} = k + \alpha\ p \tag{9}$$

where k and α are as defined in the figure. At high pressures, $\sqrt{J_2'}$ is usually considered to reach a constant known as the Von Mises limit, Y_M in figure 4a. The failure envelope may be used to check and, if necessary, correct computed deviator stress values.

The other portion of the material model is the hydrostat shown in figure 4b. Ordinarily, though, laboratory or field data on hydrostatic behavior do not exist. Rather, seismic velocity data and/or laboratory uniaxial strain data are typically available. However, uniaxial response may be converted to the hydrostatic case using Poisson's ratio, ν, and the failure surface. The following procedure, may be used to accomplish this. Equations 10 and 11 relate pressure to axial stress, σ_a, and relate excess compression, μ, to axial strain, ϵ_z, up to the point of failure.

$$p = \frac{1}{3}\left(\frac{1 + \nu}{1 - \nu}\right)\sigma_a \tag{10}$$

$$\mu = \frac{\varepsilon_z}{1 - \varepsilon_z} \tag{11}$$

Failure may be checked by comparing the respective values of $\sqrt{J_2'}$ as computed from the failure surface and as computed from the uniaxial test using the relation

$$\sqrt{J_2'} = \frac{1}{\sqrt{3}}\left(\frac{1 - 2\nu}{1 - \nu}\right)\sigma_a \tag{12}$$

where σ_a is as computed for the given value of p using equation 10. If the former value is the lesser of the two, failure has occurred and a new uniaxial stress is computed as

$$\sigma_a = \frac{2}{3}\sqrt{3J_2'} + p \tag{13}$$

The corresponding uniaxial strain may be found and used to compute the excess compression, equation 11, associated with the value of p.

The material model used for the calculation check was that for dry McCormick Ranch silty-sand as modeled in the original calculations. This choice was made to provide a base for comparison among the past and present parametric studies and because McCormick Ranch was the site of the SIMQUAKE experiments. The model used to represent this site is discussed below.

The McCormick Ranch model was originally selected because much of the

existing explosive simulation data are from McCormick Ranch and because the site was a prime candidate for earthquake simulation experiments. This was, in fact, the site for the large-scale SIMQUAKE experiments. Soil data for the site are available from references 17, 18, and 19 and from unreported tests performed at the New Mexico Engineering Research Institute (NMERI, formerly CERF).

The site, above about 23 meters, consists mainly of silty, clayey fine sand (USCS classification SM and SC) with light cementation throughout. There are some gravel and hard caliche lenses as well as a few layers of plastic silts and clays but these conditions occur seldomly and the site is quite uniform overall. Air-bailed, dry drill holes remain open without support in this material but undisturbed samples are difficult to obtain. The soil below 23 meters is a clean uniform sand. Most simulation tests have been performed above this material and, therefore, its properties have not been determined. The ground water table at the site is below 150 meters.

A representative seismic profile for the site is given in table 3. The seismic velocity gradually increases from 400 m/sec to 670 m/sec from the surface to 4.25 meters below the surface and then remains 670 m/sec to a depth of 26 meters, indicating the relative uniformity of the upper silty sand. The increase in seismic velocity at 26 meters is probably associated with the uniform sand layer. The data of reference 18 indicate that the average dry density in the upper 15 meters is about 1639 kg/m^3 and the average moisture content is about 6.5 percent. These values combine to give an average mass density of 1746 kg/m^3.

TABLE 3

Representative Seismic Profile for McCormick Ranch Test Site (ref. 17)

Depth (m)	Seismic Velocity (m/sec)
0-1	400
1-4.25	530
4.25-26	670
26-79	1140
79 and Below	1860

The uniaxial stress-strain model for this site (figure 12) was derived by assuming a seismic modulus (taking 503 m/sec as an average velocity in the upper material) to the 0.69 MPa stress level and then softening the model to correspond to a modulus based upon one-half the seismic velocity. Unloading is assumed to occur at the seismic modulus. This seismic-based model was used in the calculations which investigated array height variations.

Failure data was available from triaxial tests reported in reference 18 and from other unreported results from NMERI. Figure 13 presents the fit to the data in terms of $\sqrt{J_2'}$ versus p as used in this model.

As mentioned earlier, the material model for the calculations requires input in terms of a hydrostat and a yield surface. The uniaxial fit of figure 12 was converted to a hydrostat assuming a Poisson's ratio of 0.3 and using the failure envelope in figure 13. This hydrostat is shown in figure 14.

The calculation set-up, as just described, was employed to reevaluate the array height study of reference 6. Array height effects were studied by varying the number of loaded zones. The material model and the pressure-

time history remained constant throughout the calculations but changes in the element grid were affected where necessary to accommodate the geometry of each case. Minor alterations relative to the earlier study allowed for better calculation stability at later times and, thus, were used. The subsequent results are presented in figures 15 through 17 while equations 14 to 16 describe these curves and replace the relationships presented earlier. These results are similar in character to the results they replace but differ slightly in magnitude and exact shapes.

$$a.\alpha = 4980\ (R/\alpha)^{-0.57} \qquad \text{for } R/\alpha \leq 0.533\ (H/\alpha)^{0.406} \qquad (14a)$$

$$a.\alpha = 1110\ (H/\alpha)^{1.01}\ (R/\alpha)^{-3.00} \qquad \text{for } R/\alpha > 0.533\ (H/\alpha)^{0.406} \qquad (14b)$$

$$v = 18.9\ (R/\alpha)^{-0.164} \qquad \text{for } R/\alpha \leq 0.763\ (H/\alpha)^{0.407} \qquad (15a)$$

$$v = 1150\ (H/\alpha)^{0.856}\ (R/\alpha)^{-2.34} \qquad \text{for } R/\alpha > 0.763\ (H/\alpha)^{0.407} \qquad (15b)$$

$$d/\alpha = 0.068\ (R/\alpha)^{-0.145} \qquad \text{for } R/\alpha \leq 0.581\ (H/\alpha)^{1.72} \qquad (16a)$$

$$d/\alpha = 0.030\ (H/\alpha)^{1.06}\ (R/\alpha)^{-1.58} \qquad \text{for } R/\alpha > 0.581\ (H/\alpha)^{1.72} \qquad (16b)$$

where

a = peak particle acceleration, g's

v = peak particle velocity, m/s

d = peak particle displacement, m

R = range, m

H = array height, m

α = areal charge density, kg/m^2 of TNT

b. Material Property Variations - The above results are applicable

only for sites similar to that modeled, i.e. uniform dry alluvium. One of the primary objectives of this study was to widen the application of the simulation design technique. That is, to expand the range of materials and, hence, the possible test sites, for which results may be predicted. This goal was approached through changes in the hydrostat and in the yield surface.

The dimensional analysis indicated the variables which relate to material characterization. The number of parameters does not allow that each be investigated in a study of this scope. Therefore, those parameters which were believed to most govern the motion environment were investigated. This parametric investigation was similar to that for array height but array height, rather than material model, was held constant throughout this portion of the study.

Regarding the hydrostat, the loading wave speed is believed to be a controlling variable. Variations of other parameters, e.g. P_1 and relative shape of loading and unloading portions, would effect the environment also and deserve study. However, these effects are probably secondary and were not subject to analysis here. The wave speed changes were actually approached using the uniaxial case with subsequent conversion to the hydrostat. This is because the uniax is the curve which is most often encountered. This presentation, and the related seismic wave speed, is the more familiar form of viewing data.

Three uniaxial loading curves were selected for study. One, of course, being the McCormick Ranch uniax utilized in preceding study. This uniax was discussed in detail earlier and needs no further definition. Two other cases were modeled. These hypothetical cases were chosen to provide a wide,

yet realistic, range of wave speeds. The uniaxial curve for each of these models is illustrated in figure 18. Noting that wave speed is directly proportional to material modulus (i.e. $v = \sqrt{E/\rho}$), three different material stiffnesses, and wave speeds, have been chosen.

Specifically, the McCormick Ranch model (U_1) with seismic wavespeed, C_p = 503 m/s was developed from a measured velocity and is typical of dry silty sand. A second uniax, designated U_2, is developed based on a C_p equal to 305 m/s. This value is typical of loose soils (ref. 16). A third, stiff, uniax uses a seismic wave speed of 1676 m/s typical of wet, compacted or cemented soils (ref. 16) and is designated U_3.

The remainder of the shape of the uniaxial models was developed to remain consistent with observations of the related hydrostat. Data has shown (ref. 16) that, in general, the wave speed at which a material is loaded, C_L, is about one-half the material elastic wave speed, C_i. Furthermore, the unloading wave speed, C_u, is generally about equal to the elastic wave speed. Each of the uniaxial models reflect those generalizations. Also, the elastic limit, P_1, was held constant to maintain consistent shape of the uniax and hydrostat among the calculations.

Several other parameters identified in the dimensional analysis were left unchanged through these calculations. This was necessary to properly study stiffness variations. These parameters include mass density, Poisson's ratio and the failure surface characteristics. The values used were those identified for the McCormick Ranch model. A variation in failure surface was later investigated and will also be presented.

Since the TOODY program requires input in the form of a hydrostat, the uniaxial curves necessitated conversion to that form of loading surface.

The technique described previously was employed using the McCormick Ranch failure surface to convert the soft, U_2, and the stiff, U_3, uniax curves to soft, H_2, and stiff, H_3, hydrostats. The McCormick Ranch hydrostat, H_1, was found earlier. Figure 19 presents these models. The figure also shows a fourth hydrostat, H_4, which was developed for a preliminary study of failure surface effects. This case employed a failure surface similar to the McCormick Ranch model, but with a reduced K value (figure 20), with the McCormick Ranch uniax. Table 4 summarizes the material models.

c. Material Property Results - A series of three calculations was performed to investigate stiffness effects. The calculations used each of the three different stiffness models and the calculation set-up as described. In summary, a 6.1 m array was modeled in rectangular, two dimensional geometry. The calculation assumed a line of symmetry about the middle of the array to eliminate interference from free surface effects. The pressure-time function, figure 3, was applied over one-half the modeled array height, or 3 m, to simulate a detonation of TNT at a 17.49 kg/m^2 charge density. Figures 21 through 23 present the peak calculated motions expressed in the form shown in figures 5 through 7.

An in depth study was undertaken to determine forms for the motion parameters which would collapse the data. This type of study calls for a review of the dimensional analysis and for noting the general trends of the data. The original terms involving dependent parameters are repeated below. These are:

radial acceleration: $\dfrac{a\alpha}{C_L^2 P_o}$

TABLE 4

SUMMARY OF MATERIAL PROPERTIES USED IN TOODY CALCULATIONS

Parameter	Calculation			
	McCormick Ranch* (MAT 1)	P20S.2 (MAT 2)	P20S.3 (MAT 3)	P20S.4 (MAT 4)
$\rho(kg/m^3)$	1746	1746	1746	1746
ν	0.3	0.3	0.3	0.3
$C_P(m/s)$	503	305	1676	503
$C_L(m/s)$	155.7	94.3	518.9	251.5
$C_u(m/s)$	245.1	148.5	1382.3	396
$C_{L1}(m/s)$	122.6	74.3	691.5	198
$C_{L2}(m/s)$	136.8	74.3	408.6	221
B(MPa)	273.1	100.4	3034.	273.1
$P_1(P_a)$	42.7	42.7	42.7	42.7
$P_t(P_a)$	-62	-62	-62	-62
$K(P_a)$	48.2	48.2	48.2	24.1
β	0.22	0.22	0.22	0.22
$Y_M(MP_a)$	200	200	200	200

*McCormick Ranch model used for symmetrical cases P5S (3 m array), P20S.1 (12.2 m array), P40S (24.4 m array) and P80S (48.8 m array)

radial velocity: $\frac{\rho C_L v}{P_o}$

radial displacement $\rho C_L^2 \frac{d}{\alpha}$

These terms, which include material property parameters for motion, were plotted versus range. Range was already expressed in the original form.

$$\frac{R}{\alpha} (P_o)$$

(Recall that P_o, a constant, had been omitted from the range term.) Although these plots provided some insight into the stiffness effects, the data did not adequately collapse.

The investigation then turned to inspection of the waveforms. Any trend which may be discerned therefrom could provide insight into parametric effects. In figure 24 the time-domain waveform is characterized by three times. These characteristic times are the outward (positive) phase duration (t_{pd}), the time to positive peak (t_{pp}) and the duration of the total wavelength (t_T).

The positive phase duration of the computed velocity waveform is a function of material model and of array height. Figure 25 illustrates this fact for material property variations showing calculated t_{pd} values versus range. The trend was similar for array height variation. Noting these findings, the dimensional parameters were manipulated to obtain appropriate scaling terms. These terms summarized below were completed for each calculation and plotted in figure 26.

$$C_L t_{pd} \quad \frac{P_o}{\alpha}$$

and

$$\rho C_L^2 \frac{H}{\alpha}$$

Eliminating constant terms ρ and P_o yields the terms shown in the figure which relates positive phase duration to array height and material loading wave speed. The results are characterized by equation 17.

$$\frac{C_L \ t_{pd}}{\alpha} = 0.059 \left(\frac{H \ C_L^2}{\alpha} \right)^{0.33} \tag{17}$$

Such a trend in waveforms suggests interdependence between the phase duration and peak amplitudes of particle motion.

This insight was used to establish new π-terms which were found to collapse the data very well. These new terms are summarized below:

$$\frac{\sigma}{P_0}$$

$$\rho \ C_L \ t_{pd} \frac{a}{P_o}$$

$$\frac{\rho \ C_L \ v}{P_o}$$

$$\frac{\rho \ C_L \ d}{P_o \ t_{pd}}$$

Elimination of the constant P_o term in each case yields the terms which were plotted. These are

peak stress: σ

peak radial acceleration: $\rho\ C_L\ t_{pd}\ a_H$

peak radial velocity: $\rho\ C_L\ v_H$

peak radial displacement: $\rho\ C_L\ d_H/t_{pd}$

Finally, the range term

$$\frac{R}{C_L\ t_{pd}}$$

was formulated to reflect the time dependence. Figures 27-30 show these results.

Two observations of these plots may be made. The first, and most significant, of these is the collapse of not only the stiffness data, but of the array height data as well. This helps to provide simplification of predictions.

A second observation is the near range divergence of the P80S acceleration data. This divergence is probably related to the method by which acceleration is determined. Acceleration is estimated by the user from TOODY supplied velocity plots. These estimations are determined using calculated peak velocity and measured time to peak velocity and by assuming a parabolic rise. This defines that:

$$a = \frac{2\ v}{t_{pp}} \tag{18}$$

Rapid rise characteristic in the velocity waveforms close in to the large array likely introduced error into these calculations.

The above observations were considered when determining the fits shown in figures 28 through 30 and defined by equations 19, 20 and 21 for predicting peak array middepth motions with range. The equations which strictly define the results of the figures were manipulated by substitution of equation 17 so that the predictions may be based wholly on independent parameters rather than on dependent parameters (i.e. t_{pd}).

$$\frac{a}{C_L^2} \cdot \alpha = 1.81 \times 10^7 \left(\frac{R}{\alpha}\right)^{-0.66} \left(\frac{H\, C_L^2}{\alpha}\right)^{-0.11} \frac{1}{\rho\, C_L^2} \qquad \text{for } R \leq R_o \qquad (19a)$$

$$\frac{a}{C_L^2} \cdot \alpha = 3.22 \times 10^3 \left(\frac{R}{\alpha}\right)^{-2.88} \left(\frac{H\, C_L^2}{\alpha}\right)^{0.62} \frac{1}{\rho C_L^2} \qquad \text{for } R > R_o \qquad (19b)$$

$$\rho C_L v = 3.92 \times 10^6 \left(\frac{R}{\alpha}\right)^{-0.12} \left(\frac{H\, C_L^2}{\alpha}\right)^{0.04} \qquad \text{for } R \leq R_o \qquad (20a)$$

$$\rho C_L v = 2.24 \times 10^3 \left(\frac{R}{\alpha}\right)^{-2.11} \left(\frac{H\, C_L^2}{\alpha}\right)^{0.7} \qquad \text{for } R > R_o \qquad (20b)$$

$$\rho C_L^2 \frac{d}{\alpha} = 5.51 \times 10^4 \left(\frac{R}{\alpha}\right)^{-0.11} \left(\frac{H\, C_L^2}{\alpha}\right)^{0.39} \qquad \text{for } R \leq R_o \qquad (21a)$$

$$\rho\, C_L^2 \frac{d}{\alpha} = 158. \left(\frac{R}{\alpha}\right)^{-2.02} \left(\frac{H\, C_L^2}{\alpha}\right)^{0.9} \qquad \text{for } R > R_o \qquad (21b)$$

where

a = peak particle acceleration, g's

v = peak particle velocity, m/s

d = peak particle displacement, m

C_L = soil loading wave speed, m/s

ρ = soil mass density, kg/m^3

α = areal charge density, kg/m^2 of TNT

R = range, m

H = array height, m

The range of transition from planar to cylindrical attenuation, R_o, is a constant and was found to be

$$\frac{R_o}{C_L\ t_{pd}} = 0.4 \tag{22}$$

A fourth material property calculation was then made to study yield surface effects. In this case, the intercept on the $\sqrt{J_2'}$ axis, K, was the variable parameter with all other parameters remaining constant. Each of the terms for t_{pd}, a, v, and d, before elimination of the P_o factor, may be combined with the π term P_o/K to develop a new set of scaling terms which include this variable. Figures 31 through 35 include the results of this yield surface change with the previous calculations.

Although these results collapse with those from the other calculations, they will not be included in the prediction equations because only two values for K were considered. This is an insufficient data base from which to formulate conclusions and more calculations with different values would need to be performed to verify these results. Furthermore, failure criteria will only affect motions in the event of failure. Therefore, the phase duration and peak motion algorithms will remain as presented in equation 17

and equations 19 to 21, respectively.

4. FREE-SURFACE EFFECTS

Design expressions for motion along the middepth of an explosive array (equations 19 through 21) were developed in the preceding section. These expressions were derived assuming a plane of symmetry along this middepth. However, the motions at the ground surface are of greater significance during earthquakes, and hence, for simulation design. The effects of a free, unconfined surface were studied to a limited extent in reference 6. A more indepth analysis of the free surface is presented here to provide supplementary design relationships.

Several calculations had previously been performed in which a free surface replaced the boundary of symmetry. These calculations duplicated most parameters of the P20S symmetrical case, i.e. H = 12.2 m and McCormick Ranch material characteristics. However, a free surface was modeled and pressure was applied to elements beginning some distance below this surface simulating an explosive array buried by various depths of overburden. The study considered burial depths of 6.1 m and 12.2 m which were designated P20F and P40F, respectively.

Figure 36 demonstrates the similarity in centerline motions between the symmetric case and the two free-surface calculations. The similarity in the motions indicates that centerline predictions based upon symmetric calculations apply to middepth motions in the free surface case also. The equivalence allows that the free surface study may be based upon the results of symmetric calculations with the existing predictions for centerline motions remaining valid.

Motions at the free surface were then compared to the centerline motion in the symmetric case. The comparison revealed that the surficial motions varied from those at the middepth and that the variation depended upon the geometry of the case; that is, on the depth of surcharge and on the range in question. Figure 37 defines this dependence. The figure plots the ratio of free surface peak amplitudes (A_{FS}) and symmetric case centerline peak amplitudes (A_{CL}), as a function of range and centerline depth, i.e.

$$\frac{A_{FS}}{A_{CL}} = f\left(\frac{R}{H/2 + S}\right)$$

The characteristics of the curves are indicative of some of the characteristics of the ground motion environment. For example, close-in to the array, one would expect mostly horizontal motion at the middepth. Conversely, the surface motion would be dominated by vertical cratering effects. The curves for horizontal motion approach low surface magnitudes for low values of $R/(H/2 + S)$ agreeing with this reasoning. On the other hand, at far range the loading from the array begins to affect the overburden providing for nearly equivalent motion along a greater spatial variation both above and below the centerline. Furthermore, the displacement curve does not return to a scaled amplitude of unity probably because the lack of confinement allows for greater displacement at the surface.

These results of the analysis into free-surface effects may be applied to predictions of peak ground motion as developed in this section. However, it is important to recall that these relationships are based on calculation

results. They must be verified by large-scale earthquake simulation experiments before they may be considered reliable. The next section fulfills this need by comparing the results to data from four such experiments, the SIMQUAKE series of events.

SECTION III

SYNTHESIS OF DATA AND CALCULATIONS

The calculations discussed in previous sections were performed only after making some simplifying assumptions. These apply to explosive source, material variables, two-dimensionality and others. For this reason, the results of calculations may probably be viewed as providing qualitatively correct relationships among variables. However, it is not expected that these results will be quantitatively exact. It is necessary to utilize these results to synthesize data from field simulations which were characteristically similar to the calculations. This would provide a quantitative base to support further analysis and would also serve to verify or disprove the qualitative reliability of the calculations.

The reader may recall that this procedure was used in reference 6 to determine equations 3 through 5. However, the field test discussed therein was the small-scale MINI-SIMQUAKE (MSQ) event. Since that study, the large-scale SIMQUAKE (SQ) simulations were performed. This series of events employed planar explosive arrays to simulate earthquake ground motions. The entire series consisted of four events. These include MINI-SIMQUAKE (MSQ); SIMQUAKE IA (SQIA) and SIMQUAKE IB (SQIB) (ref. 7), two single planar array explosive events; and SQII (ref. 8) a timed sequence double planar array explosive event. SQIA, SQIB, and SQII were the first experiments using planar explosive charges to load large-scale structural models with earthquake-like motions. The plan and elevation for SQI are illustrated in figures 38 and 39, respectively.

Measured velocity positive phase durations from each experiment (see figures 40 through 43) are seen to agree with the predictions (figure 44). (Note that front array t_{pd} and peak measured amplitudes for SQII are determined by assuming superposition of waveforms from the front and back arrays).

Figures 45 to 47 show the recorded peak centerline data from the SIMQUAKE experiments compared to the predictions developed in the previous sections. The predictions are in good agreement with the actual data but, although the characteristics of the data with range are very similar to the predictions, they are not exactly forecast. However, the empirical modifications also shown on these figures demonstrate that only slight adjustment to the predictions is needed to bring about agreement. These adjustments are justified by considering the assumptions which were made, and thus are reflected in equations 23 though 25. These equations provide predictions for peak centerline horizontal acceleration, velocity, and displacement.

$$\frac{a}{C_L^2} \cdot \alpha = 1.81 \times 10^7 \left(\frac{R}{\alpha}\right)^{-0.66} \left(\frac{H C_L^2}{\alpha}\right)^{-0.11} \left(\frac{1}{\rho C_L^2}\right) \qquad \text{for } R \leq R_o \qquad (23a)$$

$$\frac{a}{C_L^2} \cdot \alpha = 1.64 \times 10^3 \left(\frac{R}{\alpha}\right)^{-3.08} \left(\frac{H C_L^2}{\alpha}\right)^{0.69} \left(\frac{1}{\rho C_L^2}\right) \qquad \text{for } R > R_o \qquad (23b)$$

$$\rho C_L v = 3.92 \times 10^6 \left(\frac{R}{\alpha}\right)^{-.12} \left(\frac{H C_L^2}{\alpha}\right)^{0.04} \qquad \text{for } R \leq R_o \qquad (24a)$$

$$\rho C_L v = 1.43 \times 10^3 \left(\frac{R}{\alpha}\right)^{-2.11} \left(\frac{H C_L^2}{\alpha}\right)^{0.70} \qquad \text{for } R < R_o \qquad (24b)$$

$$\rho C_L^2 \frac{d}{\alpha} = 5.51 \times 10^4 \left(\frac{R}{\alpha}\right)^{-0.11} \left(\frac{H C_L^2}{\alpha}\right)^{0.39} \qquad \text{for } R \leq R_o \qquad (25a)$$

$$\rho C_L^2 \frac{d}{\alpha} = 107. \left(\frac{R}{\alpha}\right)^{-2.02} \left(\frac{H C_L^2}{\alpha}\right)^{0.54} \qquad \text{for } R > R_o \qquad (25b)$$

where

a = peak particle acceleration, g's

v = peak particle velocity, m/s

d = peak particle displacement, m

C_L = soil loading wave speed, m/s

ρ = soil mass density, kg/m^3

α = areal charge density, kg/m^2 of TNT

R = range, m

H = array height

and $$\frac{R_o}{C_L t_{pd}} \cong 0.33$$

A similar analysis was conducted for surficial motions. Figures 48 to 50 compare free surface and centerline motions where measured at the same range for SQIA, SQIB and SQII to the respective predictions. These figures follow the pattern set for centerline motion predictions. That is, a general agreement is observed in the characteristic forms of the two sets of results and slight modification of the analytical curves will provide agreement with the measured data. These free-surface correction factors and the above equations were employed to synthesize the SQ data. This data, shown in figures 51 to 53, show the above method to be reliable for the case

studied. Therefore, the equations and curves presented should be used for prediction of ground motions in future experiments.

SECTION IV

SHOCK RESPONSE SPECTRA

The response spectrum was used to aid in defining simulation criteria for previous earthquake simulations (ref. 6). This form of data expresses the effects of a ground motion on an engineering system in terms of amplitude and frequency content. Several references (e.g. 6, 20, 21) discuss the response spectrum concept in detail and it will be reviewed only briefly here.

Response spectra give the maximum response of a single degree of freedom system as a function of the frequency, or period, of that system. Consider the single degree of freedom system shown in figure 54 having mass m, linear spring stiffness k and viscous damping c and subjected to a base motion, y(t). The equation of motion, expressed in one form, is

$$\ddot{u}(t) + 2\beta\omega_n\dot{u}(t) + \omega_n^2 u(t) = - y(t) \tag{26}$$

where

$y(t)$ = base displacement as a function of time

$x(t)$ = absolute displacement of the mass

$u(t)$ = relative displacement between the mass and the base = $x(t) - y(t)$

$\beta = c/\left(2\sqrt{km}\right)$ = damping ratio or fraction of critical damping

$\omega_n = \sqrt{k/m}$ = undamped natural frequency

and a dot ($\cdot$) above a variable indicates differentiation with respect to time.

Solution of equation 26 for u and successive differentiation of this solution for $\dot{u}$ and $\ddot{u}$ yield expressions for relative displacement (S_d), relative velocity (S_v) and absolute acceleration (S_a). Each of these quantities can then be computed as a function of the natural frequency or period of the system for a given base motion. The resulting values, plotted against frequency or period, form the maximum relative displacement spectrum, maximum relative velocity spectrum, or maximum absolute acceleration spectrum, respectively. Each of these, individually, is commonly called a response spectrum. Figure 55 is an example of a relative velocity spectrum.

It can be noted that each type of spectrum satisfies different needs. The relative velocity spectrum has good definition at both high and low values of frequency while the relative displacement and acceleration spectra become obscured. The maximum relative velocity gives a direct measure of the maximum energy per unit mass in the system. The relative displacement spectrum is important because it is directly related to system strain. The absolute acceleration spectrum is important because it is directly proportional to the seismic coefficient or lateral force coefficient commonly used in building codes, i.e., if

$$F_{max} = CW \tag{27}$$

where

F_{max} = the maximum force on the mass

W = weight of the mass

C = seismic coefficient

then

$$C = \frac{1}{g} (\omega_n S_v) = \frac{1}{g} (\frac{2\pi}{T} S_v) \tag{28}$$

where

g = acceleration due to gravity

and the term in parentheses is the maximum absolute acceleration of the system.

Rather than work with each spectrum separately it would be convenient to find a unique relation among these parameters. This may be accomplished by assuming small values of damping, β, and by making other simplifying assumptions to show that

$$\frac{1}{\omega_n} S_{pa} = S_{pv} = \omega_n S_d \tag{29}$$

where the added subscript, p, refers to pseudoacceleration and pseudovelocity (sometimes denoted by PSV) to reflect these assumptions. This relation allows that the three parameters of motion can be plotted on a single tripartite plot as exemplified in figure 56.

The study of response spectra for earthquakes, and for simulation design, is supported by noting the following useful features discussed in reference 21. In spite of its definition in terms of a single degree of freedom system, these features include:

(1) The effect of system damping in limiting the dynamic stresses in a system is often apparent from the response spectrum. Undamped spectra for earthquakes often show irregular peaks suggesting dominant periods in the

input and large responses for certain system periods. However, small amounts of damping, as illustrated in figures 55 and 56, removes most of the peaks. Reference 21 notes that damped response spectra for a number of earthquakes indicate that there are no dominant periods as far as most structures with some damping are concerned.

(2) Response spectra can provide an upper bound to response for multi-degree of freedom systems which can be decoupled into a series of single degree of freedom systems. The method is described in several available references, reference 16 for example.

(3) Many complex structures behave as single degree of freedom systems under some circumstances, and the response spectra can be applied directly.

(4) The response spectrum gives the energy input into the system directly.

The foregoing discussion indicates that information in the form of a response spectrum would be useful in setting simulation criteria. Therefore, simulation design would be improved with a reliable technique by which spectra may be predicted for earthquakes and for simulation generated motions. References 20 and 22 discuss methods for estimating spectral plots. The former reference presents undamped spectral multiples of 1, 1.5 and 2 for displacement, velocity and acceleration, respectively, based on results for short impulsive motion (a parabolic velocity pulse with no inward component).

The method of reference 22 is based on a statistical analysis of available earthquake data. The technique assumes a standard shape response spectrum based on a 1 g acceleration earthquake with 36 inch displacement. Amplification factors as a function of percent damping determine the

magnitude of the spectrum at various control frequencies.

It is desired that a spectral prediction method should apply to earthquakes and to explosive simulation events. However, while the latter of the above techniques has shown to be appropriate for earthquakes (e.g., figure 57), it proves to be inadequate for the simulation events (e.g., figure 58). The estimate overpredicts the velocity and displacement portions of the explosive spectra. These results indicated a need for a method for predicting response spectra that would be applicable to both prototype earthquakes and to explosive simulations. This technique should rely on each type of motion and on the duration of significant motion.

Such a technique has been developed in the course of this study. The method relies on peak values of acceleration, velocity and displacement and on motion duration to define unique spectra for each motion record with its own control frequencies and amplification factors which are dependent upon these motion characteristics.

The relative amplitudes of acceleration, velocity, and displacement imply certain frequency content in the ground motion. Three "control frequencies" can be estimated as follows:

$$\omega_1 = \frac{a}{v},\ \omega_2 = \sqrt{\frac{a}{d}},\ \omega_3 = \frac{v}{d} \tag{30}$$

where

$\omega_1, \omega_2, \omega_3$ = control frequencies

a = peak acceleration

v = peak velocity

d = peak displacement

In essence, equations 30 provide an estimate of the frequency of the sinusoids which, superimposed, would produce the given combinations of a and v, a and d, and v and d. The frequencies ω_1 and ω_3 are the corner frequencies previously used by Newmark and Hall (ref. 23) in developing approximate spectra.

To first order, it can be assumed that earthquake and simulation time histories are such a superposition of three functions, each with one of the control frequencies as its fundamental frequency. The motion duration can be used to obtain an estimate of the number of cycles of motion at each control frequency by the equation

$$N = \frac{\omega t}{2\pi} \tag{31}$$

where

N = number of cycles of motion

t = duration of motion

ω = frequency of interest

The dependence of response spectra on number of motion cycles, as well as on damping, will be demonstrated.

Three alternative simple functions were considered in this study. These are the simple sinusoid (SS), the linearly damped sinusoid (LDS) and the parabolically modulated sinusoid (PMS). Figures 59a and 59b illustrate the LDS and PMS functions which are given mathematically by

LDS:

$$v = A(\sin \omega t)\ (1 - \frac{\omega t}{2\pi N}),\ t \leq \frac{2\pi N}{\omega}$$

$$v = 0 \qquad t > \frac{2\pi N}{\omega}$$

PMS:

$$v = A(\sin \omega t)\left(4 \frac{\omega t}{2\pi N} - 4\left(\frac{\omega t}{2\pi N}\right)^2\right), \quad t \leq \frac{2\pi N}{\omega}$$

$$v = 0 \qquad t > \frac{2\pi N}{\omega}$$

As noted above, response spectra depend on number of motion cycles and damping. To illustrate, figure 60 presents normalized response spectra computed at 5 percent damping for an input LDS velocity function with a frequency of 10 Hz and a maximum velocity equal to 1 cm/sec. N varies from 1 to 30. Similarly, figure 61 shows normalized spectra for 8 motion cycles of this same velocity function at damping values ranging from undamped to 10 percent of critical damping. One may note from these figures that N and β do indeed effect the exact shape of the response spectra. These effects are summarized in figure 62 which plots pseudovelocity amplification factor versus number of motion cycles as a function of damping for the LDS function. (Note that as N increases the curves for amplification factors approach the steady state solutions.) Figure 63 compares similar curves derived for the SS and the PMS functions to that for the LDS at β = 5 percent.

Another interesting and important observation of figures 60 and 61 is that the spectra depart significantly only in the range f/3 to fx3, where f is the frequency of the input. Further analysis of the LDS function shows the constant value that the spectra maintains for low frequencies, below f/3, to be equal to the computed peak displacement. Similarly, computations

show the constant value above fx3 to be approaching 1.5 times the peak acceleration. These observations apply approximately to the SS and PMS functions as well. It is an important guide in estimating response spectra using the control frequencies.

To recap, the amplitudes of motion can be used to obtain control frequencies. The duration estimate can be used to estimate the number of cycles at each frequency. Now it is a matter of determining which function to use to obtain spectral amplification factors and what portion of the peak velocity to use at each frequency. (Recall that the peak velocity is assumed to result from a superposition of the three functions).

Each type of event must be considered separately to determine the representative simple function and the apportionment of peak velocity to each control frequency. This is due to the differences in mechanisms which created the ground motions and the manner in which these differences are manifest in those ground motions.

The double array explosive event predictions presented herein assumed the PMS function and apportioned the peak velocity 1/4 each to the high and low control frequencies and 1/2 to the center frequency. The earthquake predictions assumed the PMS function with apportionment of 1/3 the peak velocity to each of the control frequencies. The predictions are completed by matching the spectra to the peak instrumental displacement at frequencies below $f_3/3$ and matching 1.5 times the peak instrumental acceleration at frequencies beyond $f_1 x3$.

This methodology was used to estimate the spectra for several of the SIMQUAKE ground motion records (ref. 8) and for several earthquake motion records (refs. 24 and 25). Five percent damping was considered for all

records. Computed and predicted spectra for several measurements each of SQII and for earthquakes are presented in figures 64 through 70. Spectral predictions based on reference 22 are also presented for comparison.

These results demonstrate a good potential for successfully predicting design response spectra. Extensive analysis of existing records needs to be performed to achieve more definitive rules for apportioning the peak velocity, for selecting appropriate functions for determining amplification factors, for defining the displacement assymptote, and for overall method improvement. However, due to its consideration of different characteristics of motion, it would have a more definitive basis for application than methods presently in use. Furthermore, it is important that the method can be used for explosive ground motion as well as for earthquakes. With further development, it may be used along with predicted motion to help to develop criteria for a simulation experiment.

SECTION V

CONCLUSIONS

The primary objective of this investigation was the improvement of techniques for design of simulations of earthquake motions using high explosives. This improvement includes widening the applicability of prediction algorithms and verification of predictions through comparisons to relevant data. The objective was met by addressing two major tasks.

The first task was a direct investigation of existing techniques. A series of two-dimensional finite difference calculations was performed to study the effects of changes in material properties on the resultant ground motions. The results of these calculations allowed for the revision of equations used to predict peak horizontal particle motion with range along the middepth of a planar explosive array. The predictions of acceleration, velocity and displacement now include considerations of the following variables:

- height of explosive array
- density of explosive charge
- range from array
- material stiffness

The effect of material strength was also investigated but the study was too limited to justify inclusion of the results.

In addition to revision of centerline predictions, the relationship between these motions and those at the free suface was also studied. Surficial motions are of primary importance in earthquake engineering and

this investigation reviewed free surface motions and the effects of test geometry on them. Results of calculations allowed that peak surficial motions may be estimated as a function of peak centerline motions, array height and depth of burial of the explosive array.

In final regard to improvement, the prediction of motions in the frequency domain was investigated. A technique was developed which uses peak acceleration, velocity and displacement and duration of significant motion to estimate the shock response spectrum which would represent a given motion-time history. This method assumes superposition of sinusoids of different amplitude and frequency to predict spectra which change in relative amplitudes and shape depending upon the parameters of motion peaks and duration. Previous estimates assumed consistent shape and relative amplitudes of spectral plots.

The second major task called for verification of the design techniques with actual field simulation data. Data from the SIMQUAKE experiments were examined and compared to predictions developed for the simulations from these methods. These data included motion amplitudes measured in the tests and shock response spectra determined for the records.

Predictions were developed for peak centerline motions, peak surface motions and shock response spectra. The comparisons between data and calculations presented herein verify the algorithms developed in this investigation. However, the equations do not include all parameters which were defined for the problem. Therefore, the equations are not yet universal and are not applicable for all test sites. However, although more parametric studies are required for full definition of effects of materials

and test site geometry, the results of this investigation have provided considerable improvement in simulation design techniques.

It is recommended that more in depth calculational studies be undertaken to provide even more universal definition within the simulation design techniques. Furthermore, it is recommended that actual simulation in varying media be carried out to verify such studies and, more importantly, to increase the understanding of earthquake loading phenomena.

REFERENCES

1. Wosser, T. D., Campi D. and Fovinci, M., "On the Earthquake-Induced Failure of the Imperial County Services Building", Reconnaissance Report-Imperial County, California, Earthquake, October 15, 1979, Leeds, D. J., Editor, Earthquake Engineering Research Institute, Berkeley, California, February 1980.

2. Earthquake Environment Simulation, Final Report and Proceedings, Workshop on Simulation of Earthquake Effects on Structures, National Academy of Engineering, Washington, D.C., 1974.

3. Lee, K. L., Marcuson, W. F., III, Stokoe, K. H., II, and Yokel, F. Y., Editors, Research Needs and Priorities for Geotechnical Earthquake Engineering Applications, Report of a Workshop held at the University of Texas at Austin on June 2 and 3, 1977, Sponsored by the National Science Foundation and the National Bureau of Standards.

4. Scholl, R. E., Editor, Potential Utilization of the NASA/George C. Marshall Space Flight Center in Earthquake Engineering Research, Workshop held at the NASA/George C. Marshall Space Flight Center on February 23-25, 1979, Sponsored by the National Science Foundation and the National Aeronautics and Space Administration, Earthquake Engineering Research Institute, Berkeley, California, December 1979.

5. Higgins, C. J. and Steedman, D. W., Evaluation of the Feasibility of Establishing a National Testing Capability for the Simulation of Earthquake Loads on Large-Scale Structures, Final Report on NSF Grant No. PFR-8009884, Albuquerque, New Mexico, March 1981.

6. Higgins, C. J., Johnson, R. L. and Triandafilidis, G. E., The Simulation of Earthquake-Like Ground Motions with High Explosives, Report No. CE-45 (78) NSF-507-1 on NSF Grant ENG 75-21580, The University of New Mexico, Albuquerque, New Mexico, July 1978.

7. Higgins, C. J., et. al., SIMQUAKE I - An Explosive Test Series Designed to Simulate the Effects of Earthquake-Like Ground Motions on Nuclear Power Plant Models, 7 Volumes, Report No. NP-1728 on Research Project RP-810, Electric Power Research Institute, Palo Alto, California, February 1981.

8. Higgins, C. J., Simmons, K. B. and Pickett, S. F., SIMQUAKE II - A Multiple Detonation Explosion Test to Simulate the Effects of Earthquake-Like Ground Motions on Nuclear Power Plant Models, 8 Volumes, The University of New Mexico Report on Contract RP 810-1 for the Electric Power Research Institute, Palo Alto, California, January 1979.

9. Bertholf, L. D. and Benzley, S. E., TOODY II - A Computer Program for Two-Dimensional Wave Propagation, SC-RR-68-41, Sandia Laboratories, Albuquerque, New Mexico, November 1968.

10. Sedov, L. I., Similarity and Dimensional Methods in Mechanics, Academic Press, New York and London, 1959.

11. Baker, W.E., et. al., Similarity Methods in Engineering Dynamics, Sparton Books, Hayden Book Company, Inc., Rochelle Park, New Jersey, 1973.

12. Murphy, G., Similitude in Engineering, The Ronald Press Co., New York, 1950.

13. Buckingham, E., Model Experiments and the Forms of Empirical Equations, Spring Meeting, American Society of Mechanical Engineers, June 1915.

14. Lawrence, R. J. and Mason, D. S., WONDY IV - A Computer Program for One-Dimensional Wave Propagation with Rezoning, SC-RR-71-0284, Sandia Laboratories, Albuquerque, New Mexico, August 1971.

15. Crowley, B. K., "Scaling Criteria for Rock Dynamic Experiments", Proceedings, Symposium on Engineering With Nuclear Explosives, American Nuclear Society and USAEC, Conf-700101 (Vol. 1), Las Vegas, Nevada, May 1970.

16. Crawford, R. E., Higgins, C. J. and Bultmann, E. H., The Air Force Manual for Design and Analysis of Hardened Structures, AFWL-TR-74-102, Air Force Weapons Laboratory, Kirtland AFB, New Mexico, October 1974.

17. Triandafilidis, G. E., Calhoun, D. E. and Abbott, P. A., Simulation of Airblast-Induced Ground Motions at McCormick Ranch Test Site, Vol. I, Project SILT PILE, AFWL-TR-68-27, Air Force Weapons Laboratory, Kirtland AFB, New Mexico, October 1968.

18. Schlater, D. R., DIHEST Improvement Program Test, DIP IA, Data Report, AFWL-TR-71-120, Air Force Weapons Laboratory, Kirtland AFB, New Mexico, January 1972.

19. Mazanti, B. B. and Holland, C. N., Study of Soil Behavior Under High Pressure, Report 1: Response of Two Recompacted Soils to Various States of Stress, Vols. 1-3, S-70-2, U.S. Army Waterways Experiment Station, Vicksburg, Mississippi, 1970.

20. Veletsos, A., et al, Design Procedures for Shock Isolation Systems of Underground Protective Structures, Vol. III Response Spectra of Single-Degree-of-Freedom Elastic and Inelastic Systems, Final Report RTD TDR-63-3096, Vol. III., Air Force Weapons Laboratory, Kirtland AFB, New Mexico, June 1964.

21. Hudson, D. E., "Response Spectrum Techniques in Engineering Seismology", Proceedings of the World Conference on Earthquake Engineering, Berkeley, California, June 1956.

22. Newmark, N. M., Blume, J. A. and Kapur, K. K., "Seismic Design Spectra for Nuclear Power Plants", Journal of the Power Division, ASCE, Vol. 99, No. PO2, November 1973.

23. Newmark, N. M. and Hall, W. J., "Seismic Design Spectra for Trans-Alaska Pipeline", Proceedings, Fifth World Conference on Earthquake Engineering, Rome, 1973.

24. Strong Motion Earthquake Accelerograms, Digitized and Plotted Data, Volume II - Corrected Accelerograms and integrated Ground Velocity and Displacement Curves, Part A - Accelerograms IIA001 through IIA020, EERL 71-50, Earthquake Engineering Research Laboratory, California Institute of Technology, Pasadena, California, September 1971.

25. Analyses of Strong Motion Earthquake Accelerograms, Volume III - Response Spectra, Part A - Accelerograms IIA001 through IIA020, EERL 72-80, Earthquake Engineering Research Laboratory, California Institute of Technology, Pasadena, California, August 1972.

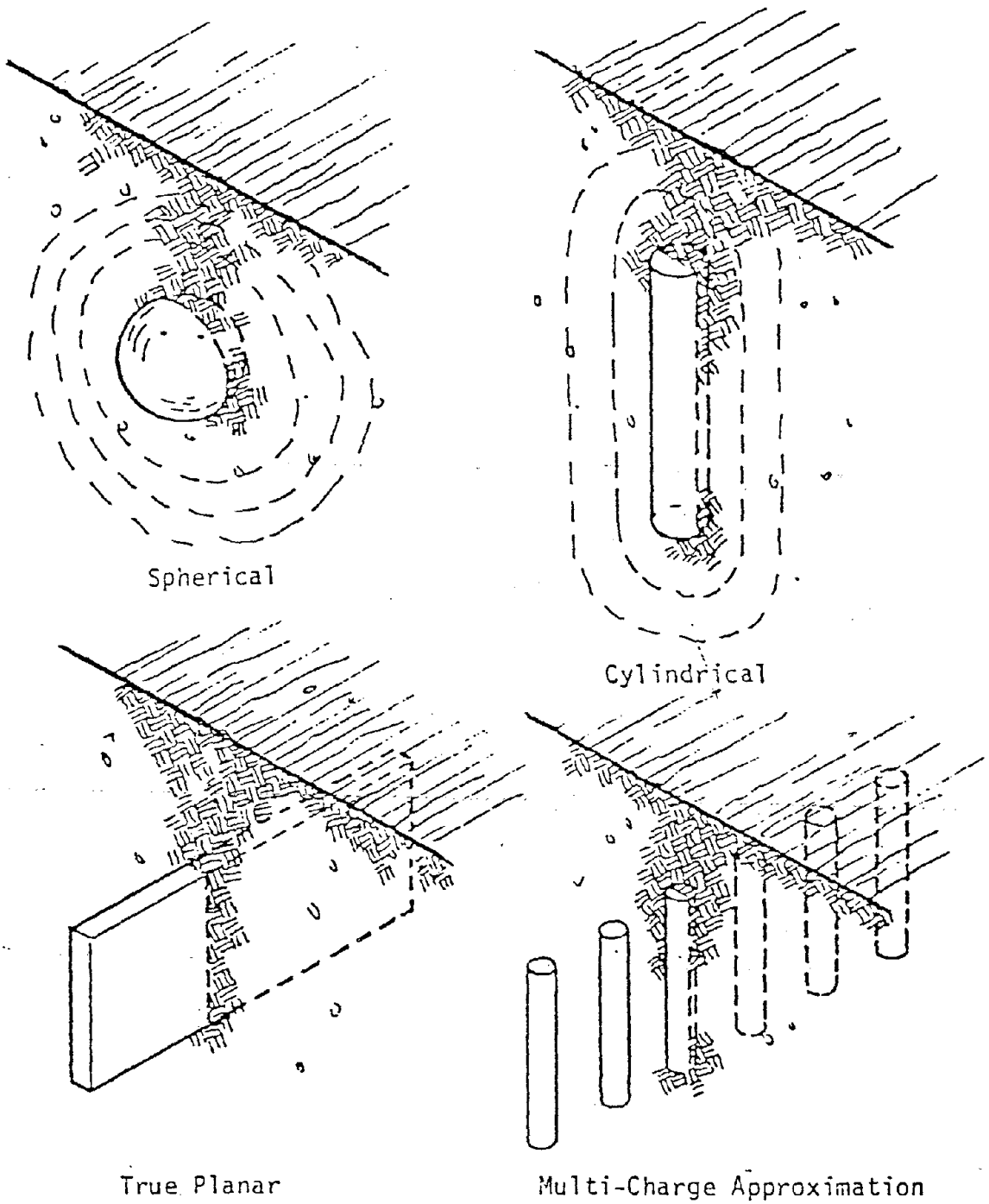

Figure 1. Three classes of explosive charge configuration.

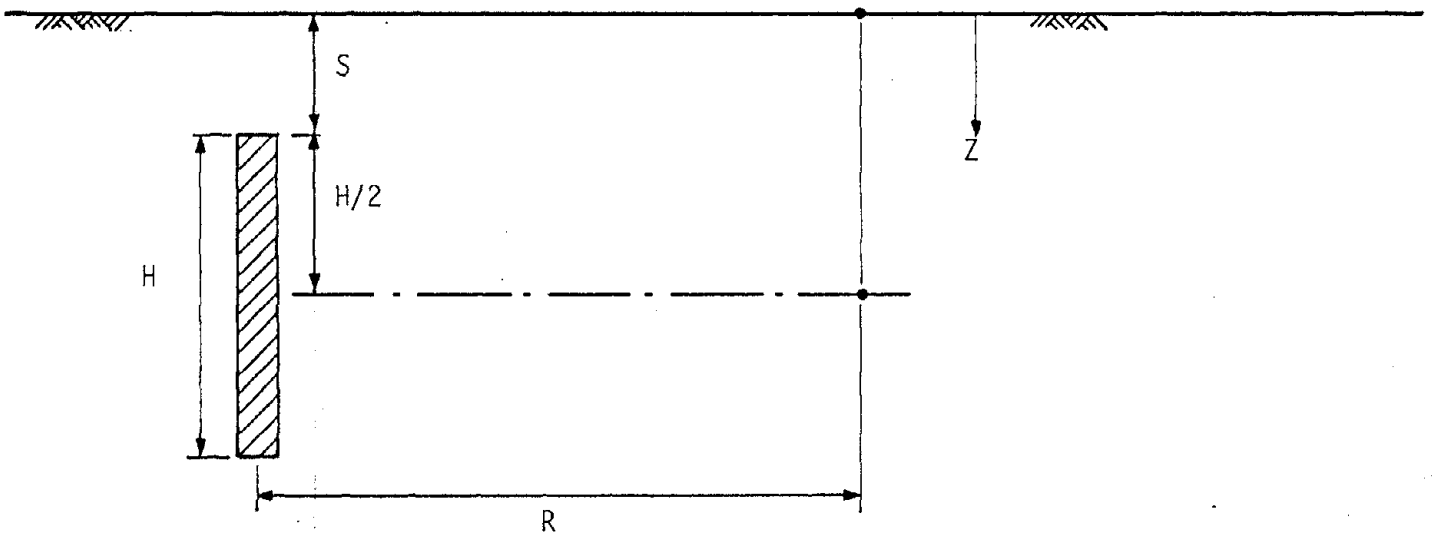

Figure 2. Test site geometry for earthquake simulation using planar explosive array.

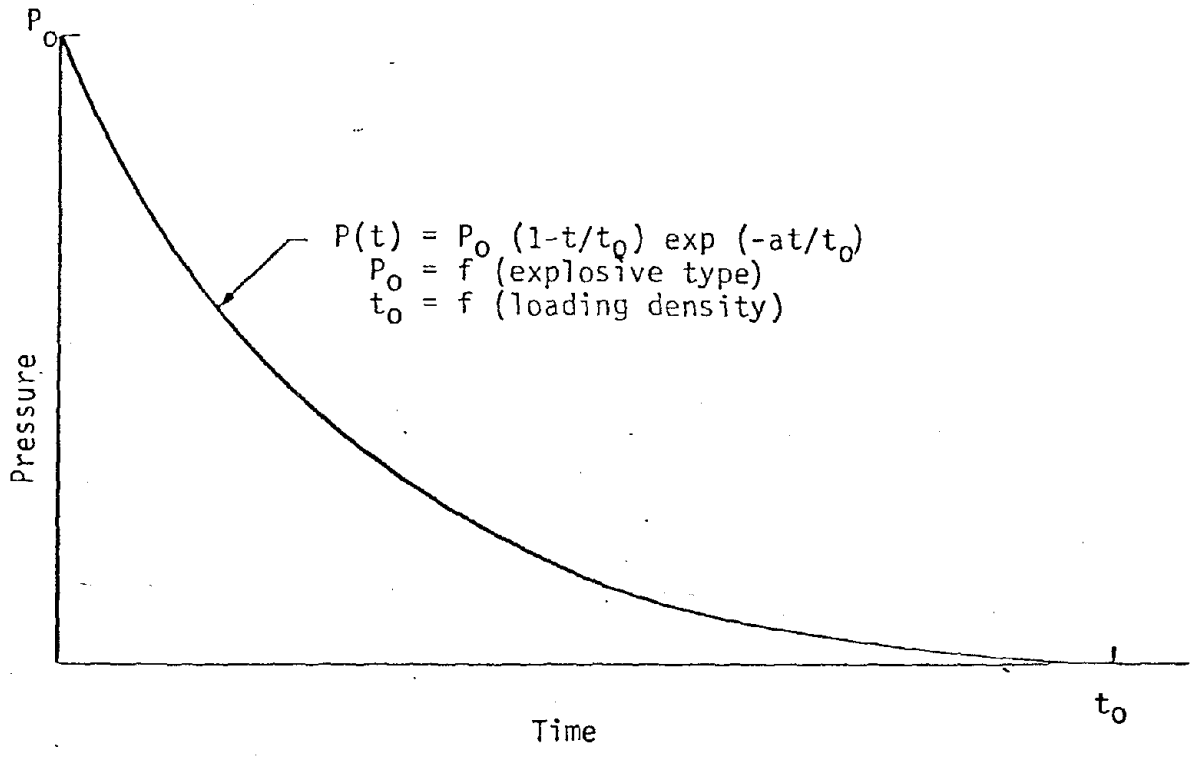

Figure 3. Pressure-time history input for two-dimensional finite difference calculations.

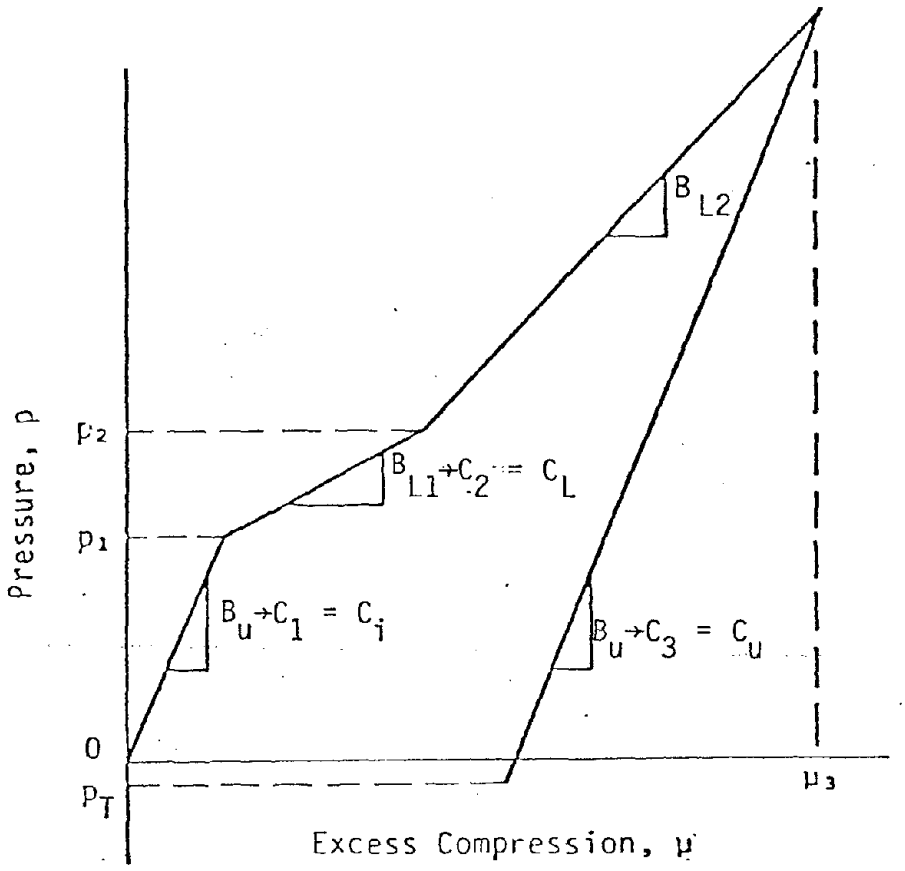

(b) Hydrostat

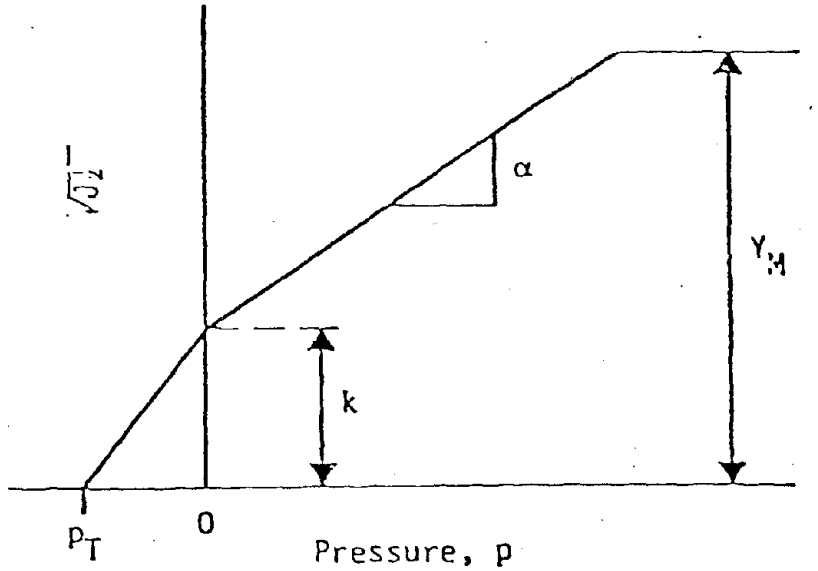

(a) Failure Surface

Figure 4. Soil constitutive model used in calculations.

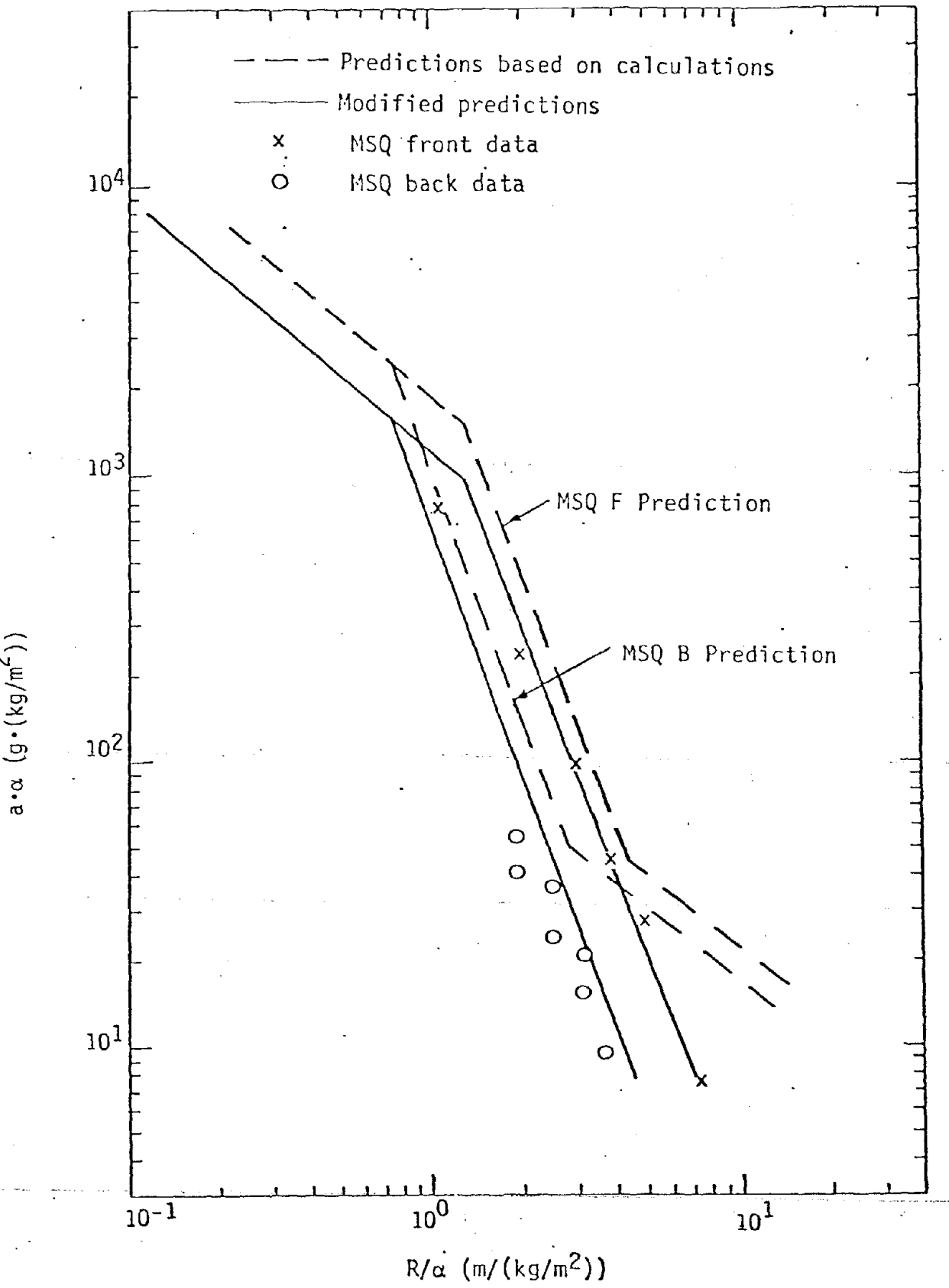

Figure 5. Planar accelerations predicted in reference 6 compared with MINI-SIMQUAKE data.

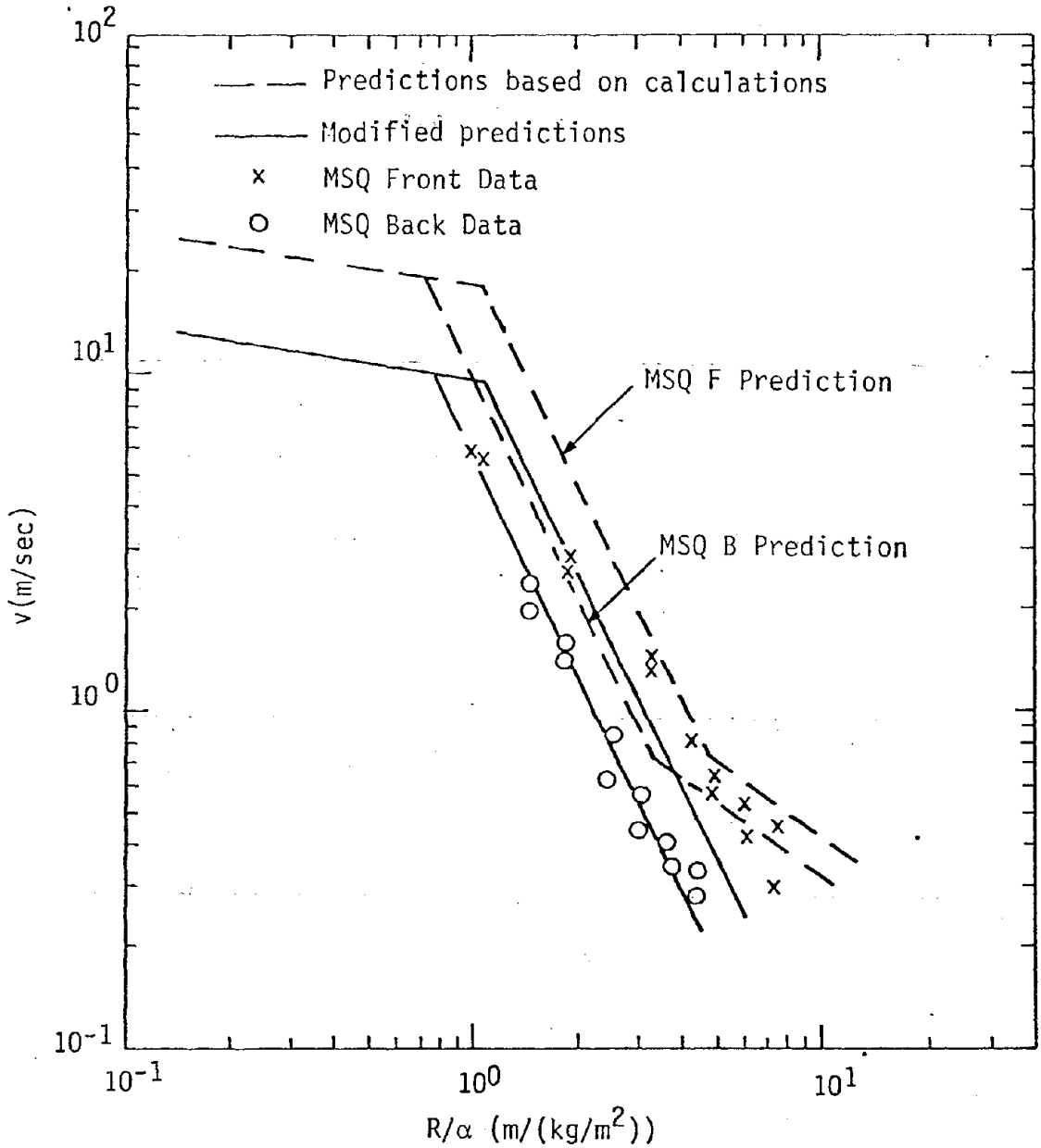

Figure 6. Planar velocities predicted from reference 6 compared with MINI-SIMQUAKE data.

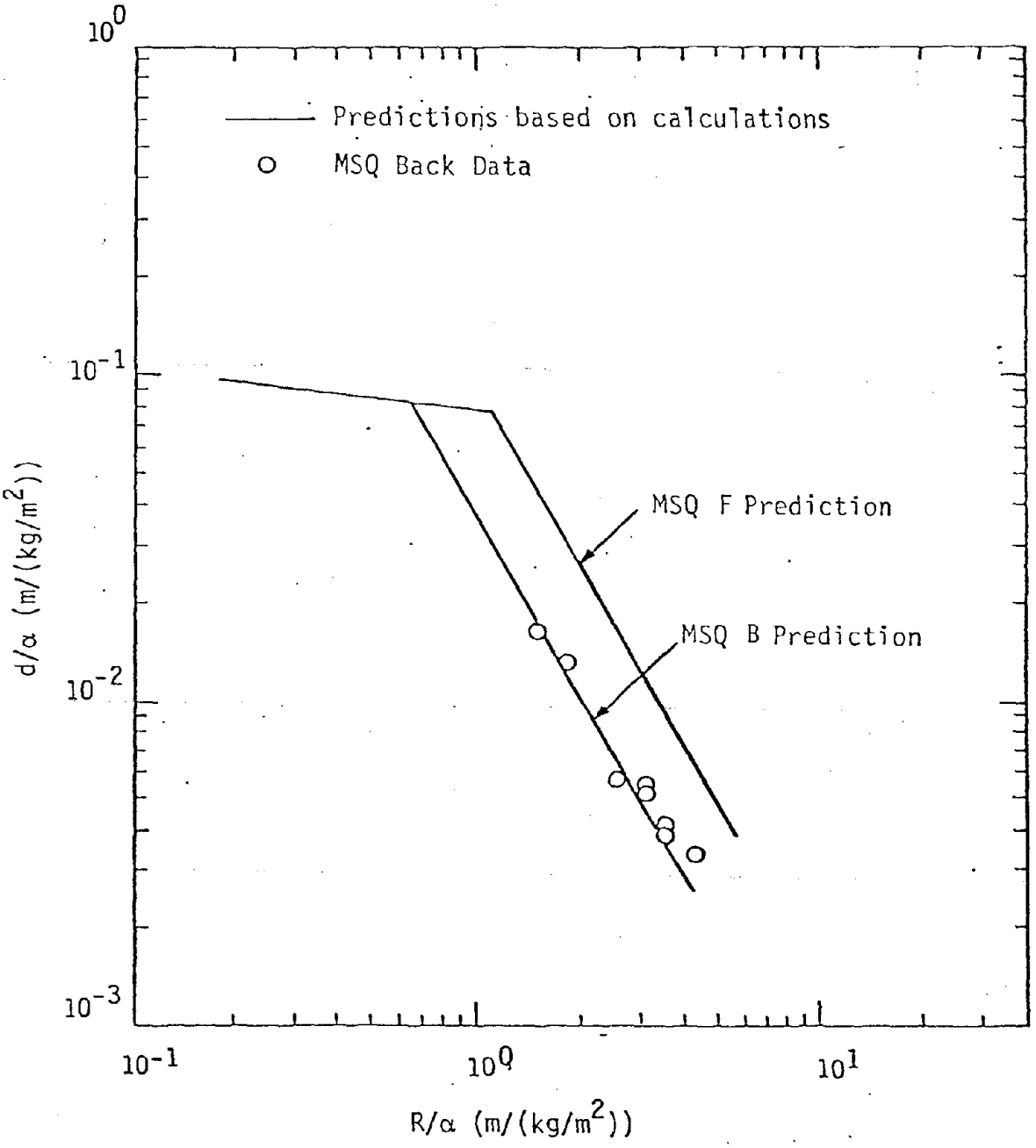

Figure 7. Planar displacements predicted from reference 6 compared with MINI-SIMQUAKE data.

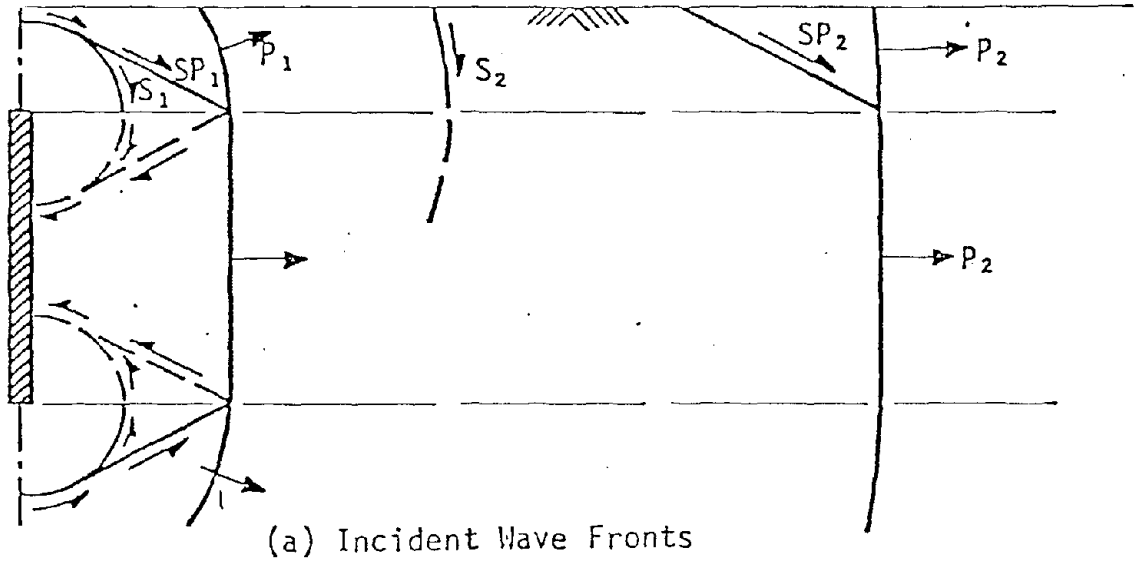

(a) Incident Wave Fronts

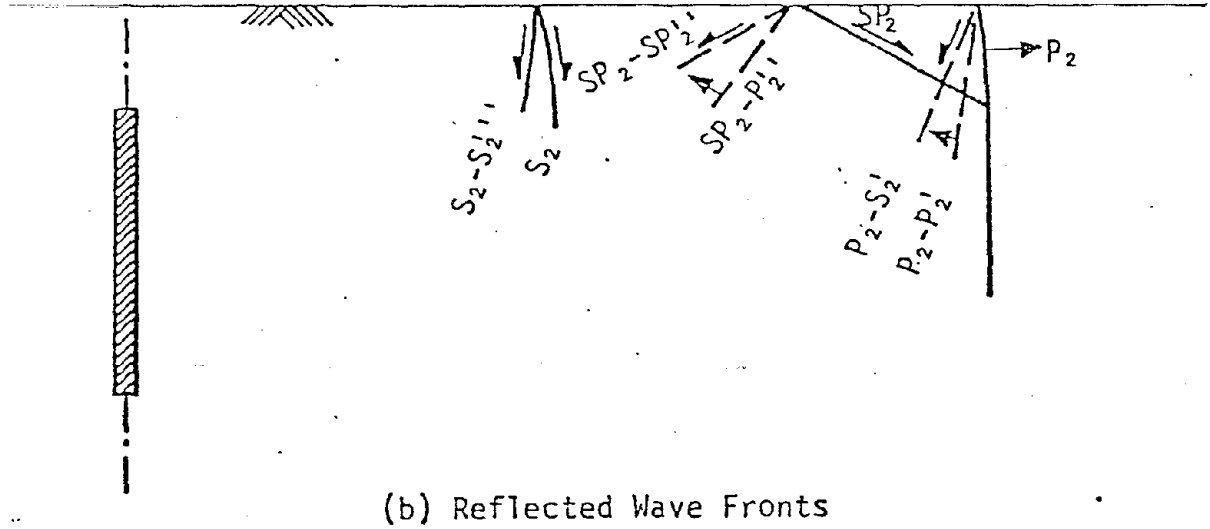

(b) Reflected Wave Fronts

Notation: Subscripts 1 and 2 refer to two different times

P - Incident P-Wave
S - Incident S-Wave
SP - Incident von Schmidt-like Wave
P-P' - Reflected P Due to Incident P
P-S' - Reflected S Due to Incident P
SP-P'' - Reflected P Due to Incident SP
SP-SP'' - Reflected SP Due to Incident SP
S-S''' - Reflected S Due to Incident S

Figure 8. Incident and reflected wave fronts near surface.

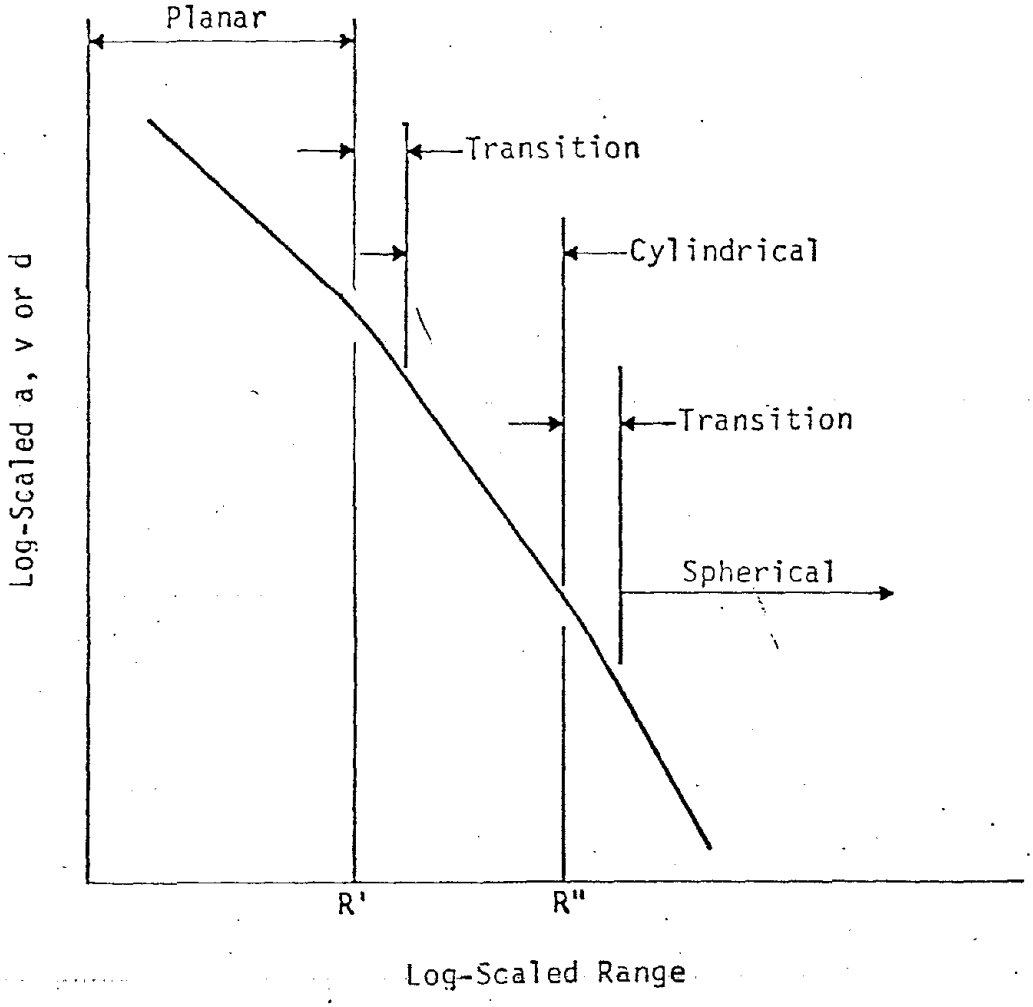

Figure 9. Effect of finite array dimensions on peak ground shock attenuation.

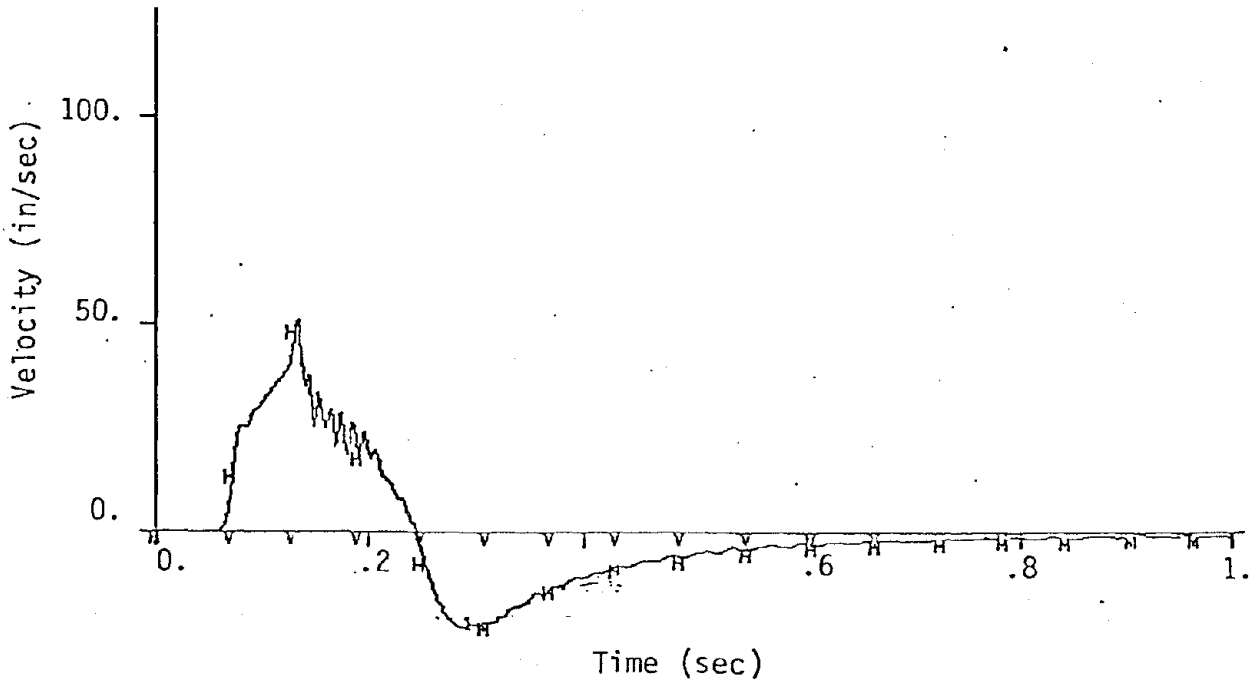

a) Cylindrical range (R = 36.5m)

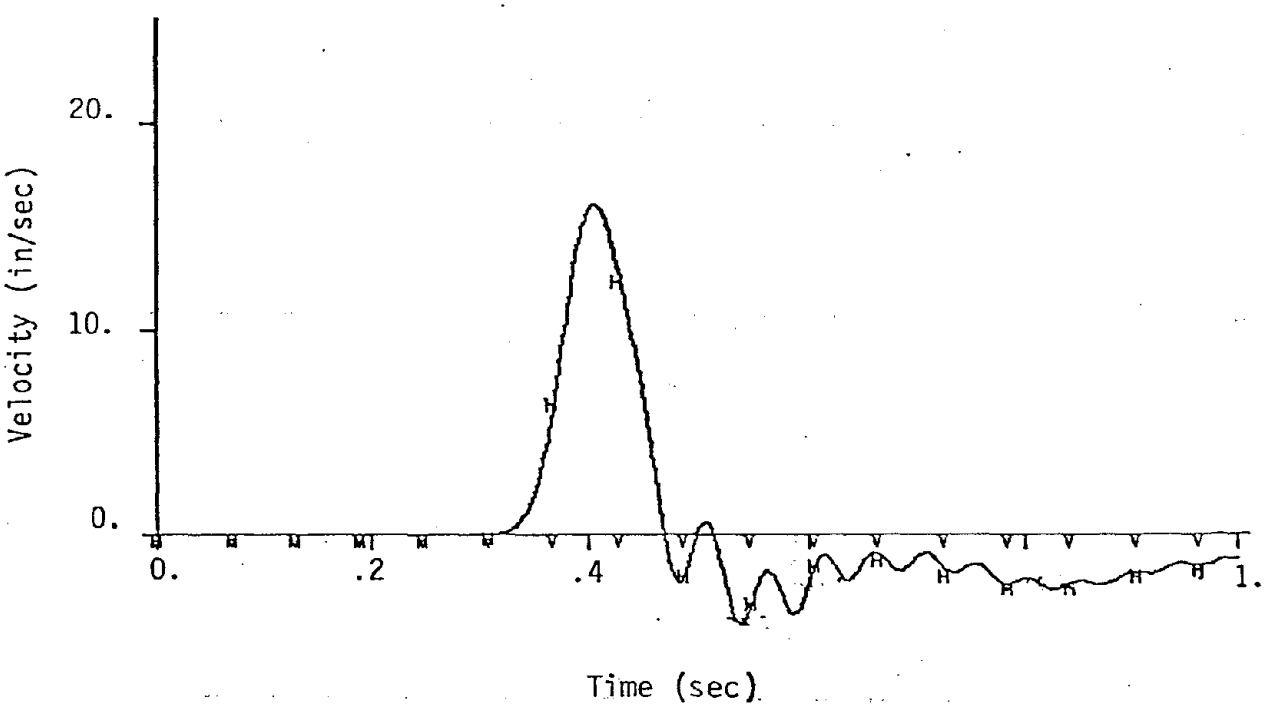

b) Elastic range (R = 183m)

Figure 10. Velocity waveforms from array centerline, calculation P20S.1 at different ranges.

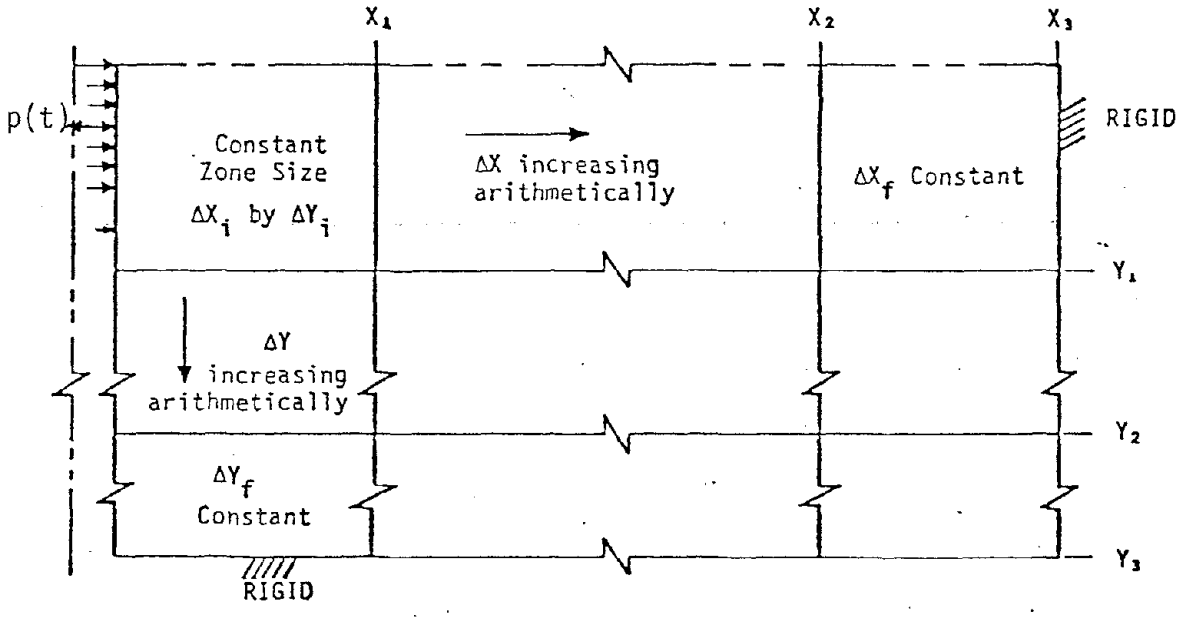

Figure 11. Two-dimensional calculation zoning configuration.

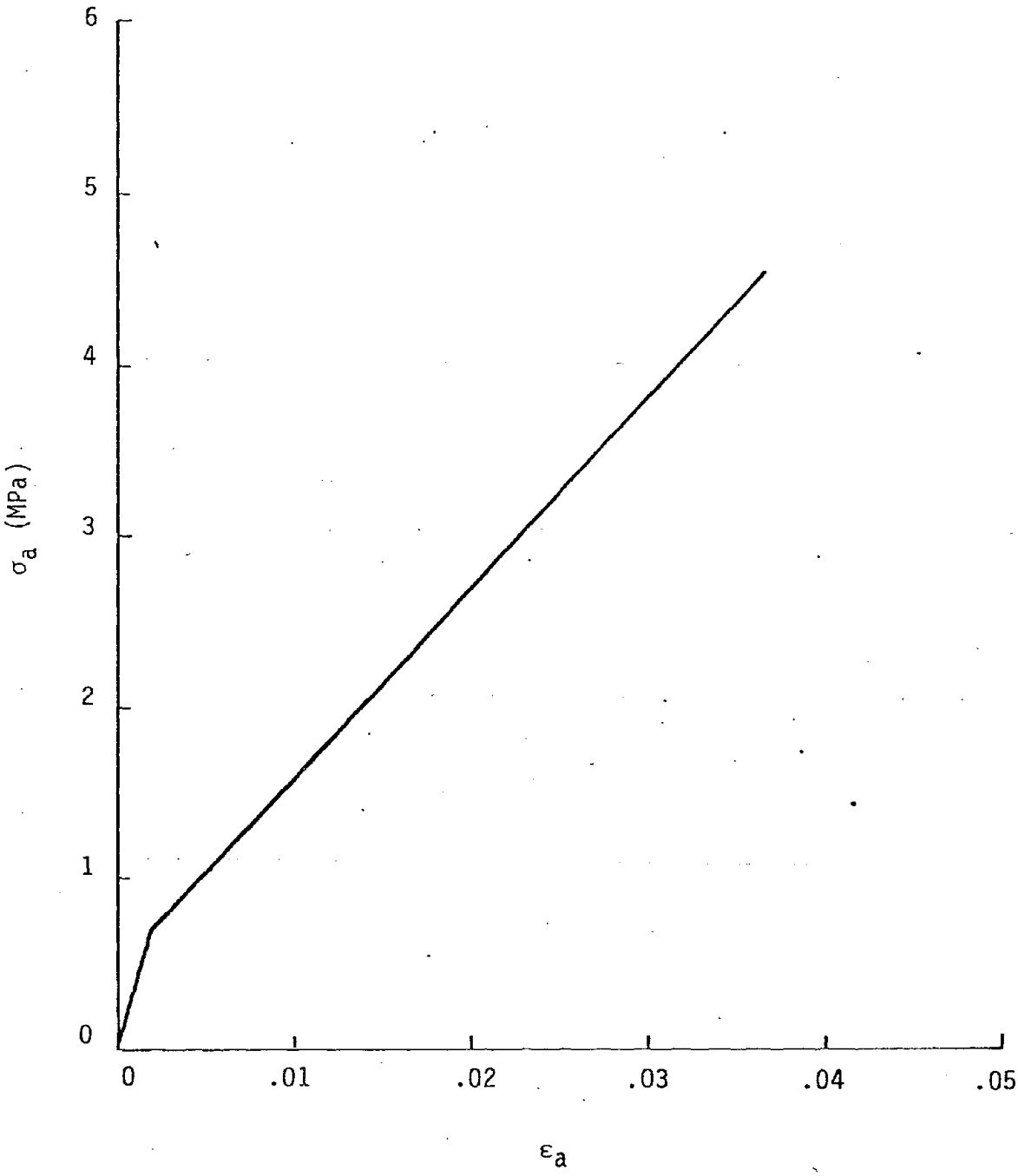

Figure 12. McCormick Ranch seismic based uniaxial curve.

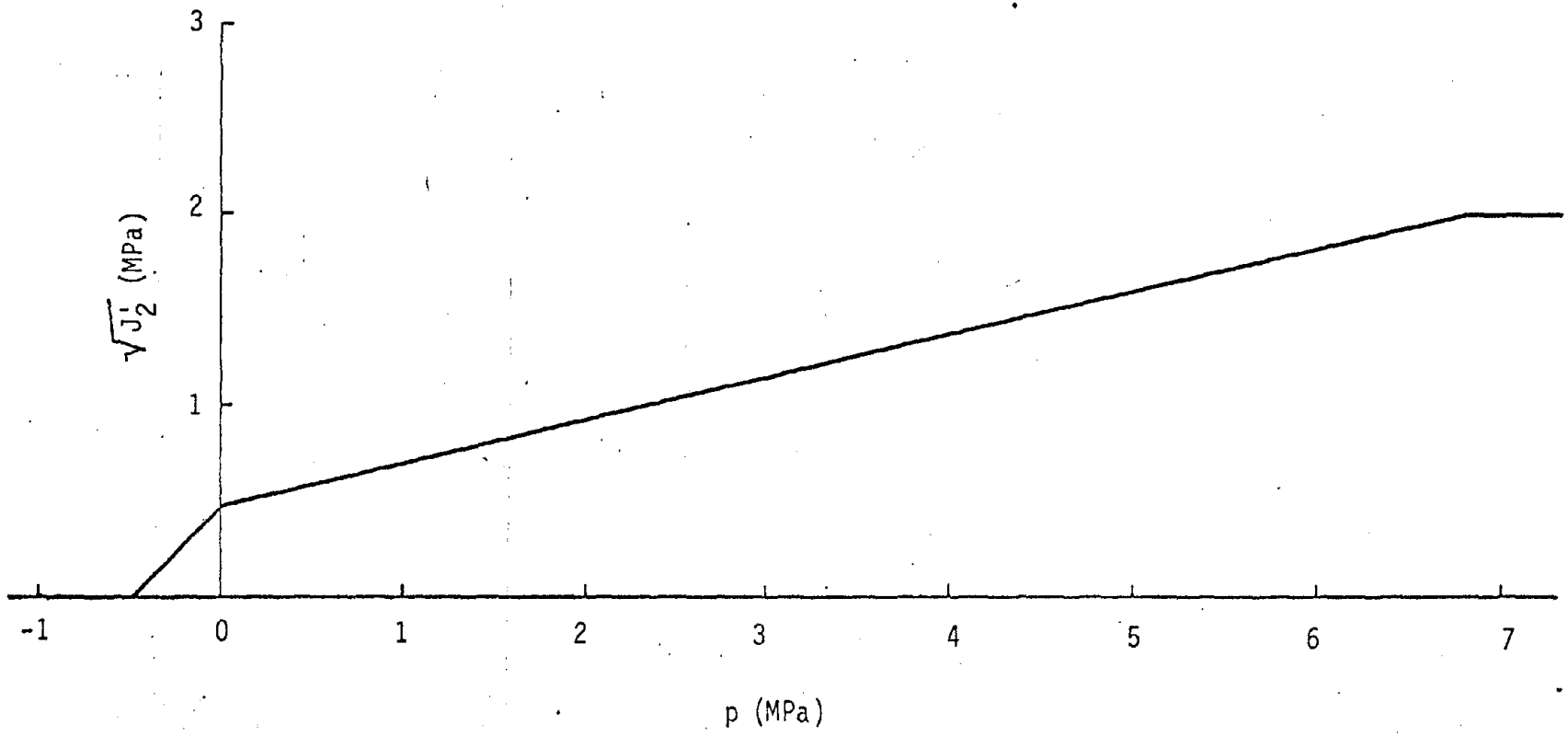

Figure 13. McCormick Ranch failure surface.

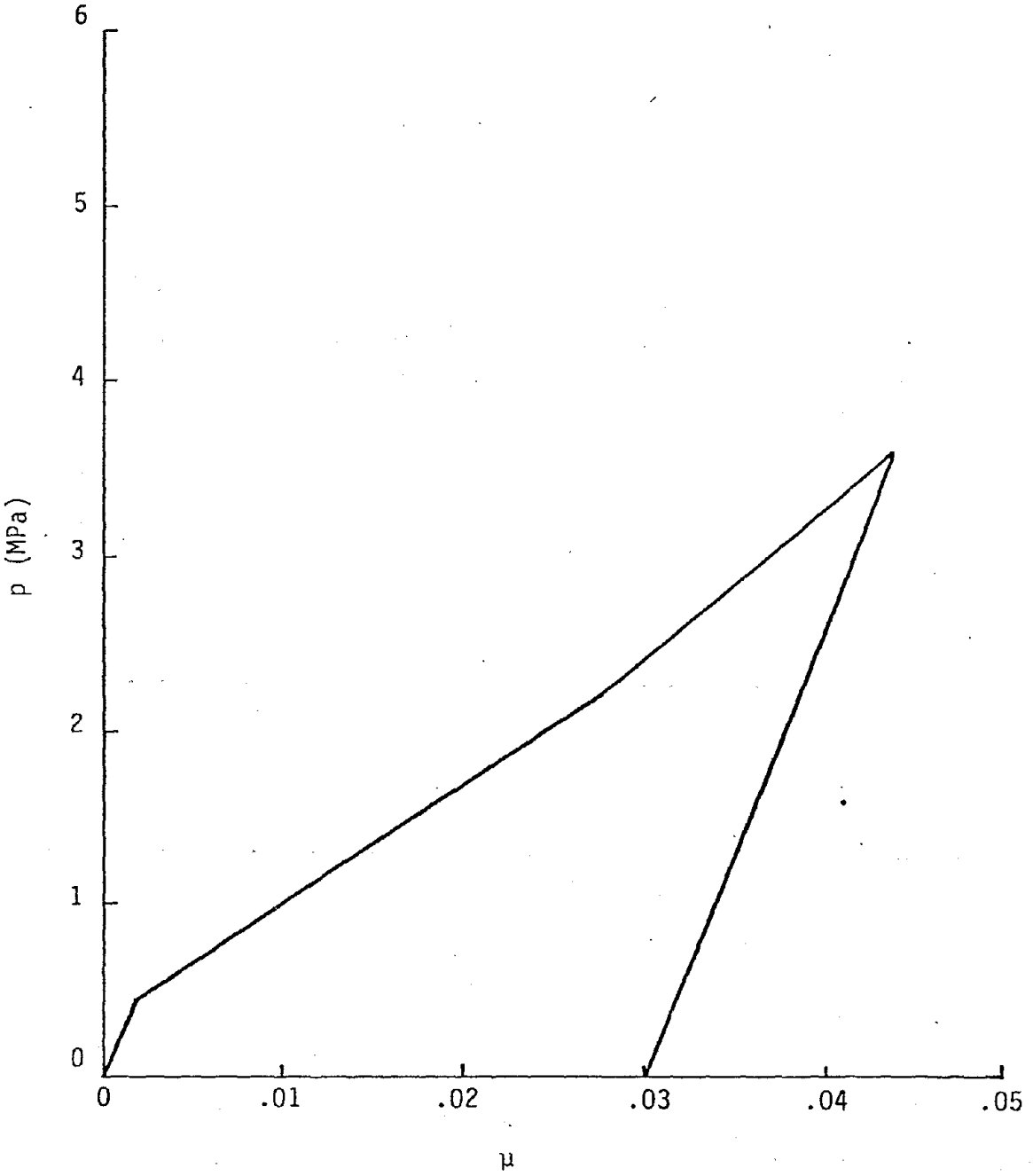

Figure 14. McCormick Ranch seismic based hydrostat.

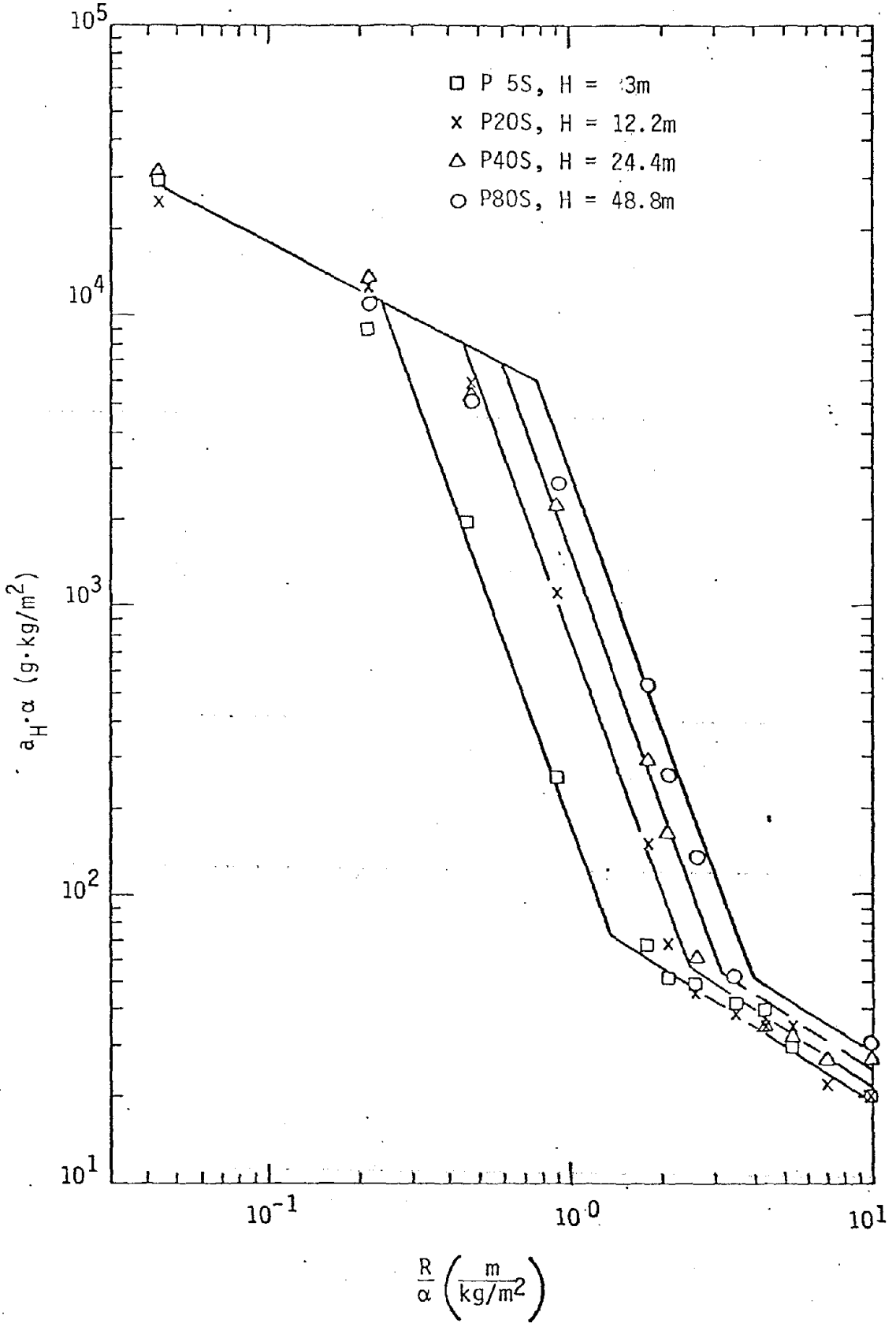

Figure 15. Effect of array height on calculated peak horizontal acceleration; McCormick Ranch material model.

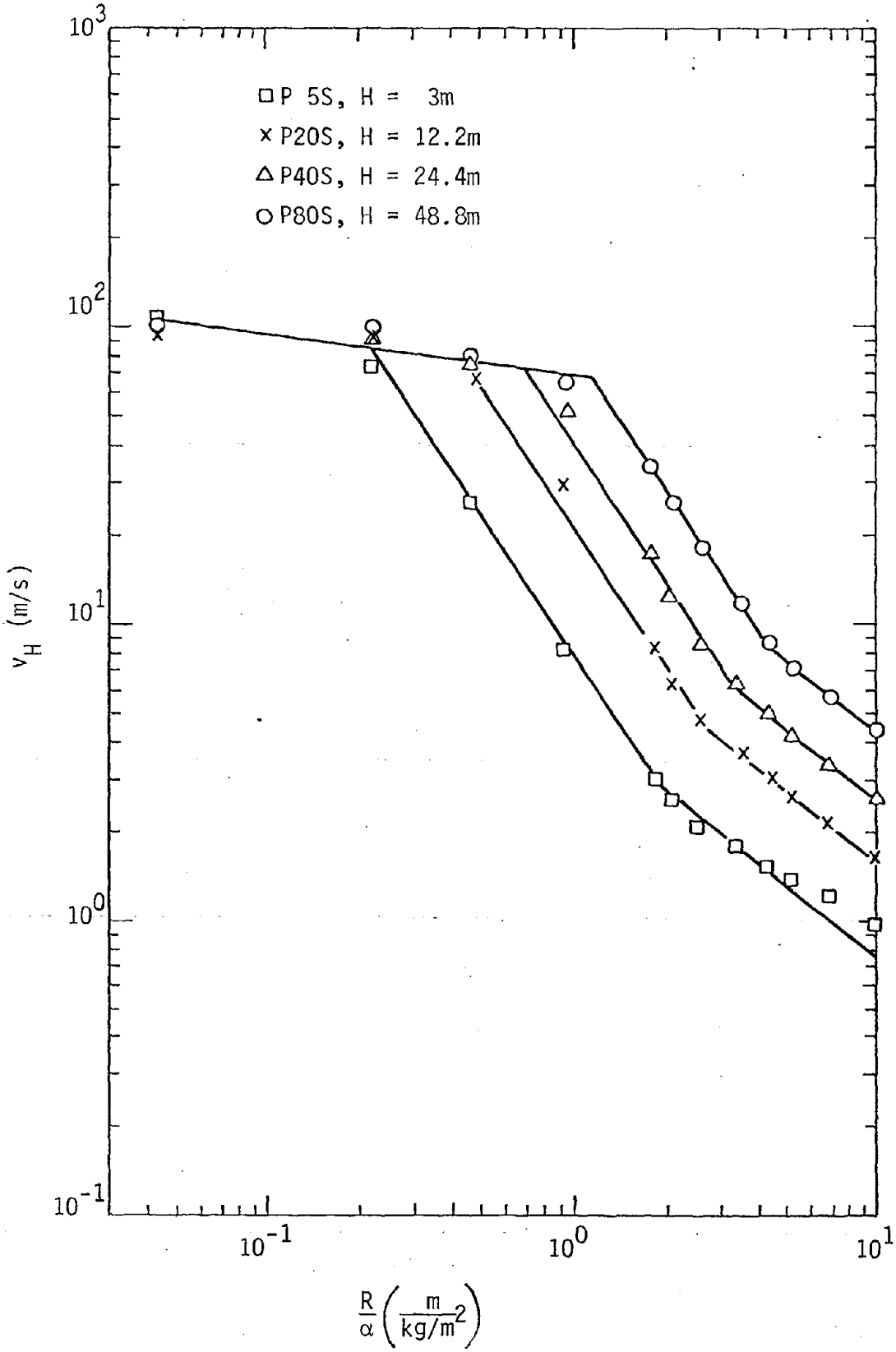

Figure 16. Effect of array height on calculated peak horizontal velocity; McCormick Ranch material model.

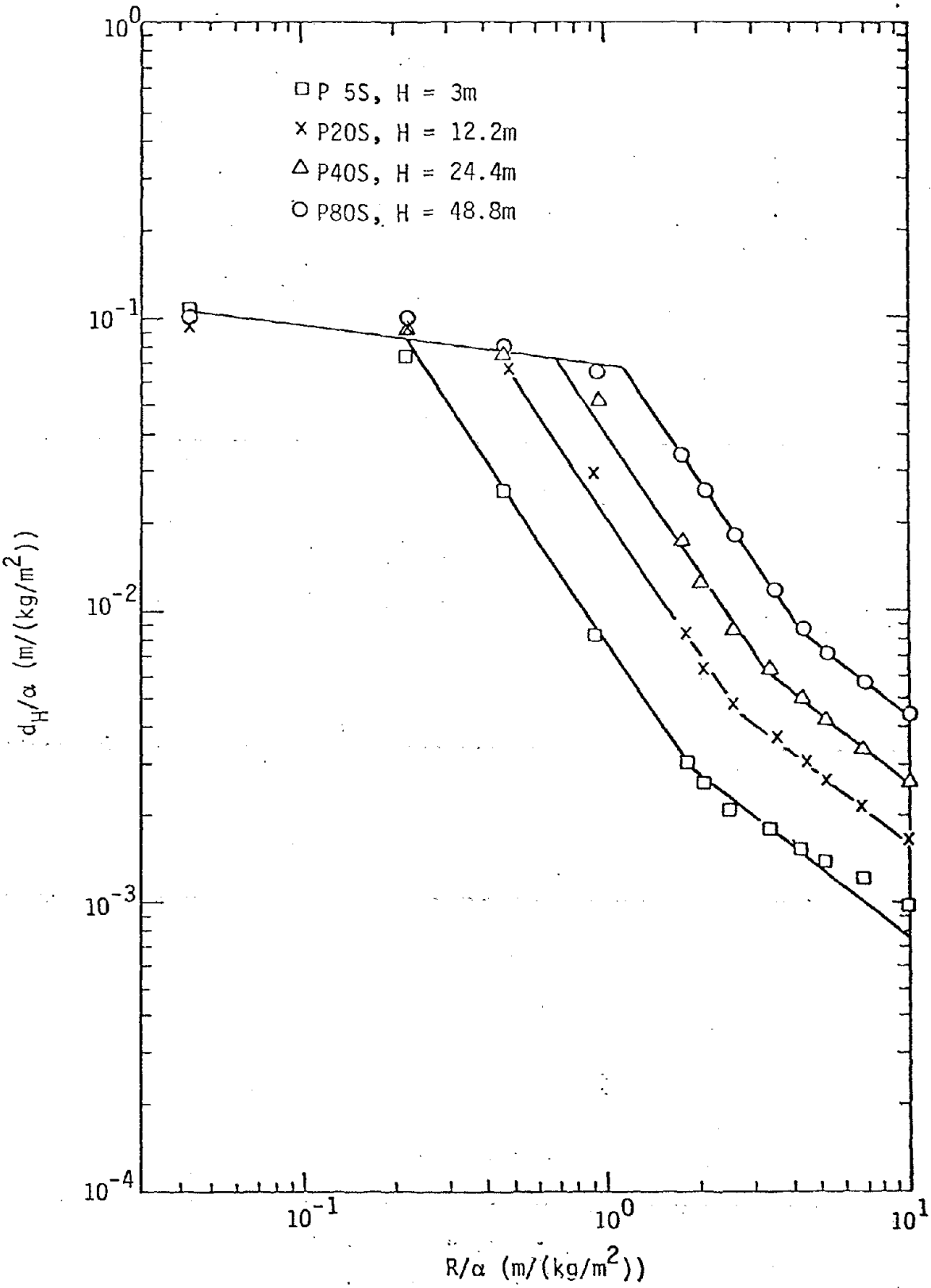

Figure 17. Effect of array height on calculated peak horizontal displacement; McCormick Ranch material model.

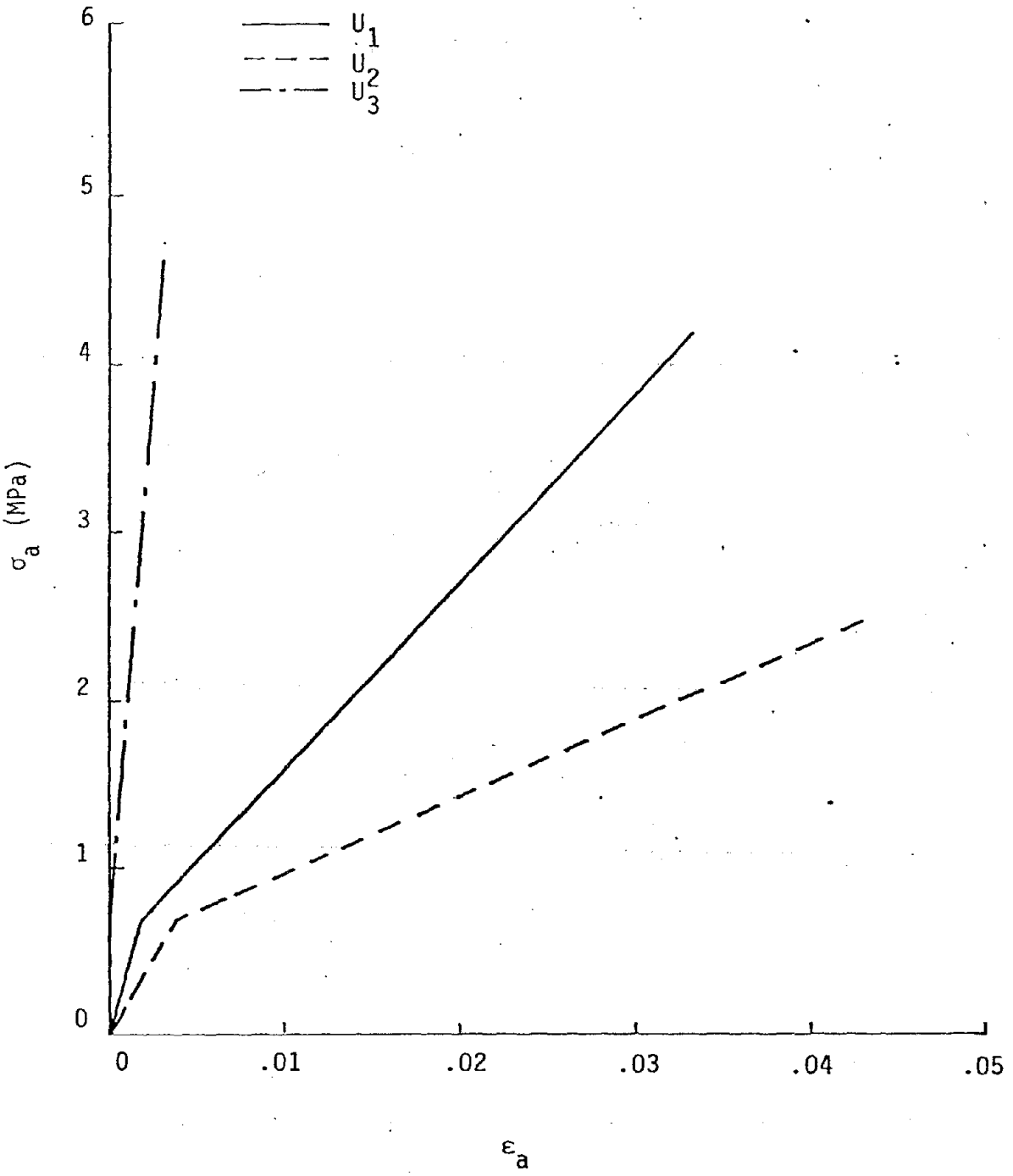

Figure 18. Uniaxial variations used in material property study.

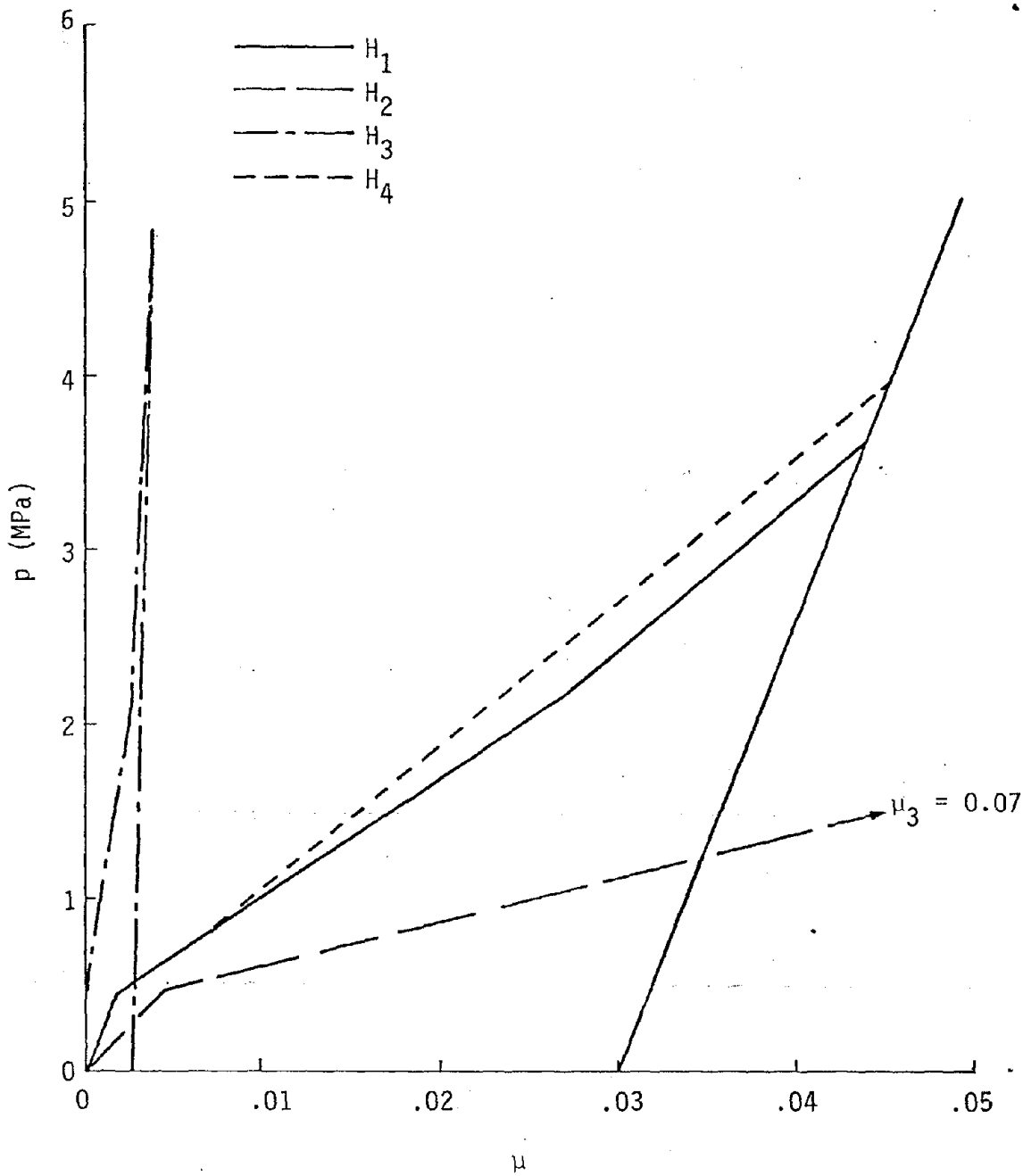

Figure 19. Hydrostat variations used in material property study.

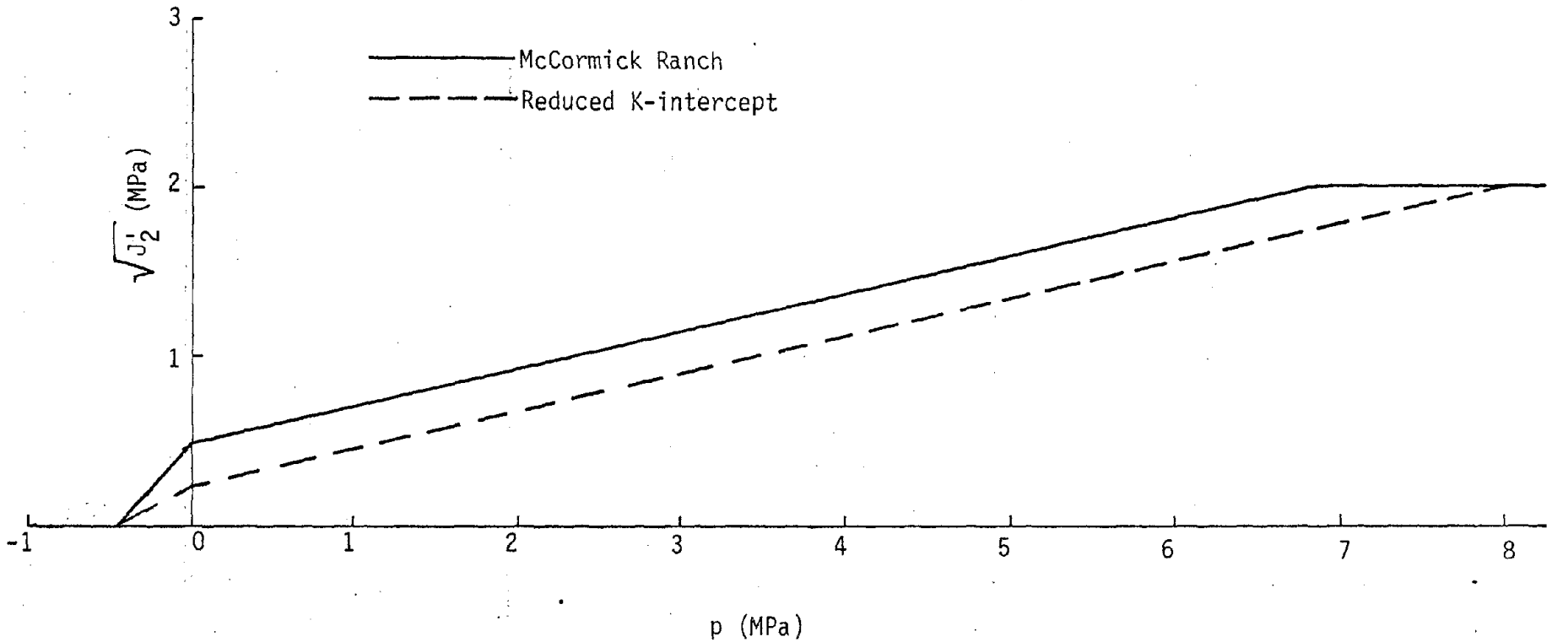

Figure 20. Variations in failure surface used in material property study.

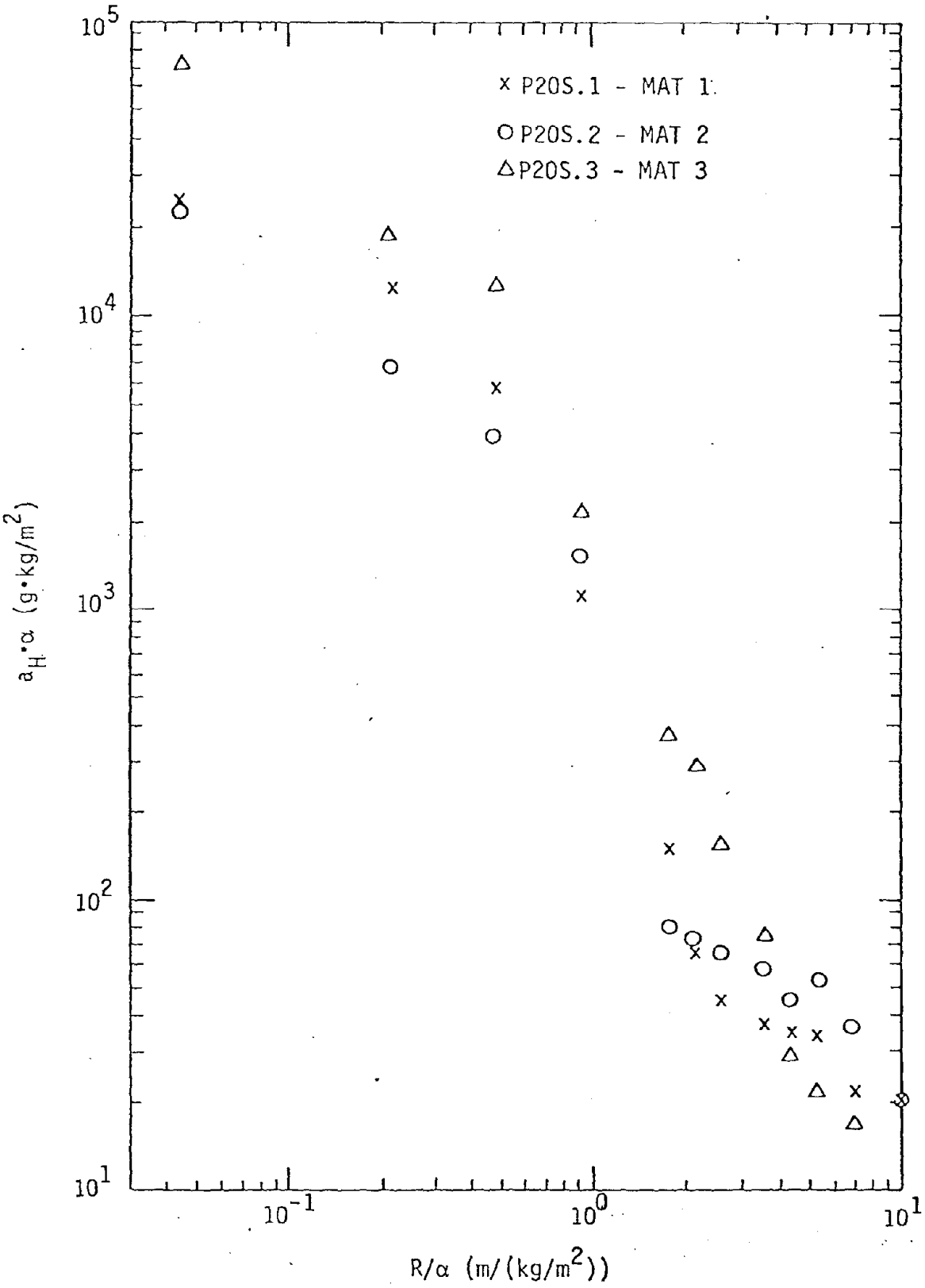

Figure 21. Effect of material stiffness on calculated peak horizontal acceleration, 12.2m array height.

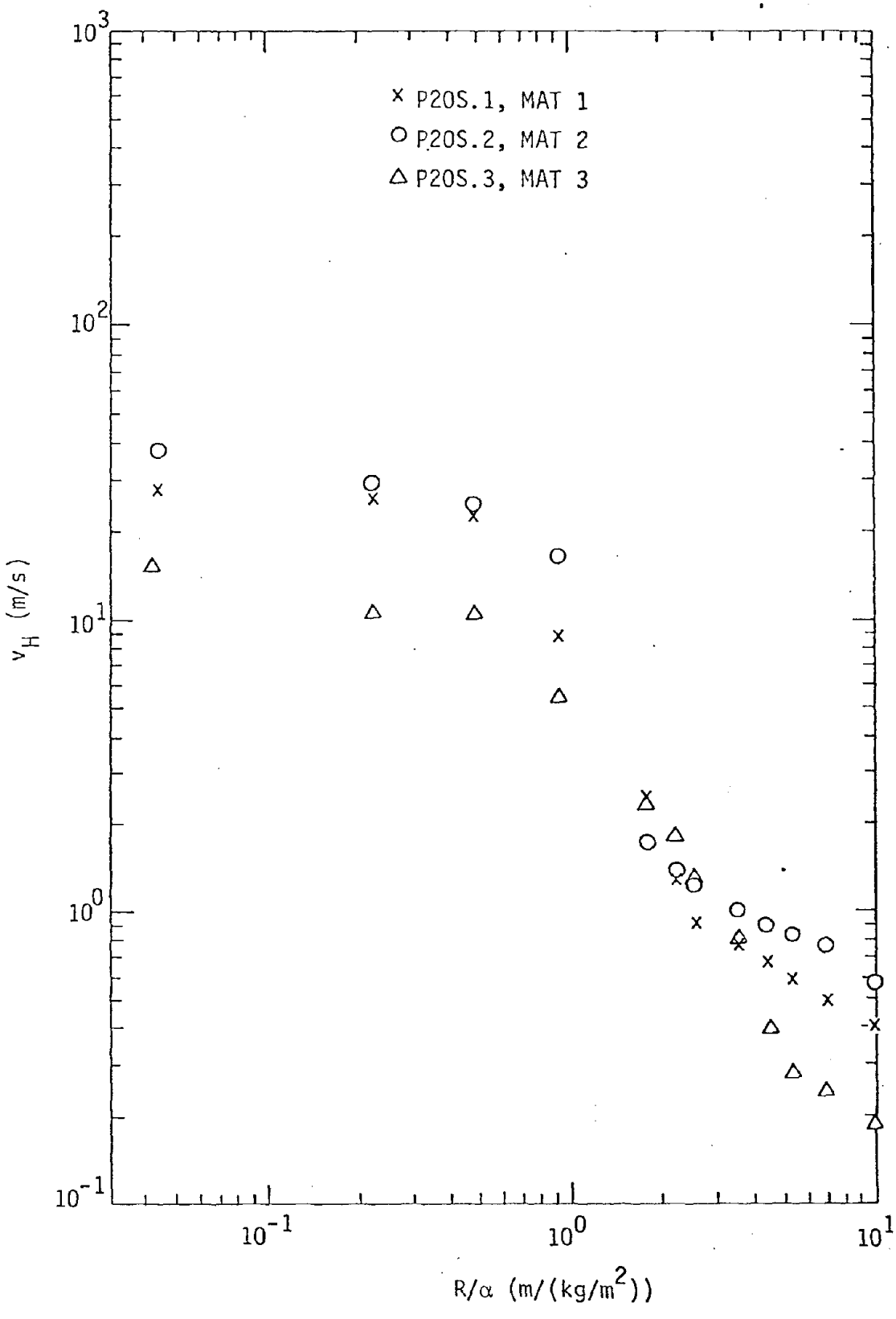

Figure 22. Effect of material stiffness on calculated peak horizontal velocity, 12.2 m array height.

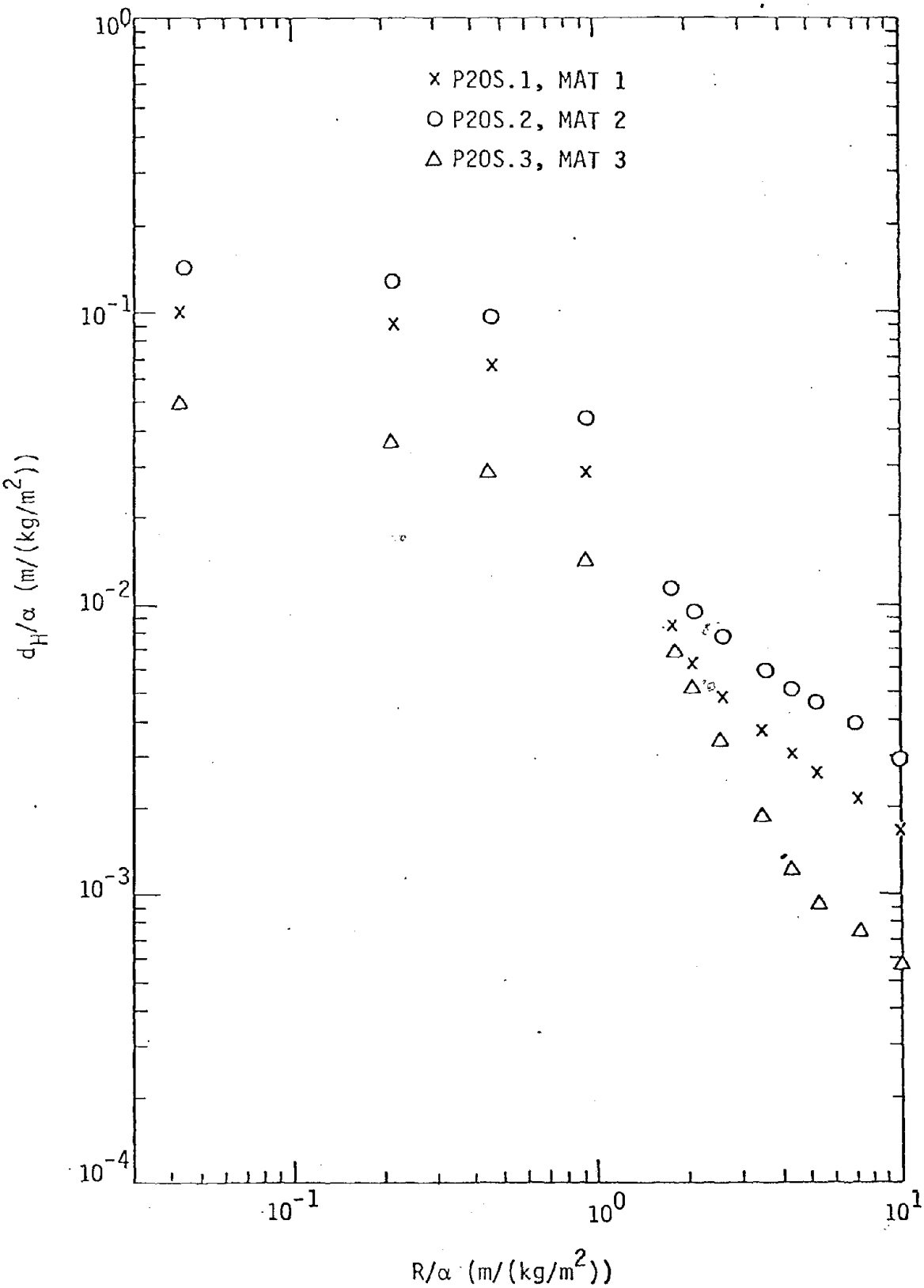

Figure 23. Effect of material stiffness on calculated peak horizontal displacement, 12.2m array height.

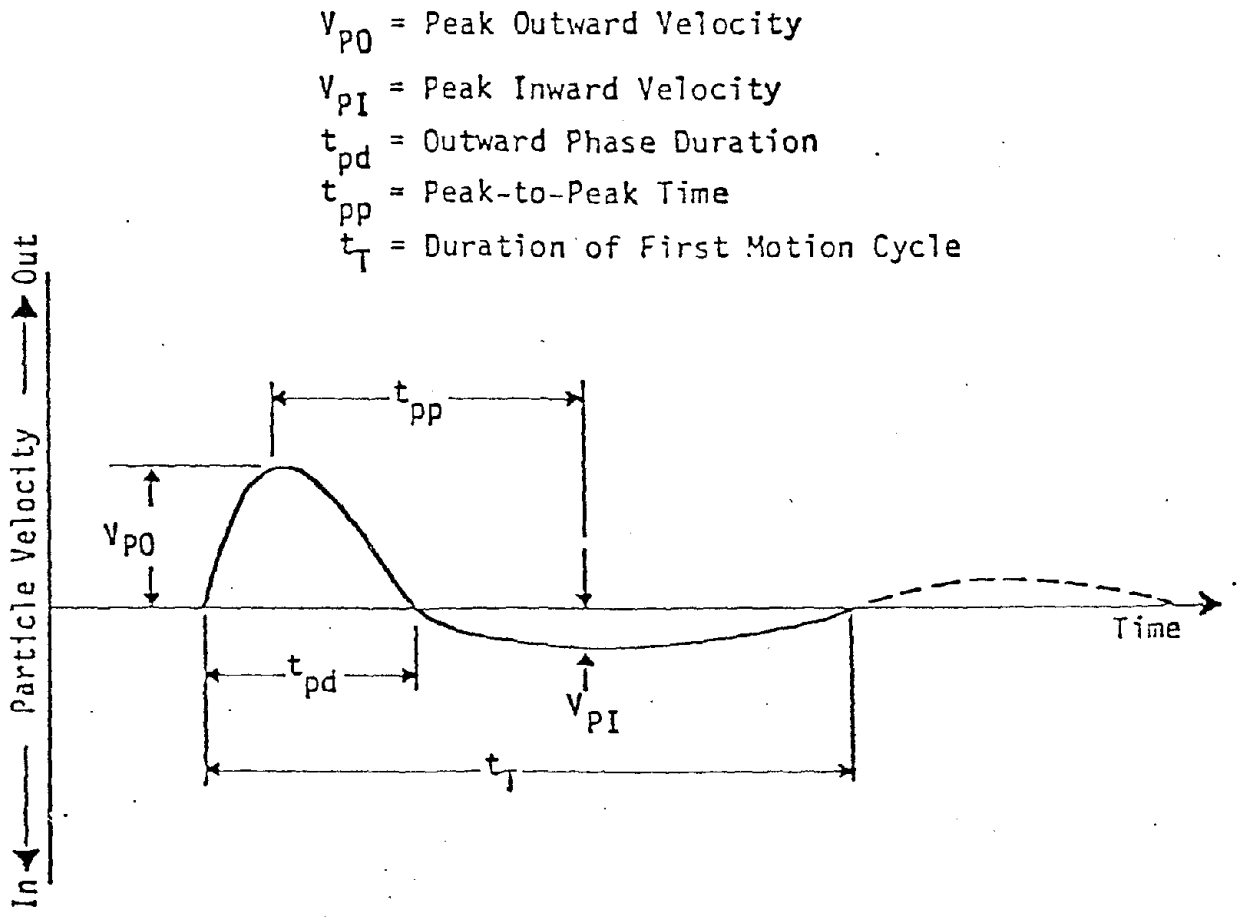

Figure 24. Idealized particle velocity time history from cylindrical or planar explosion of finite dimensions.

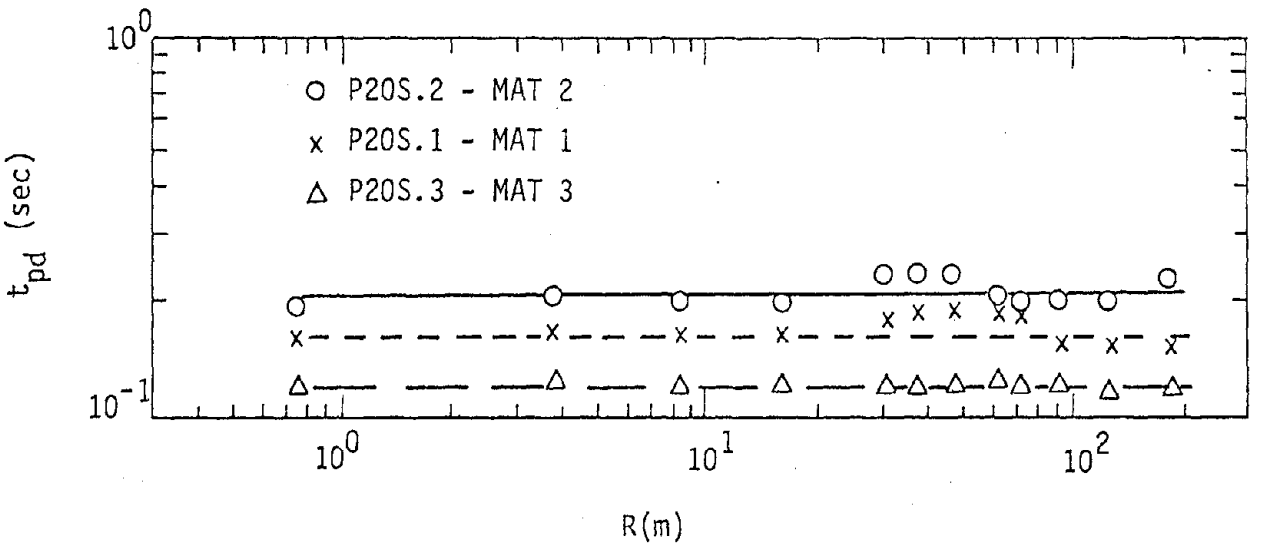

Figure 25. Horizontal velocity positive phase duration for material stiffness variations, 12.2m array height.

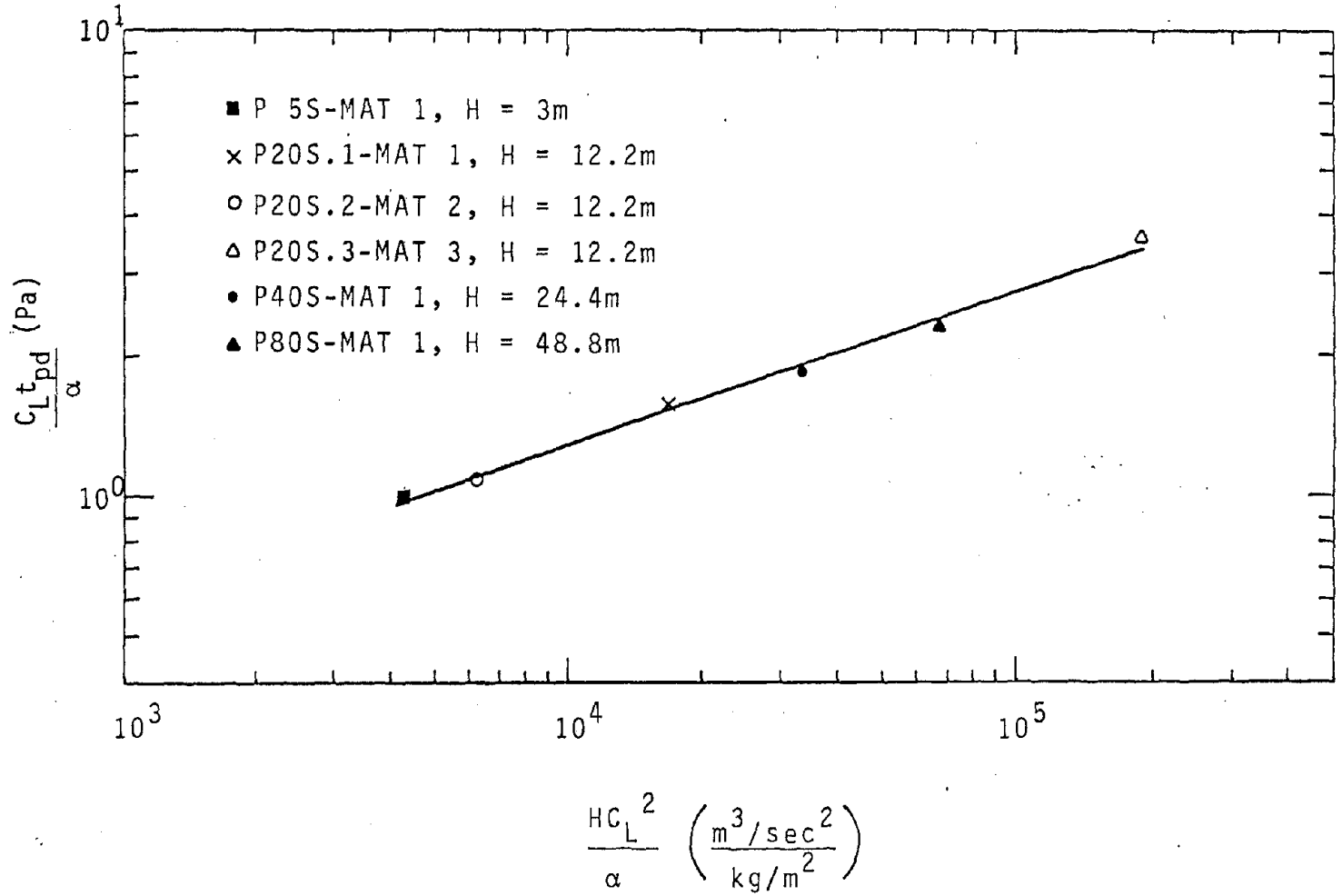

Figure 26. Relationship between array middepth horizontal velocity positive phase duration and array height and soil loading wave speed.

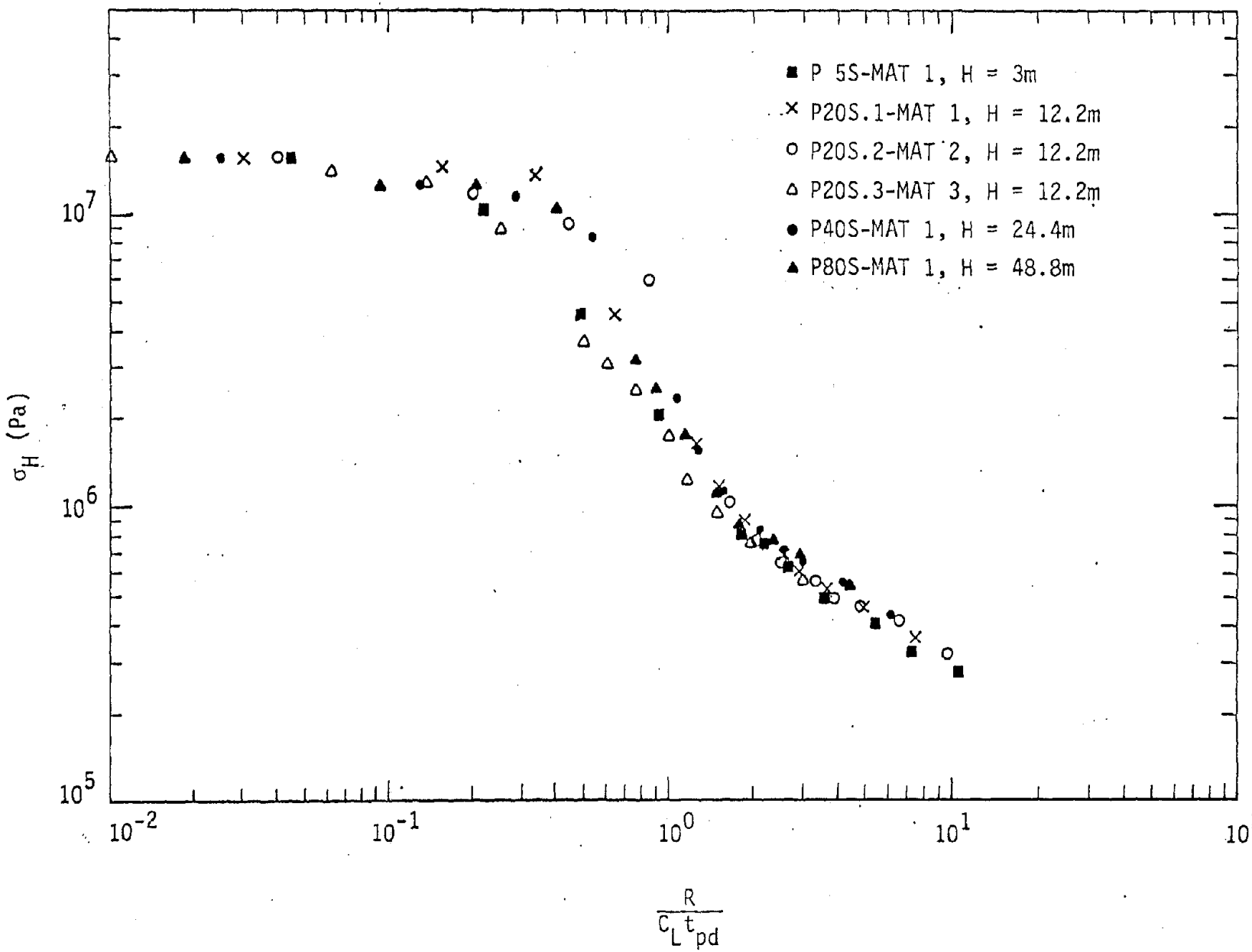

Figure 27. Effect of material loading wave speed and array height on calculated array middepth horizontal stresses.

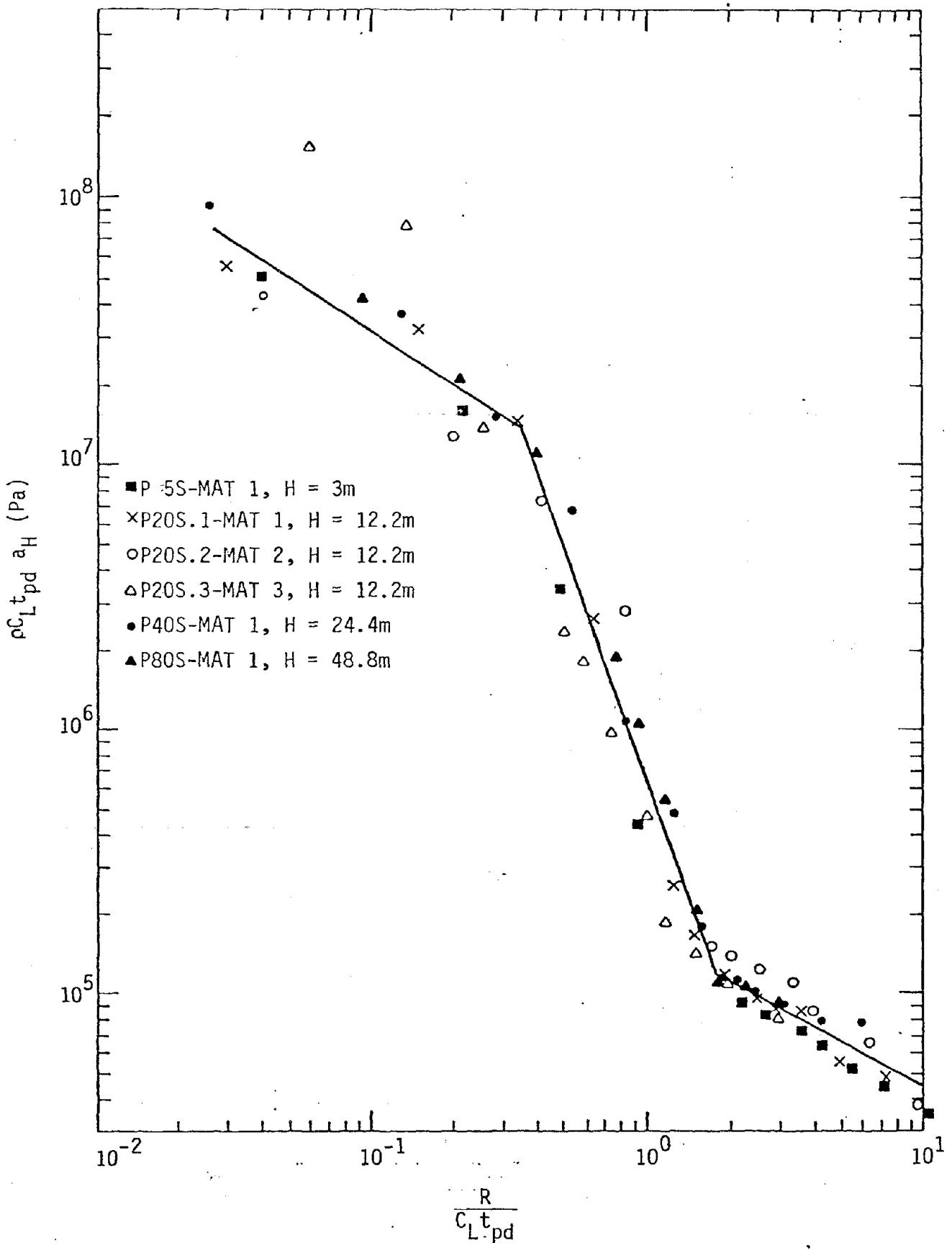

Figure 28. Effect of material loading wave speed and array height on calculated array middepth horizontal acceleration.

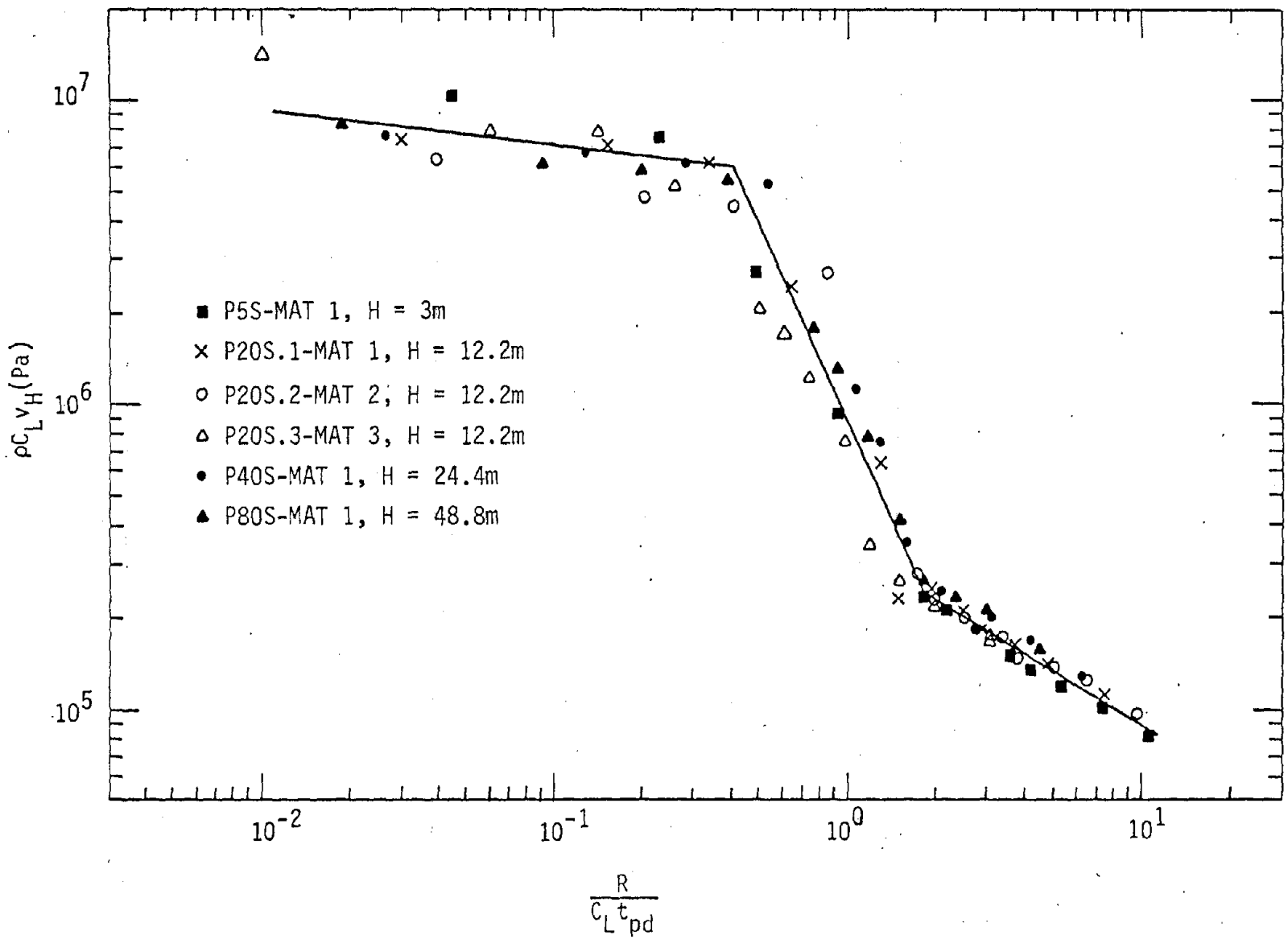

Figure 29. Effect of material loading wave speed and array height on calculated array middepth horizontal velocities.

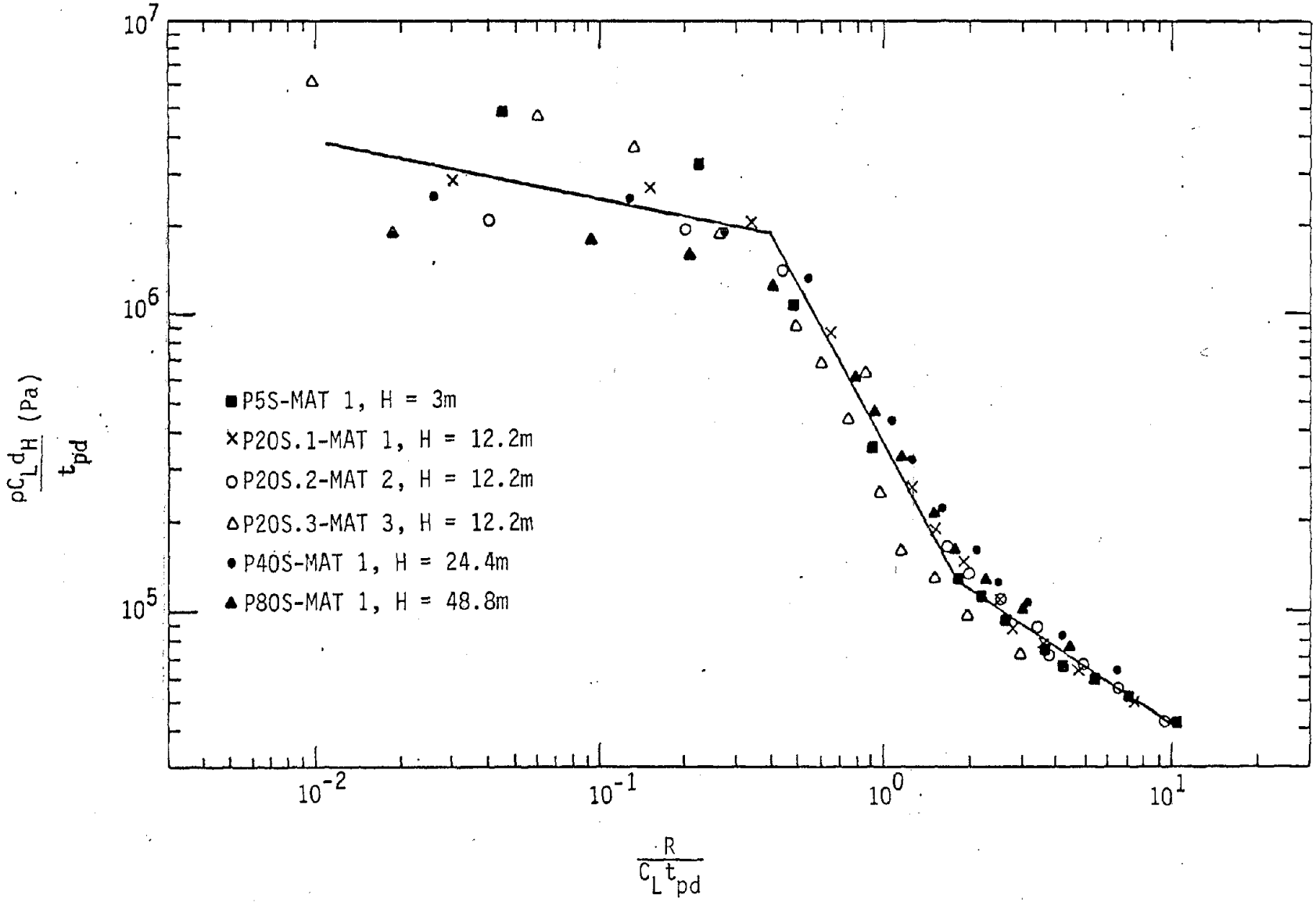

Figure 30. Effect of material loading wave speed and array height on calculated array middepth horizontal displacements.

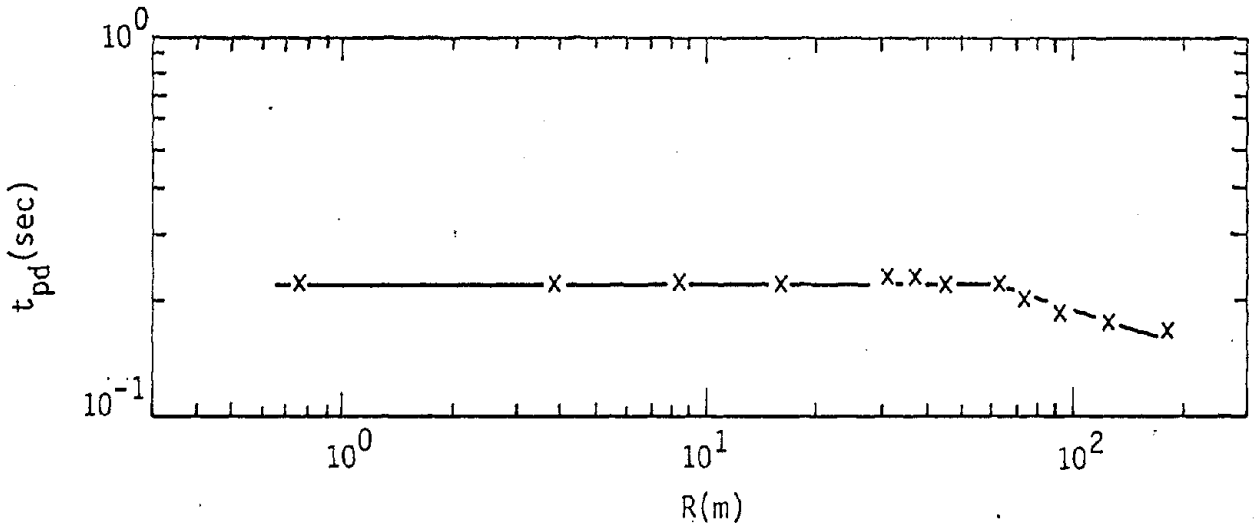

Figure 31. Horizontal velocity positive phase duration for calculation P20S.4, failure surface variation, 12.2 m array height.

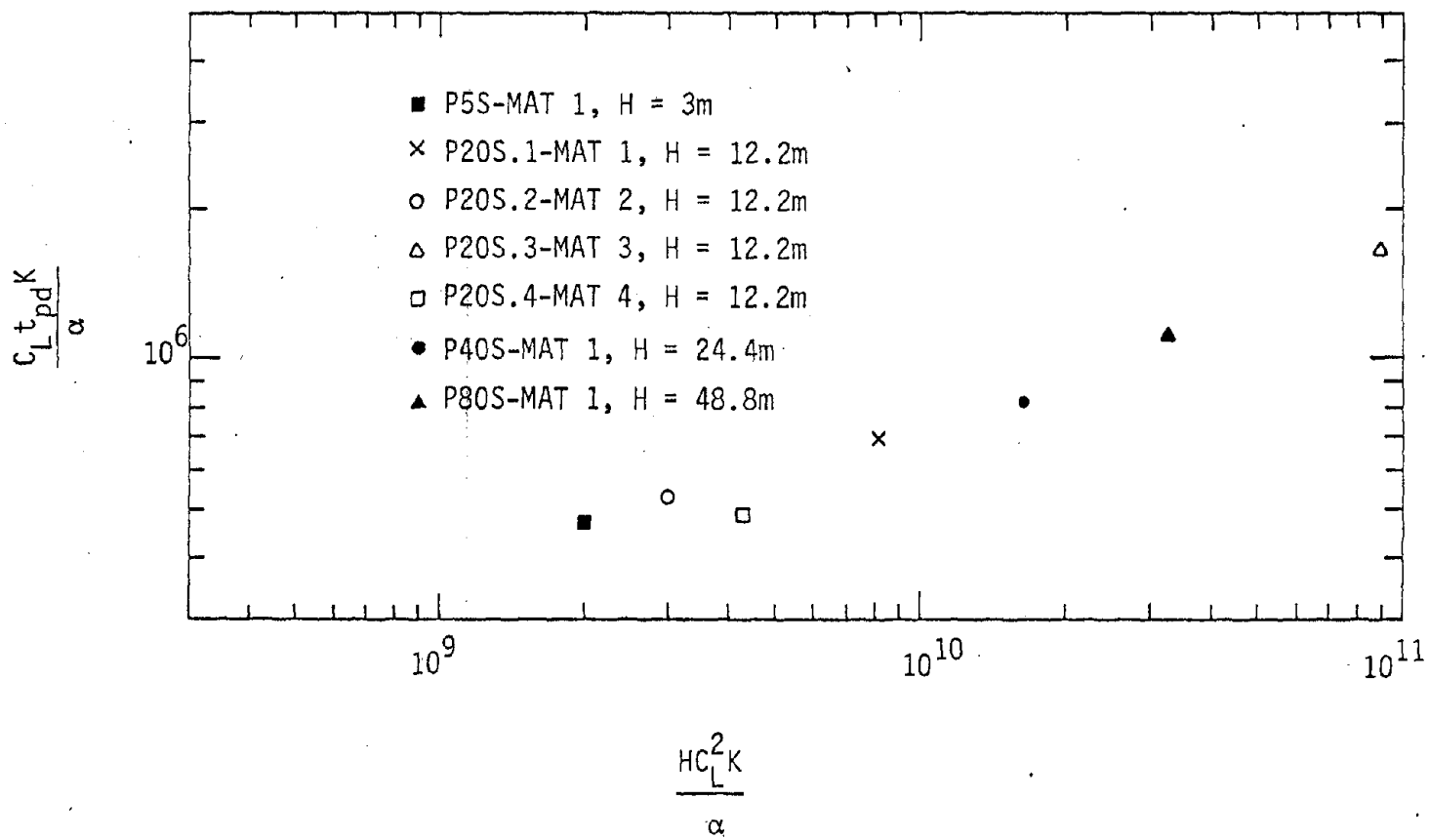

Figure 32. Effect of material loading wave speed, array height and $\sqrt{J_2'}$ intercept on calculated horizontal velocity positive phase duration.

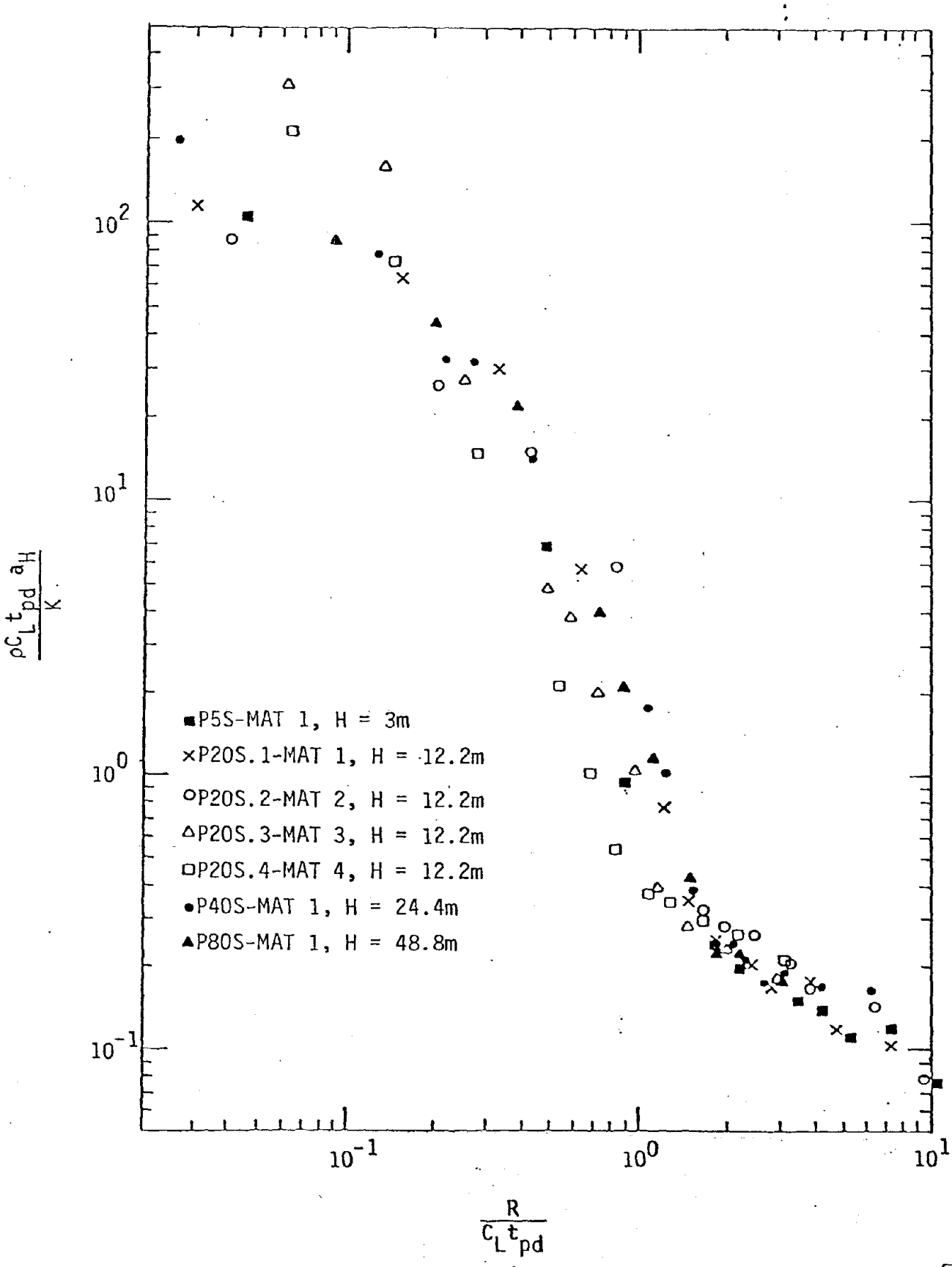

Figure 33. Effect of material loading wave speed, array height and $\sqrt{J_2'}$ intercept on calculated array middepth horizontal accelerations.

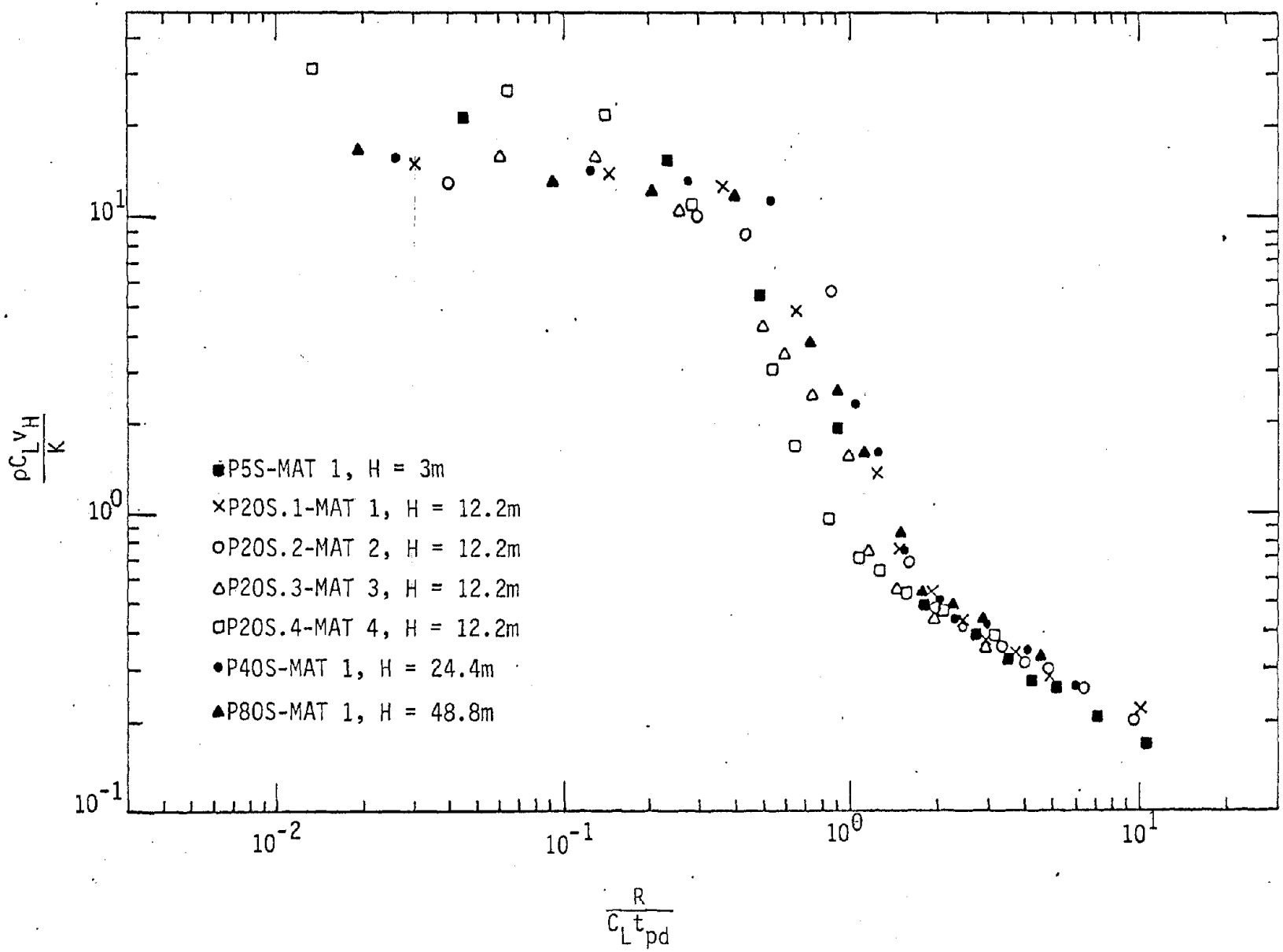

Figure 34. Effect of material loading wave speed, array height and $\sqrt{J_2'}$ intercept on calculated array middepth horizontal velocity.

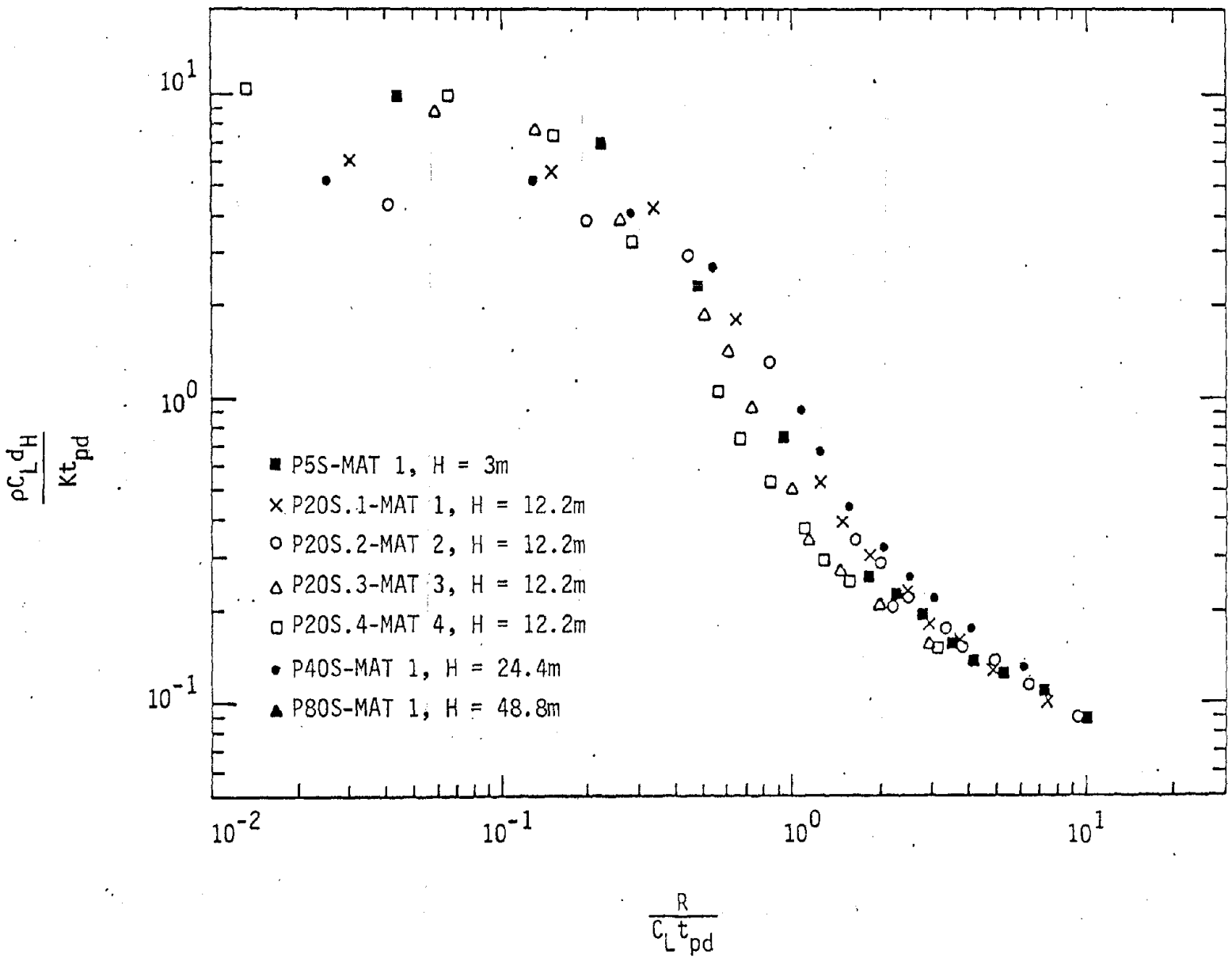

Figure 35. Effect of material loading wave speed, array height and $\sqrt{J_2'}$ intercept on calculated array middepth horizontal displacement.

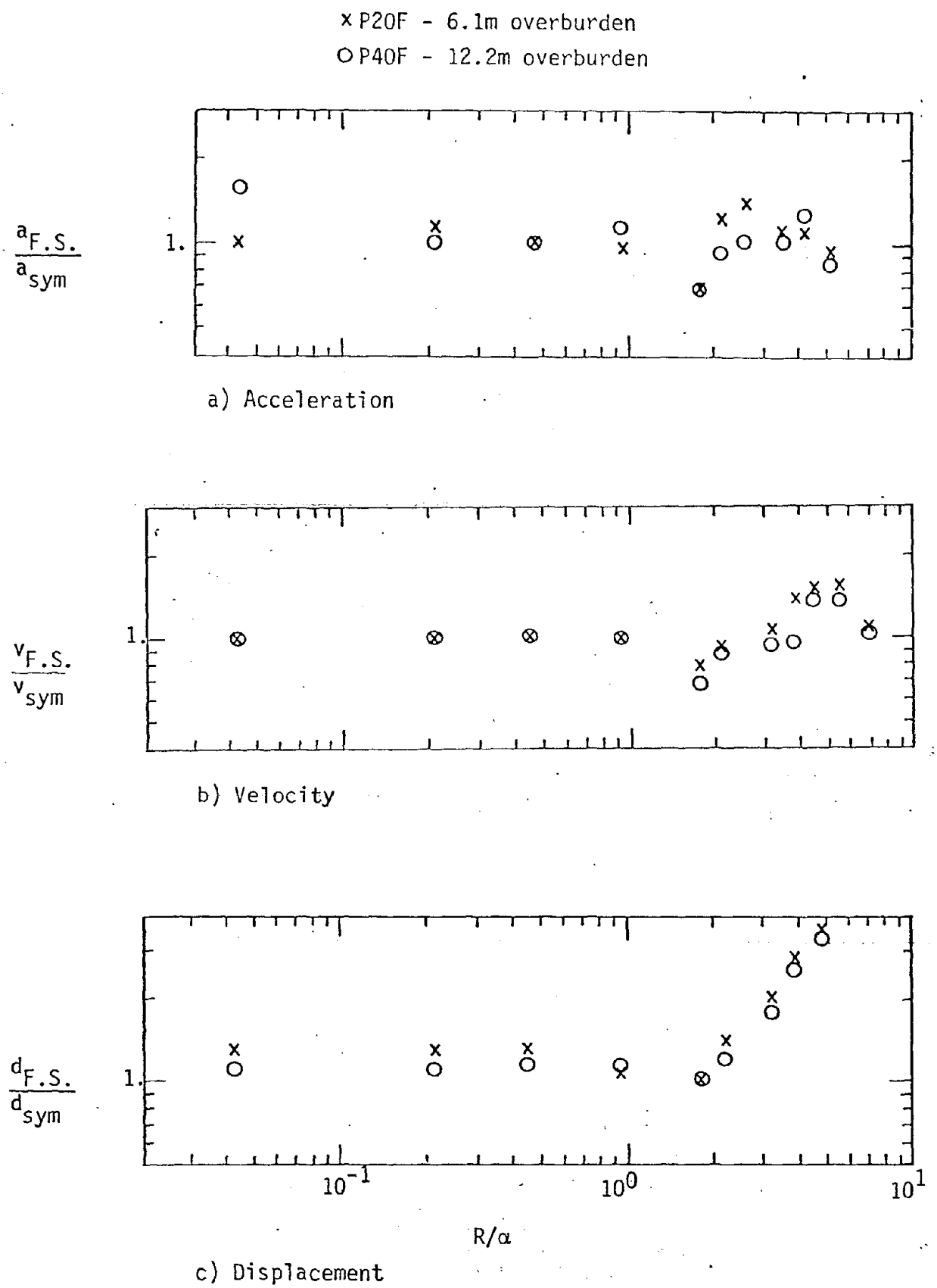

Figure 36. Horizontal motions at the array middepth; symmetric case compared to free surface case, 12.2m array height.

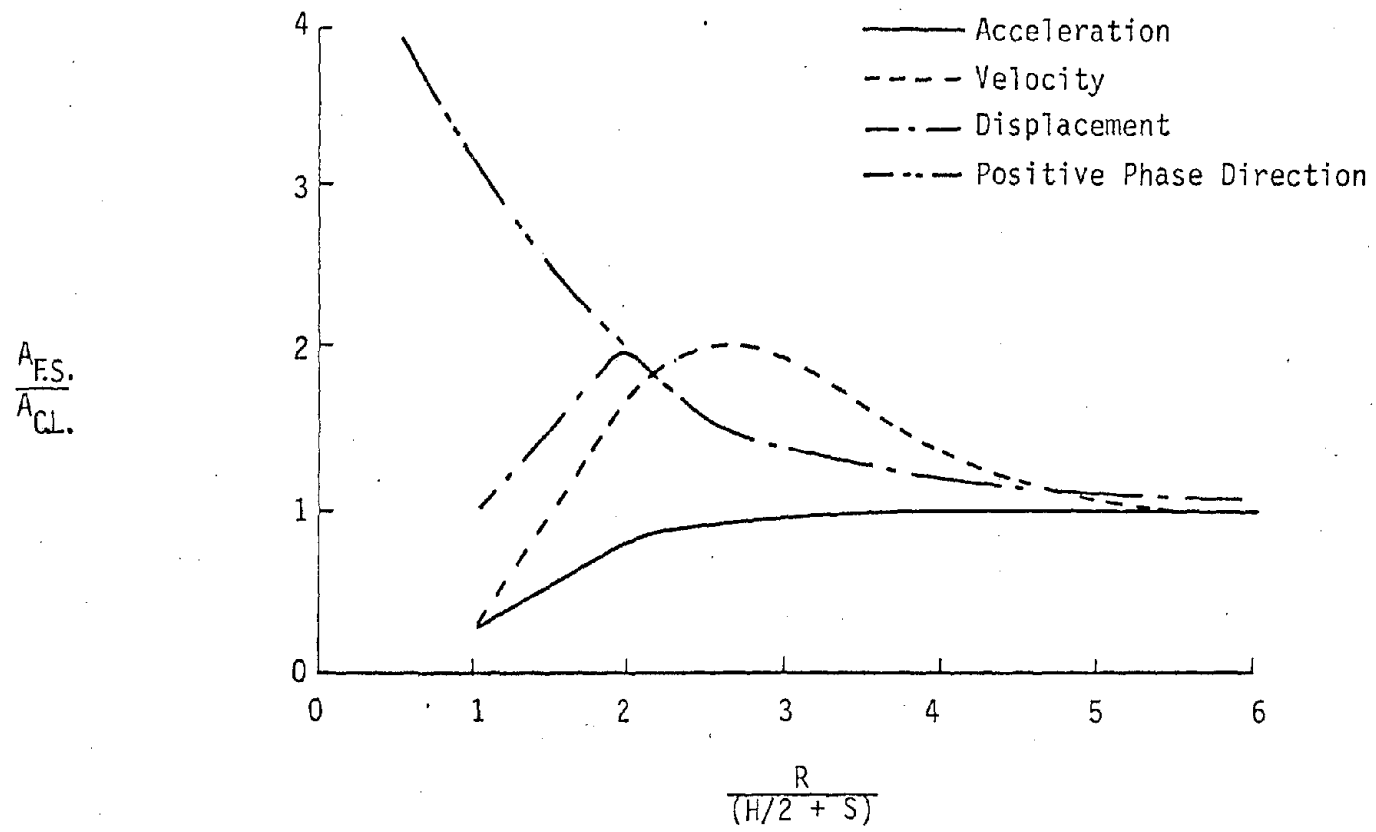

Figure 37. Calculated motion amplitudes at the free surface compared to calculated motion amplitudes at the array middepth.

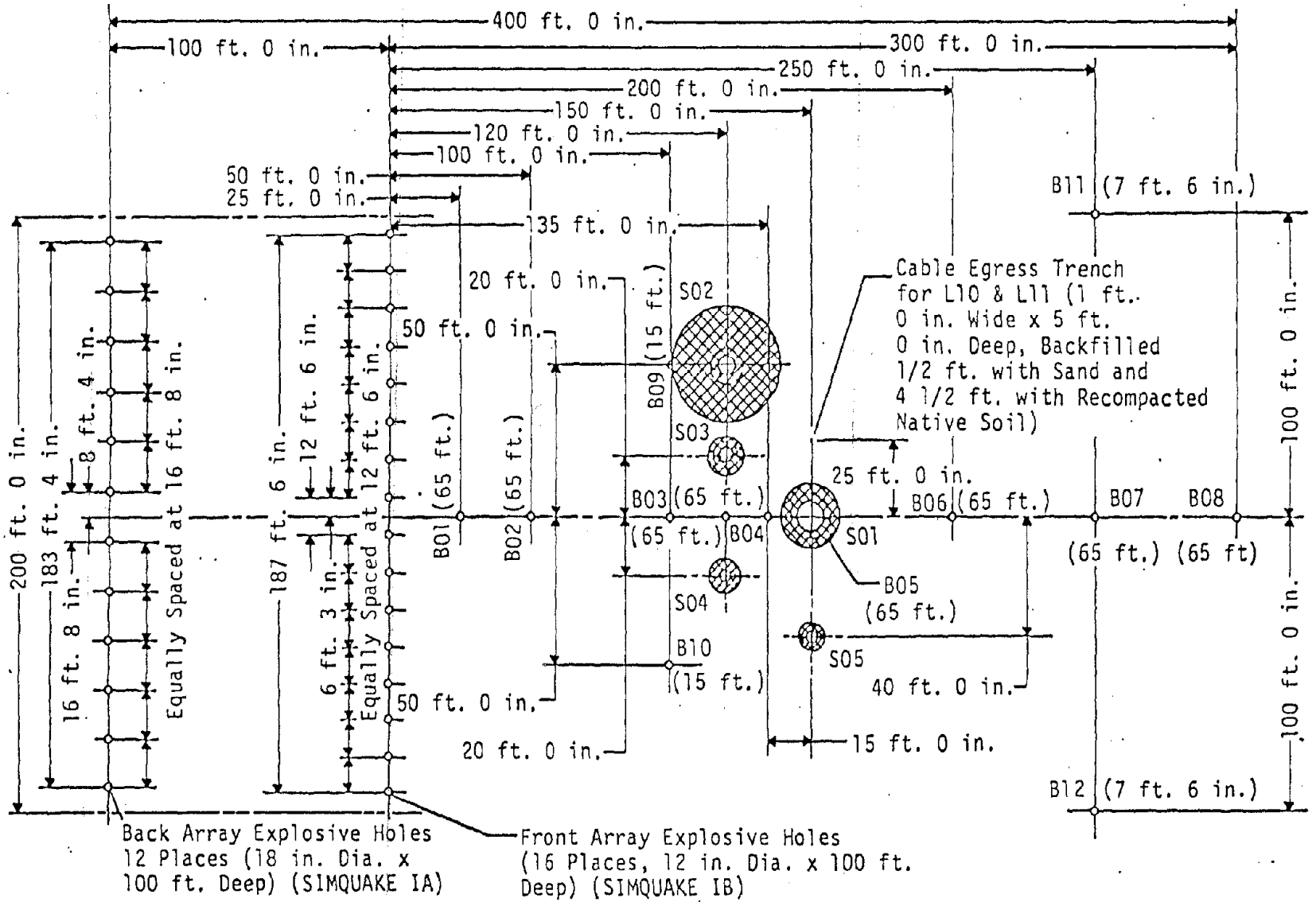

Figure 38. SIMQUAKE I - Testbed layout (ref. 7).

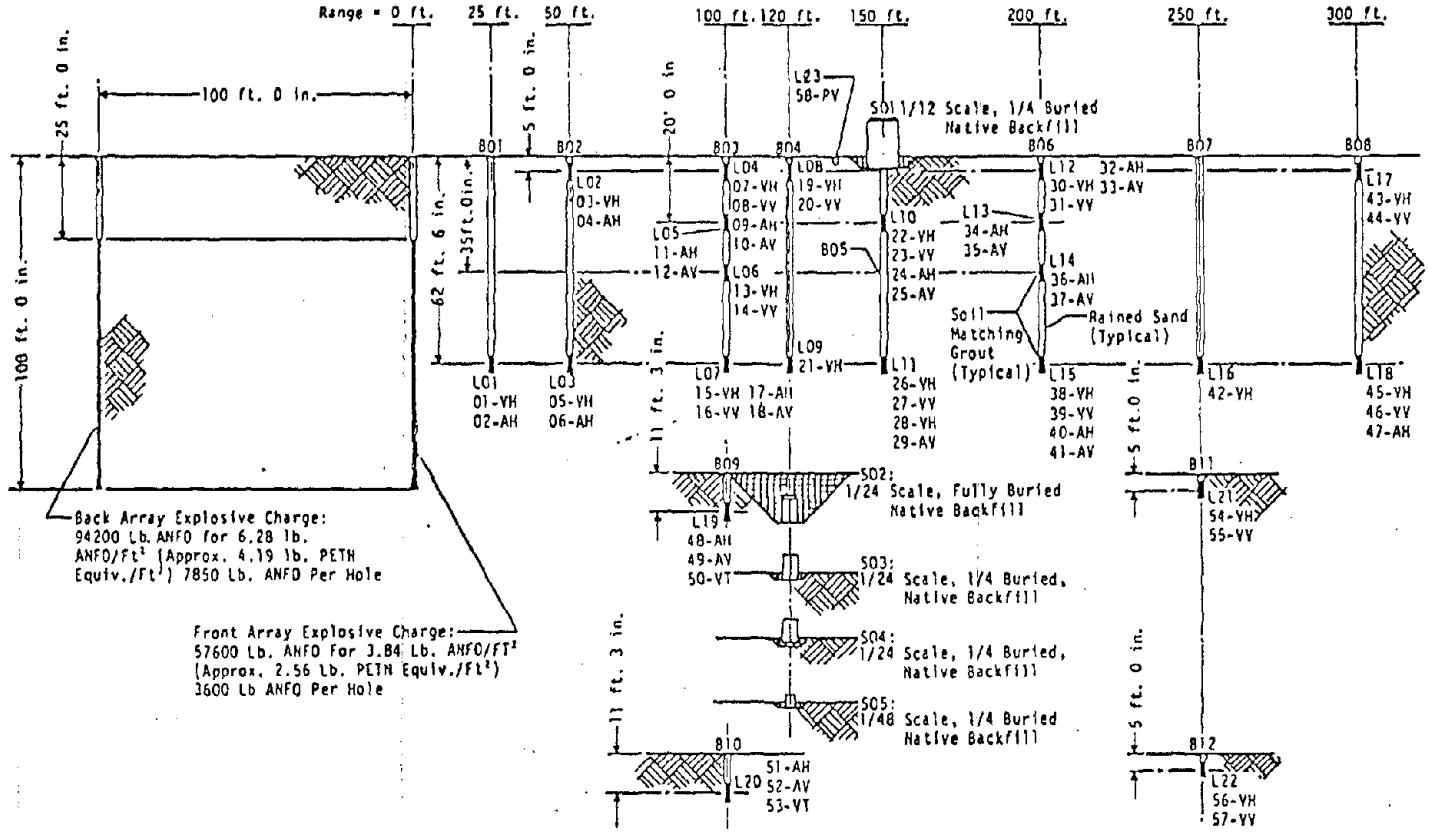

Notes:

1. See Sheets 2 thru 6 for Structural & Near Field Instrumentation Details.
2. See Sheet 7 of 7 for Detonation Details.
3. All Instrumentation Holes (B01 thru B12) to be 8 inches in diameter, Depth as Indicated, Mud Cake Lined.

Figure 39. SIMQUAKE I - Elevation View and instrumentation layout (ref. 7).

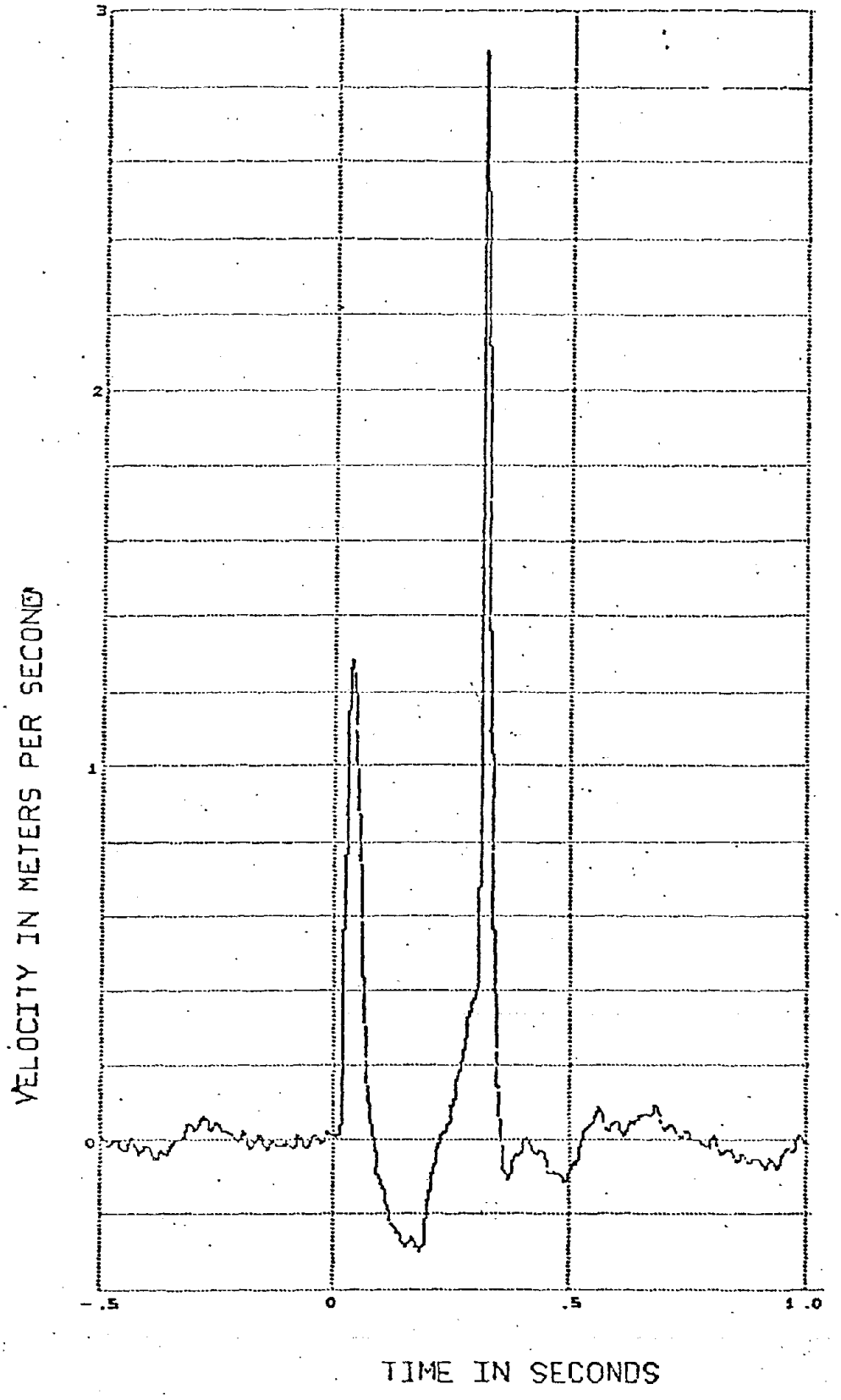

Figure 40. Typical velocity waveform measured in Mini-SIMQUAKE; array middepth, 10m range (ref. 7).

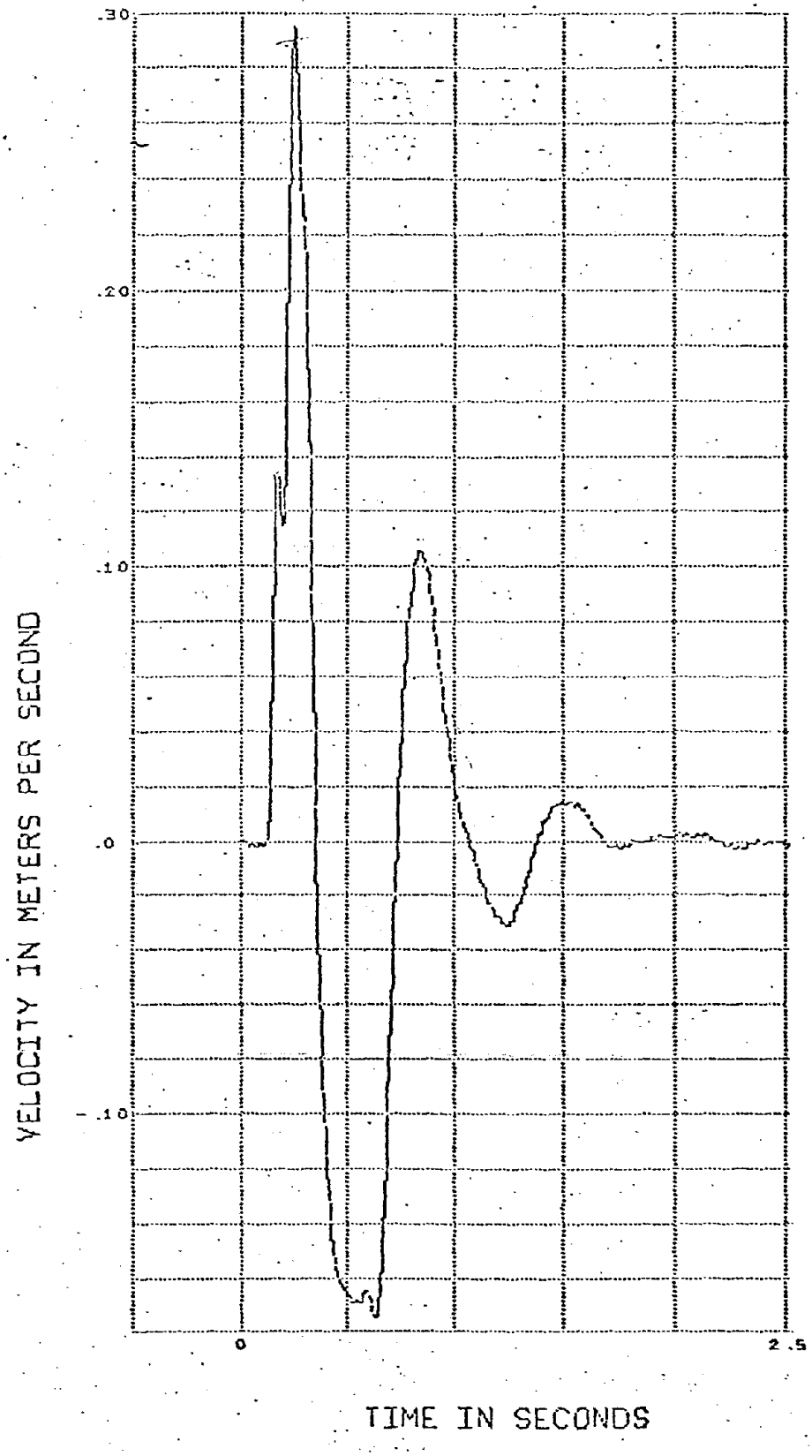

Figure 41. Typical velocity waveform measured in SIMQUAKE IA; array middepth, 61m range (ref. 7).

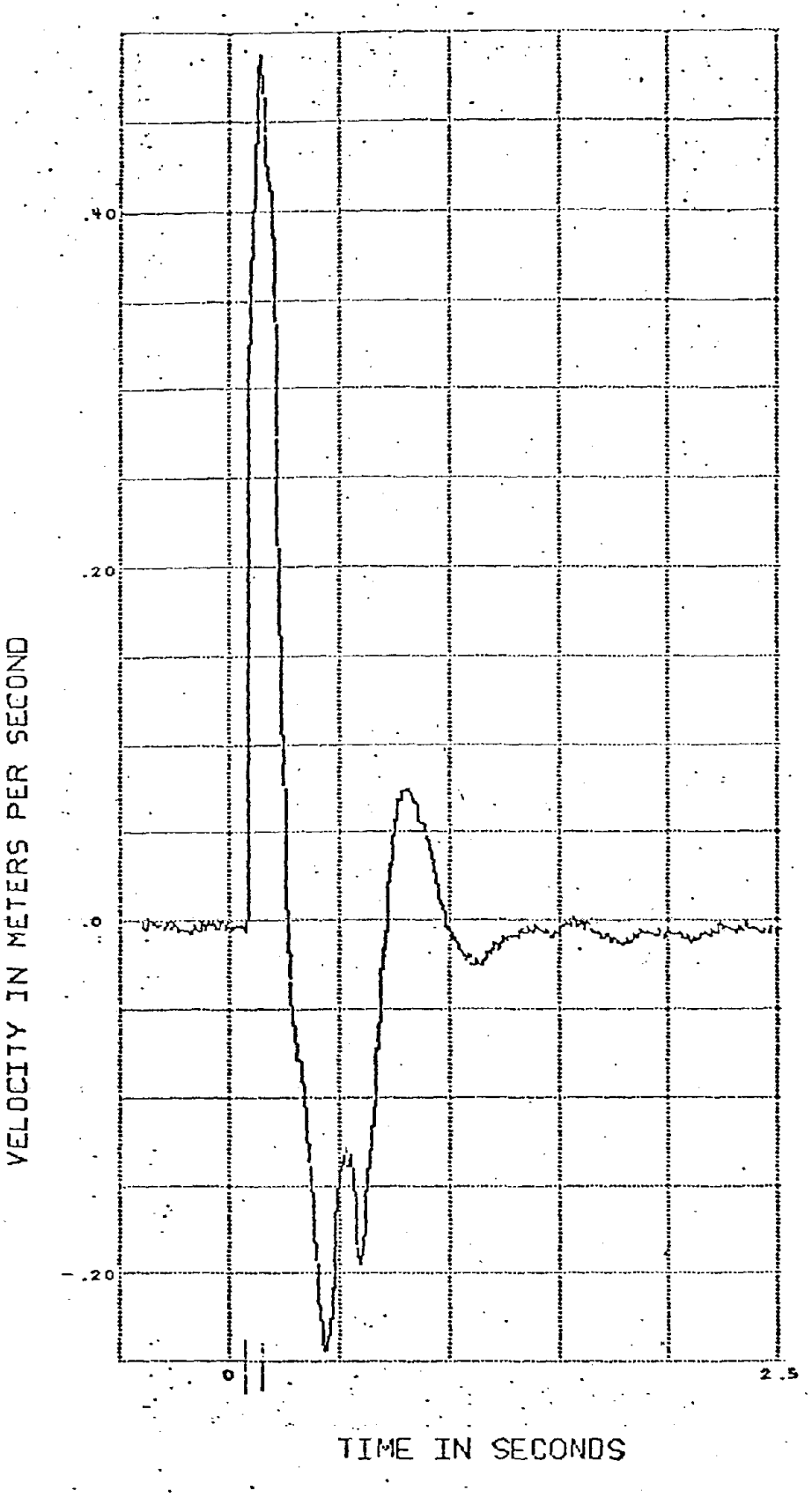

Figure 42. Typical velocity waveform measured in SIMQUAKE IB; array middepth, 46m range (ref. 7).

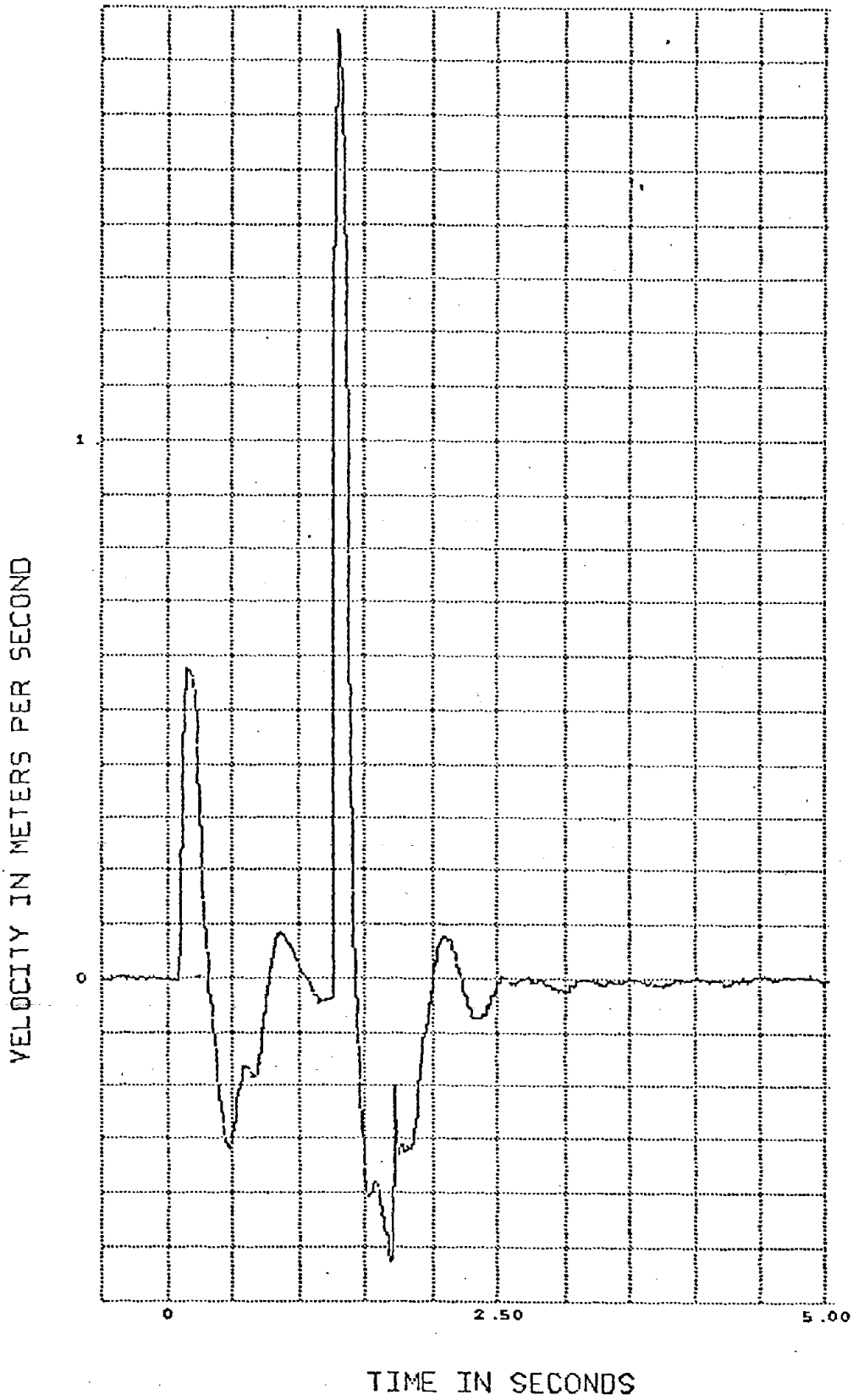

Figure 43. Typical velocity waveform measured in SIMQUAKE II; array middepth, 30.5m range (ref. 8).

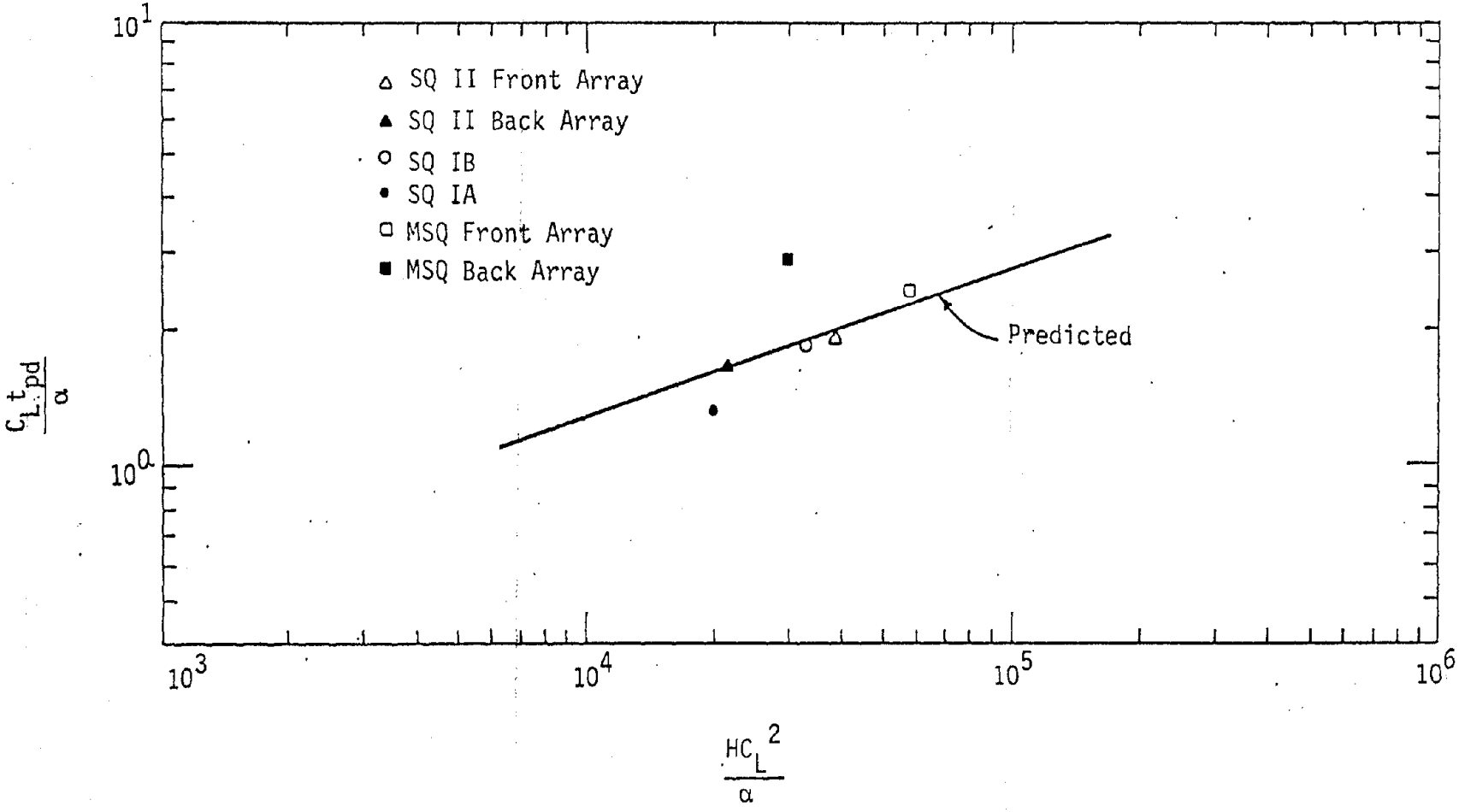

Figure 44. Measured SIMQUAKE array middepth horizontal velocity positive phase durations compared with prediction.

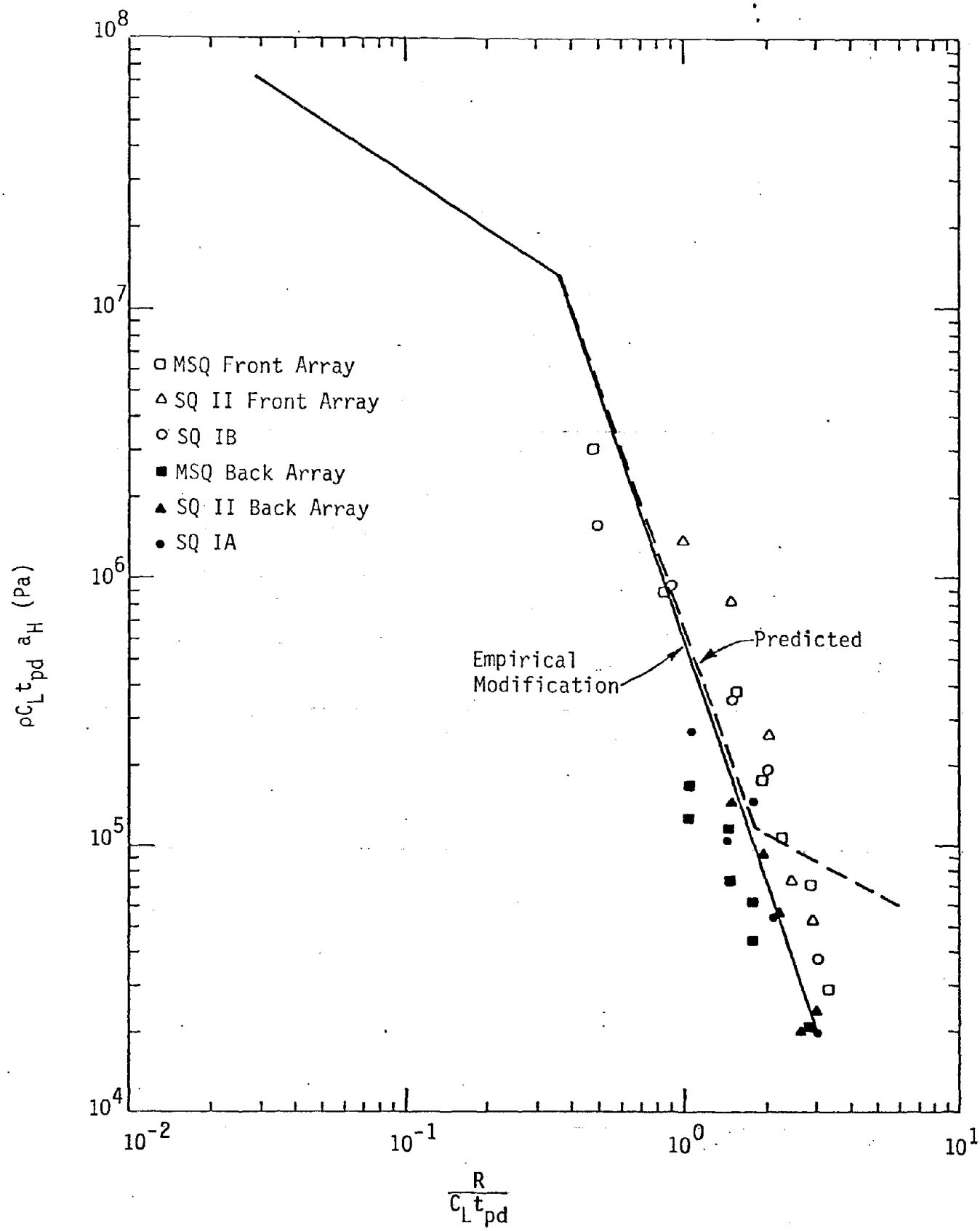

Figure 45. Measured SIMQUAKE array middepth peak horizontal accelerations compared with prediction.

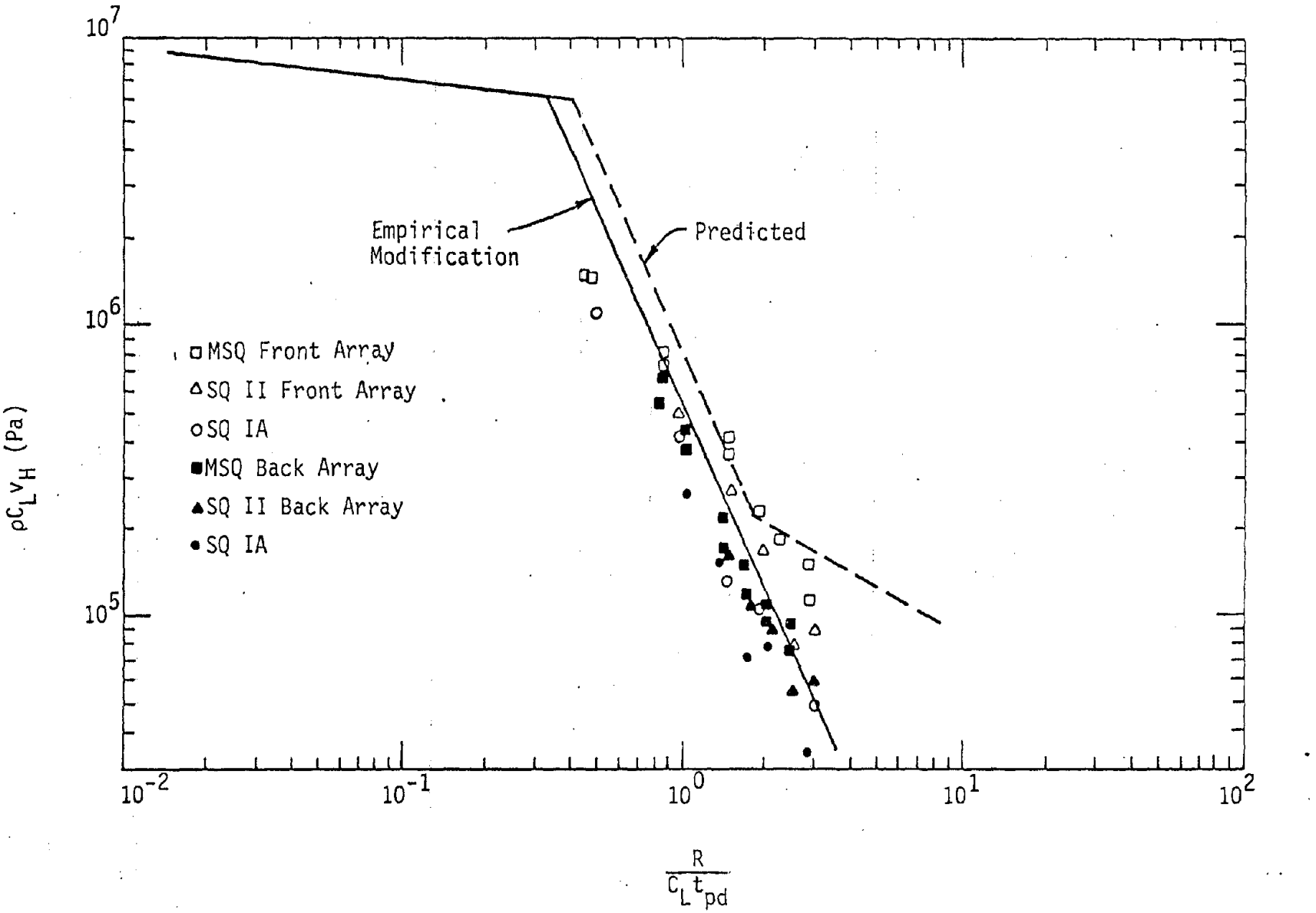

Figure 46. Measured SIMQUAKE array middepth peak horizontal velocity compared to prediction.

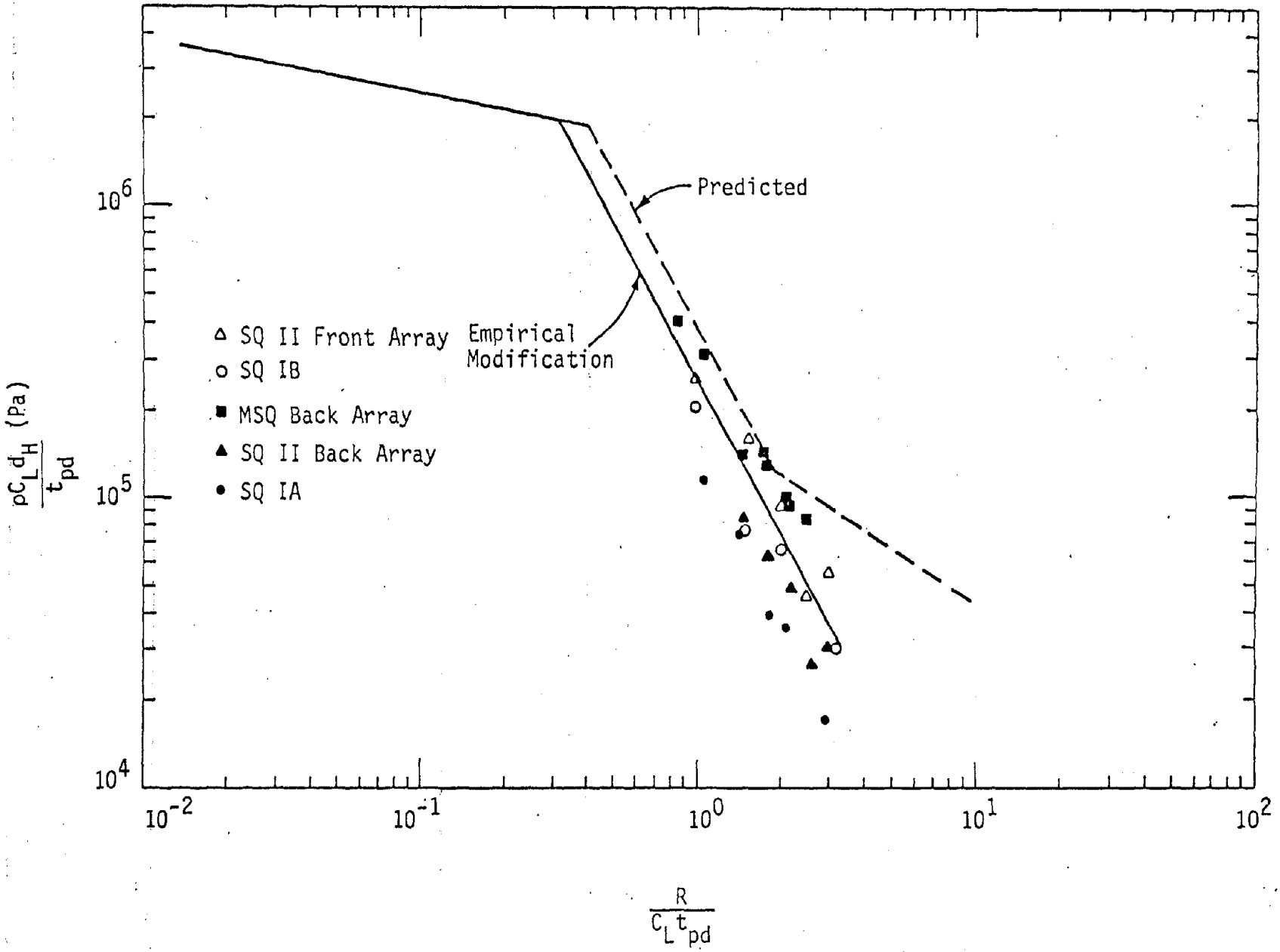

Figure 47. Measured SIMQUAKE array middepth peak horizontal displacements compared with prediction.

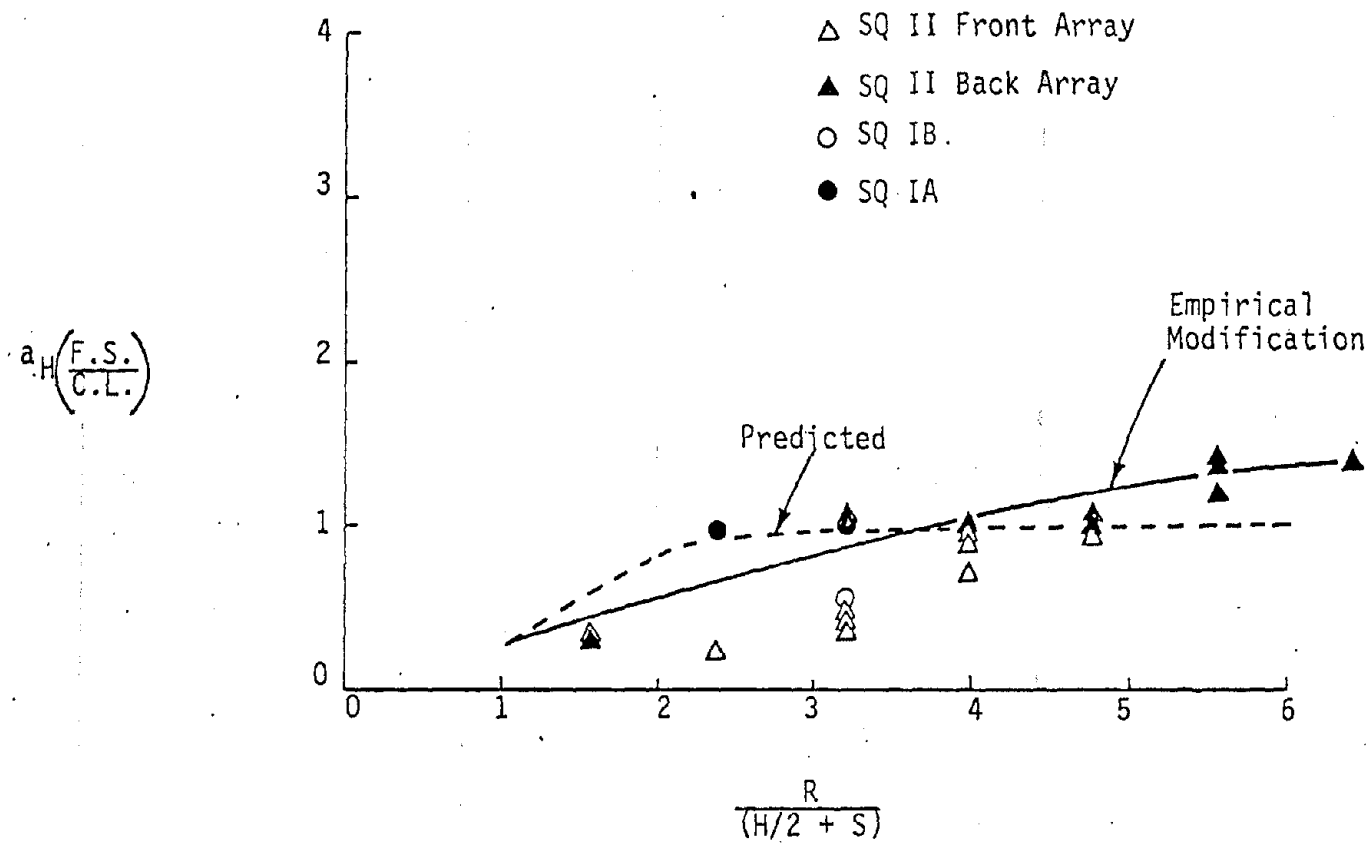

Figure 48. Ratios of measured SIMQUAKE free surface and centerline accelerations compared with predictions.

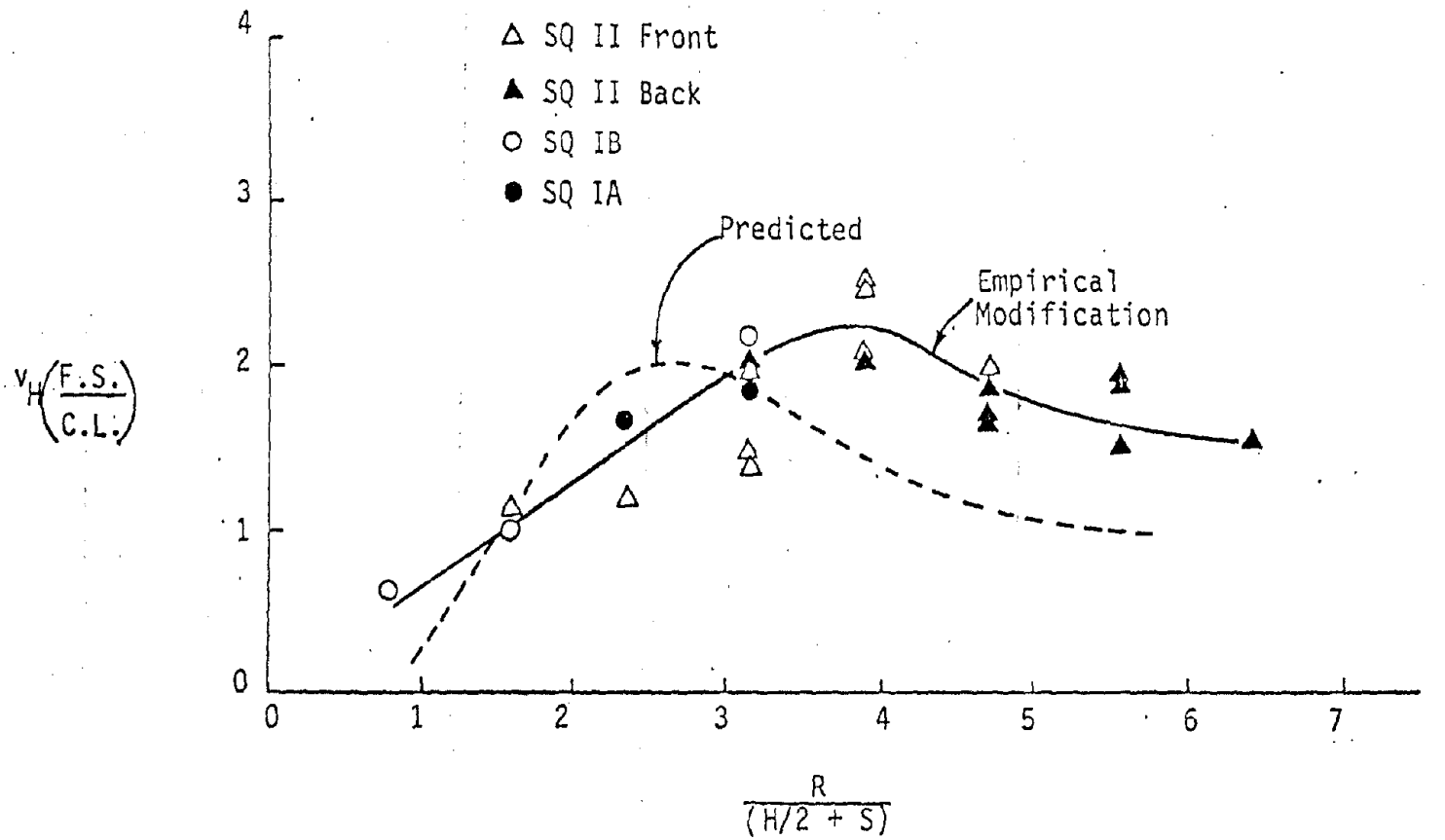

Figure 49. Ratios of measured SIMQUAKE free surface and centerline velocities compared with prediction.

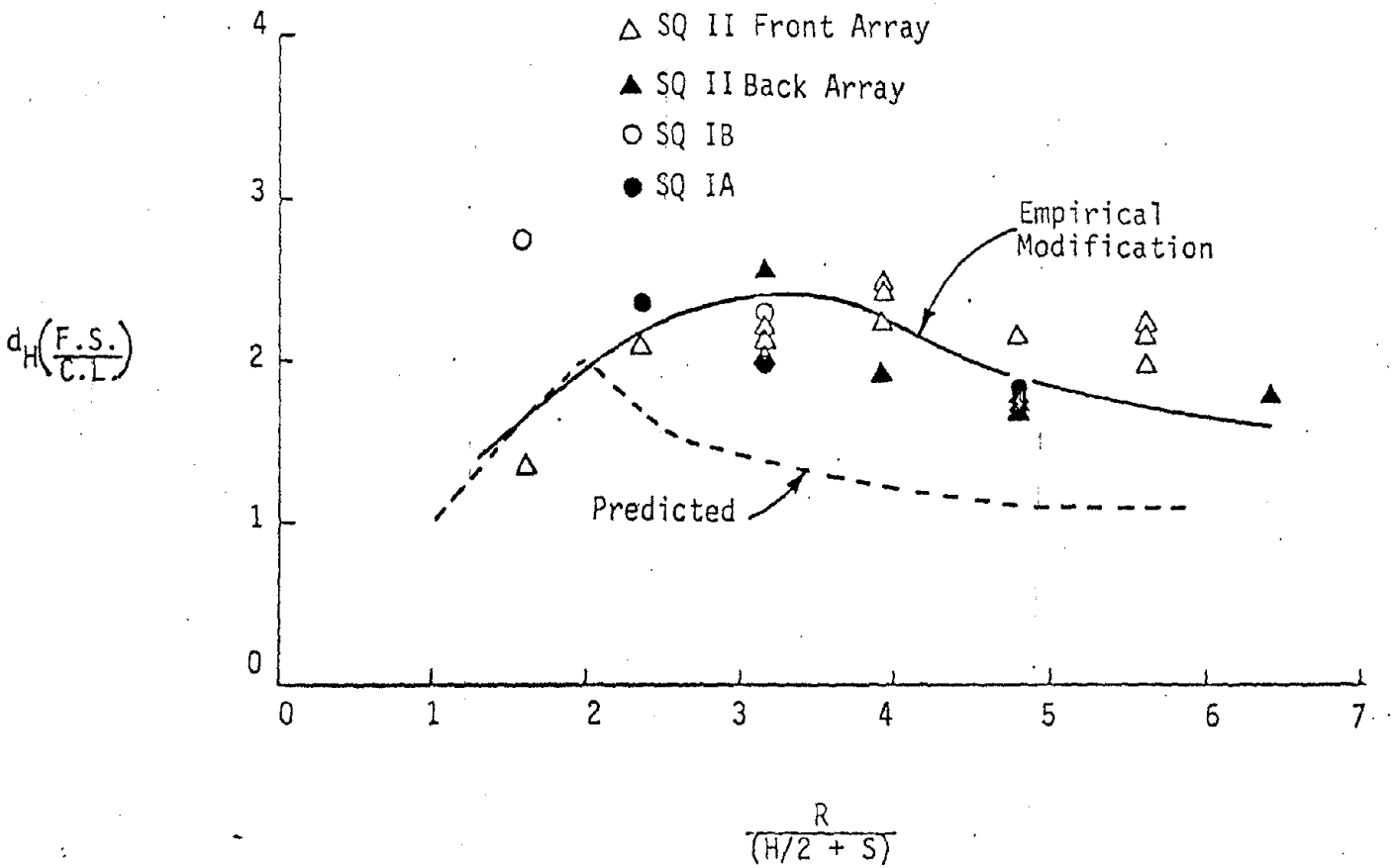

Figure 50. Ratios of measured SIMQUAKE free surface and centerline displacements compared with predictions.

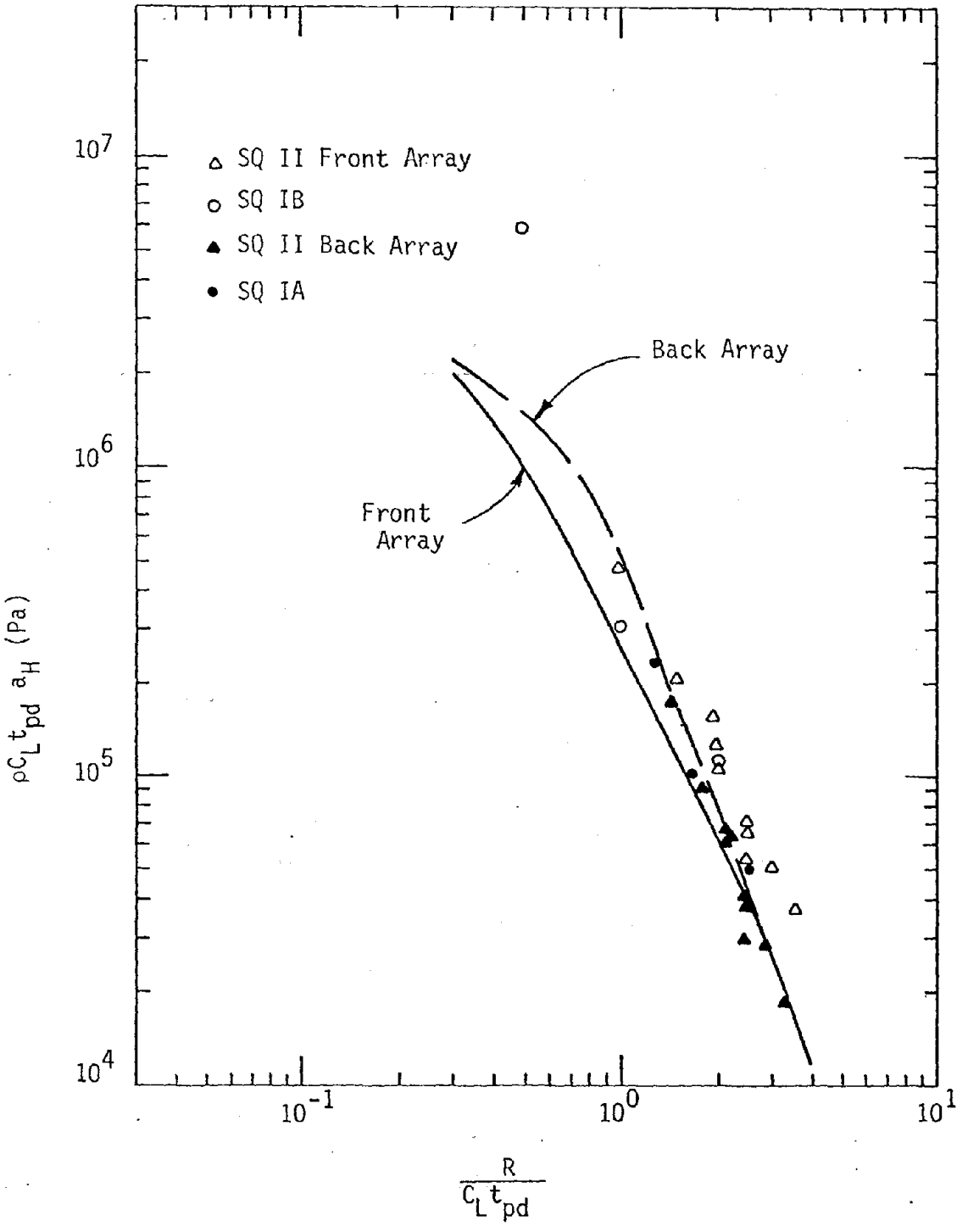

Figure 51. Measured SIMQUAKE near surface peak accelerations compared with predictions.

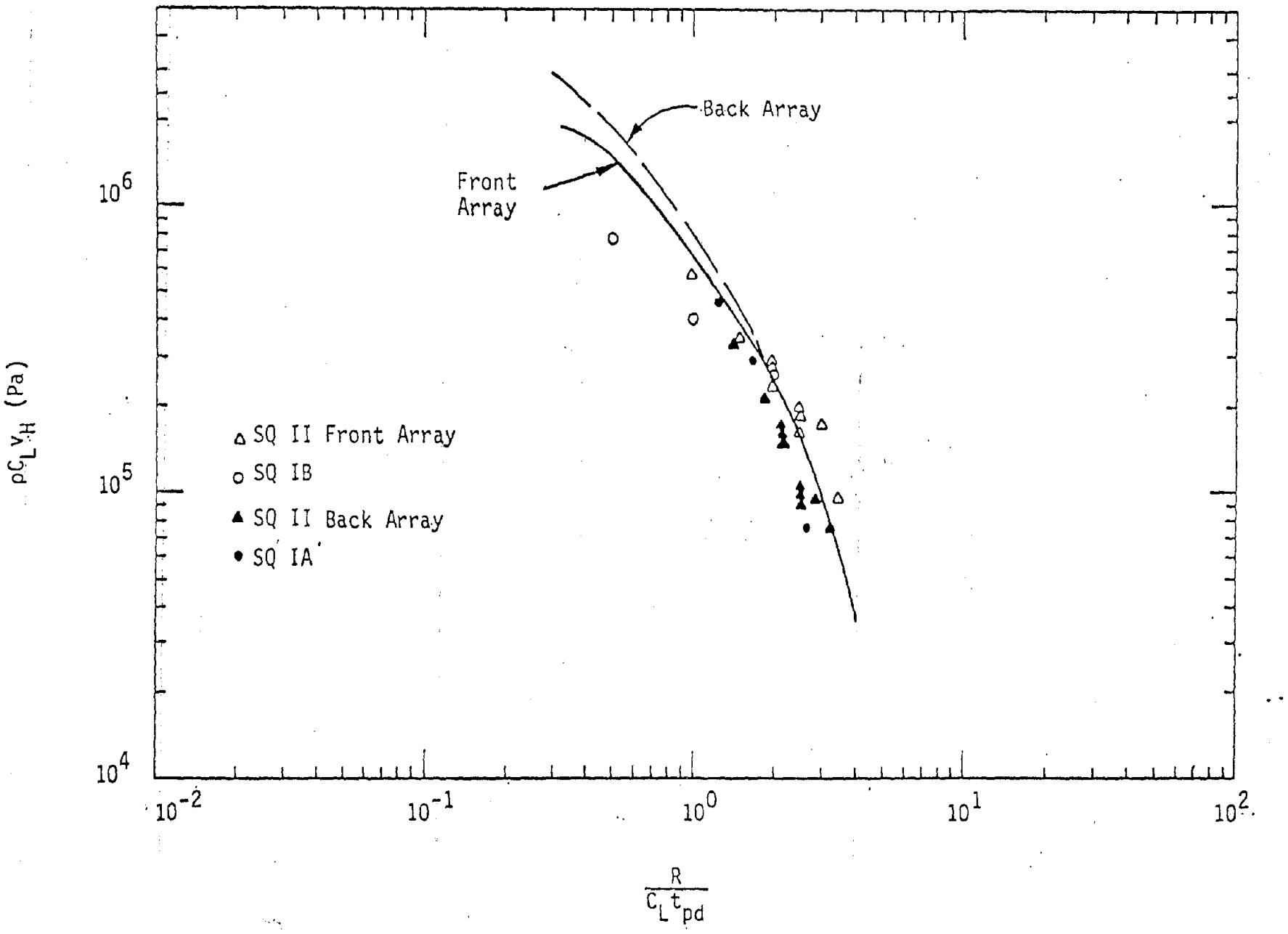

Figure 52. Measured SIMQUAKE near surface peak horizontal velocities compared with predictions.

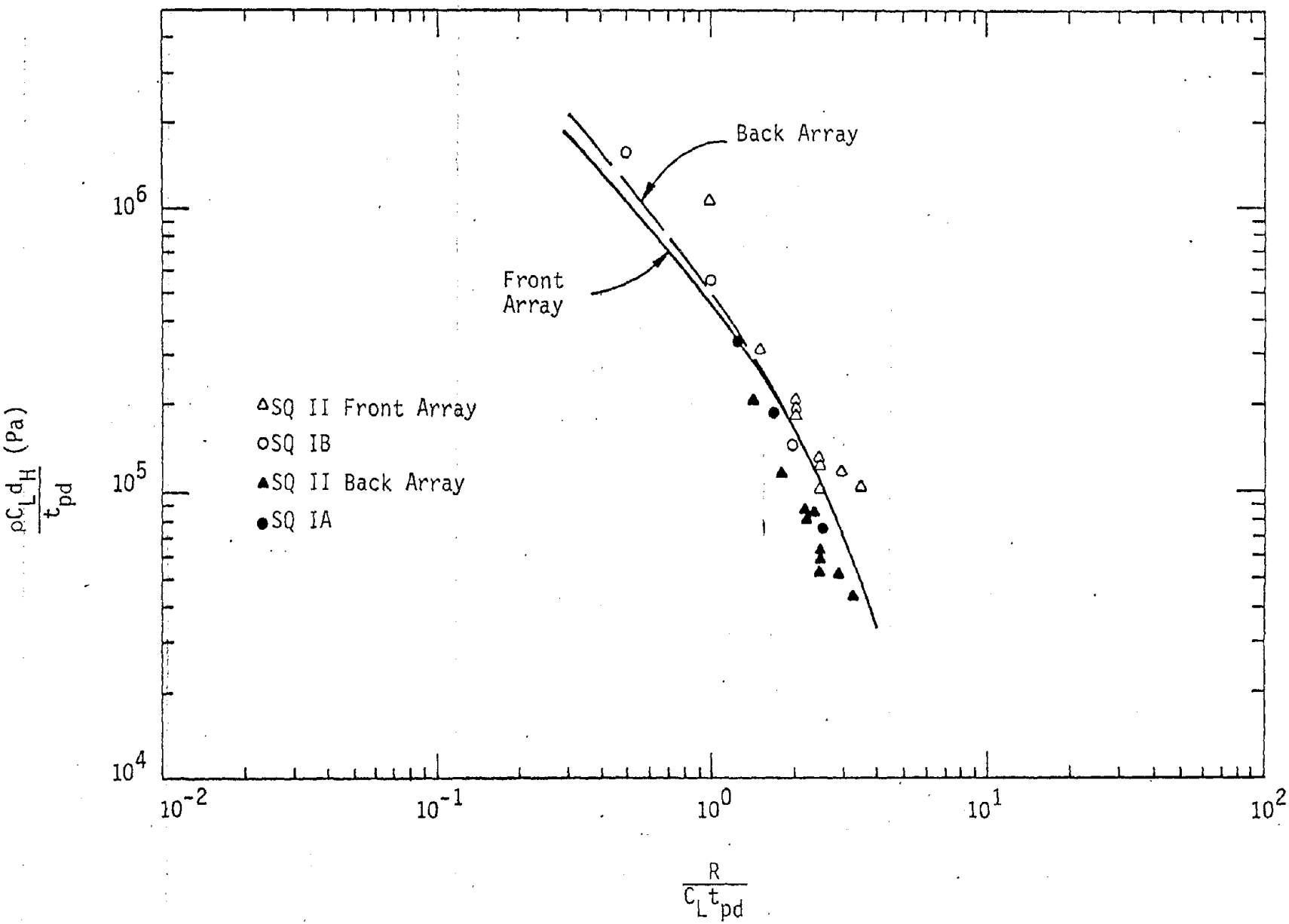

Figure 53. Measured SIMQUAKE near surface peak horizontal displacements compared with predictions.

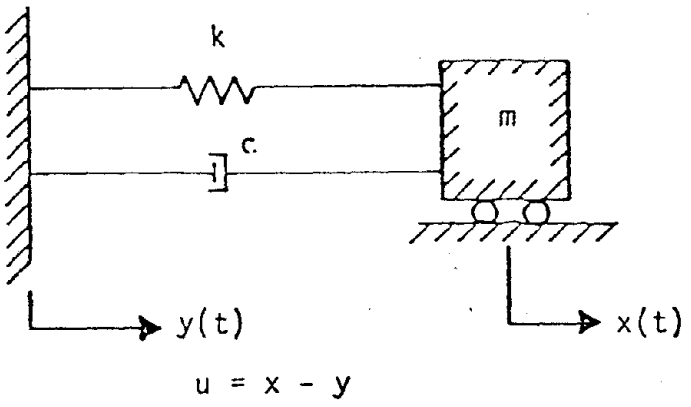

Figure 54. Single degree of freedom system subjected to base motion.

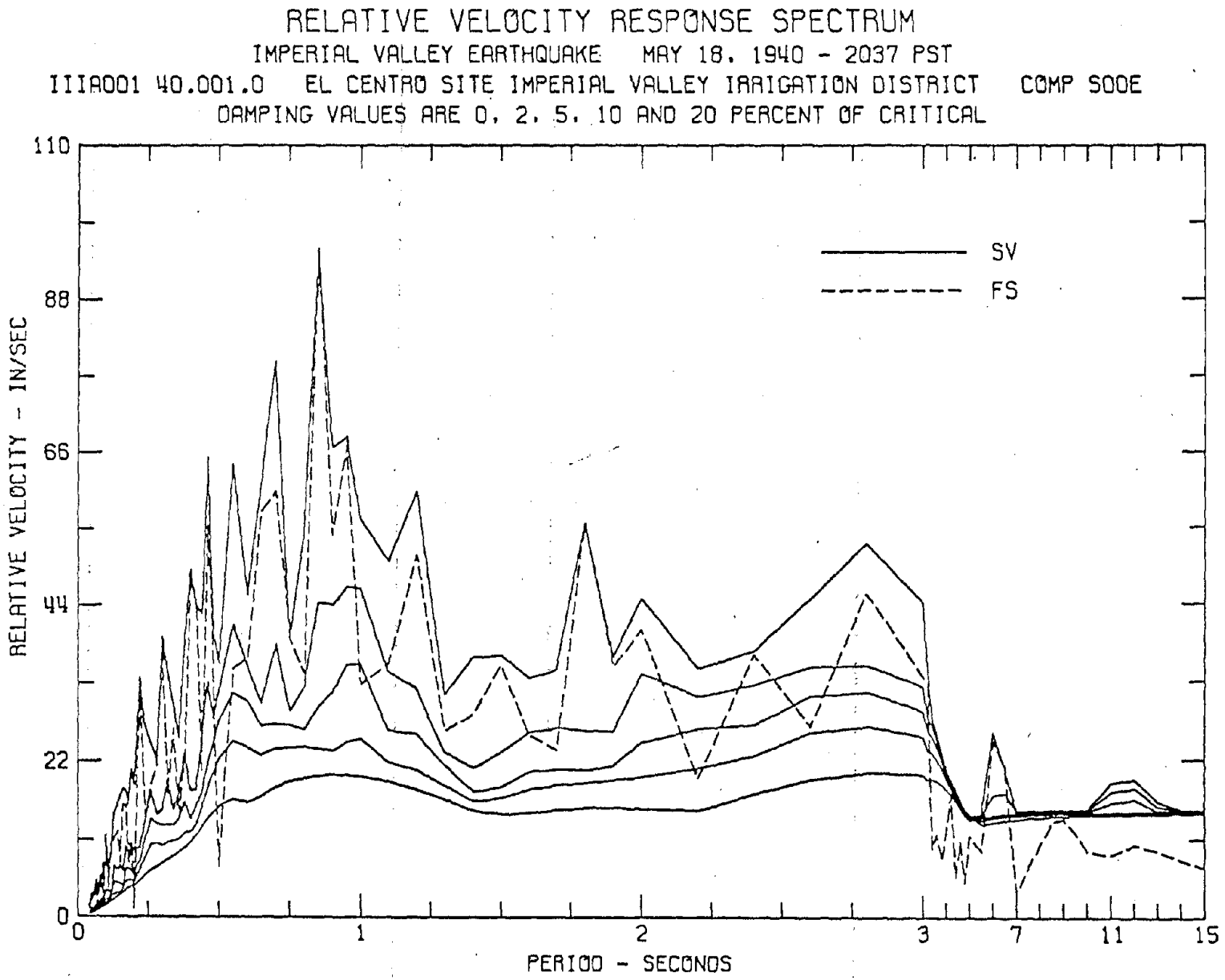

Figure 55. Example relative velocity response spectrum (ref. 24).

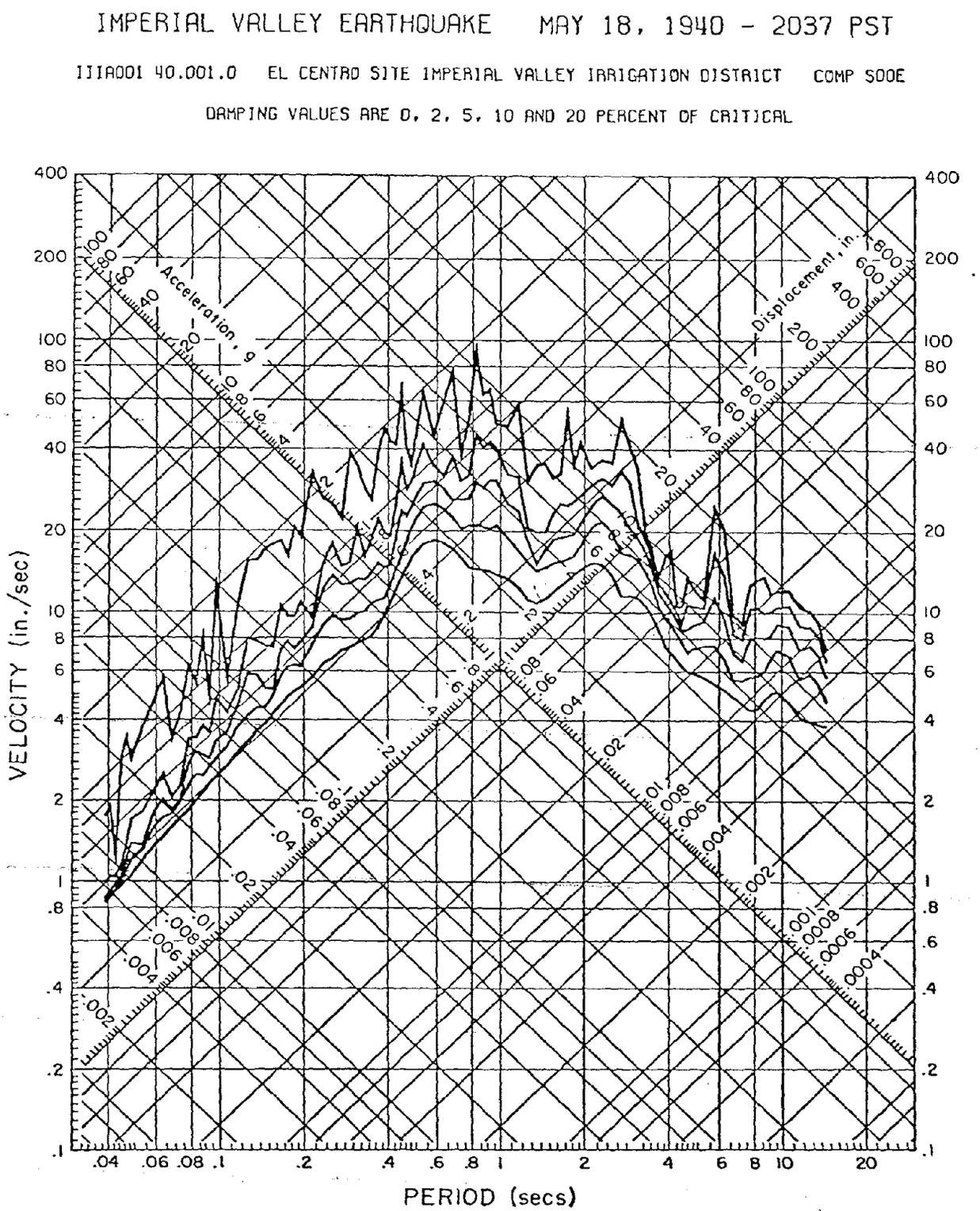

Figure 56. Example tripartite logarithmic response spectrum (ref. 24).

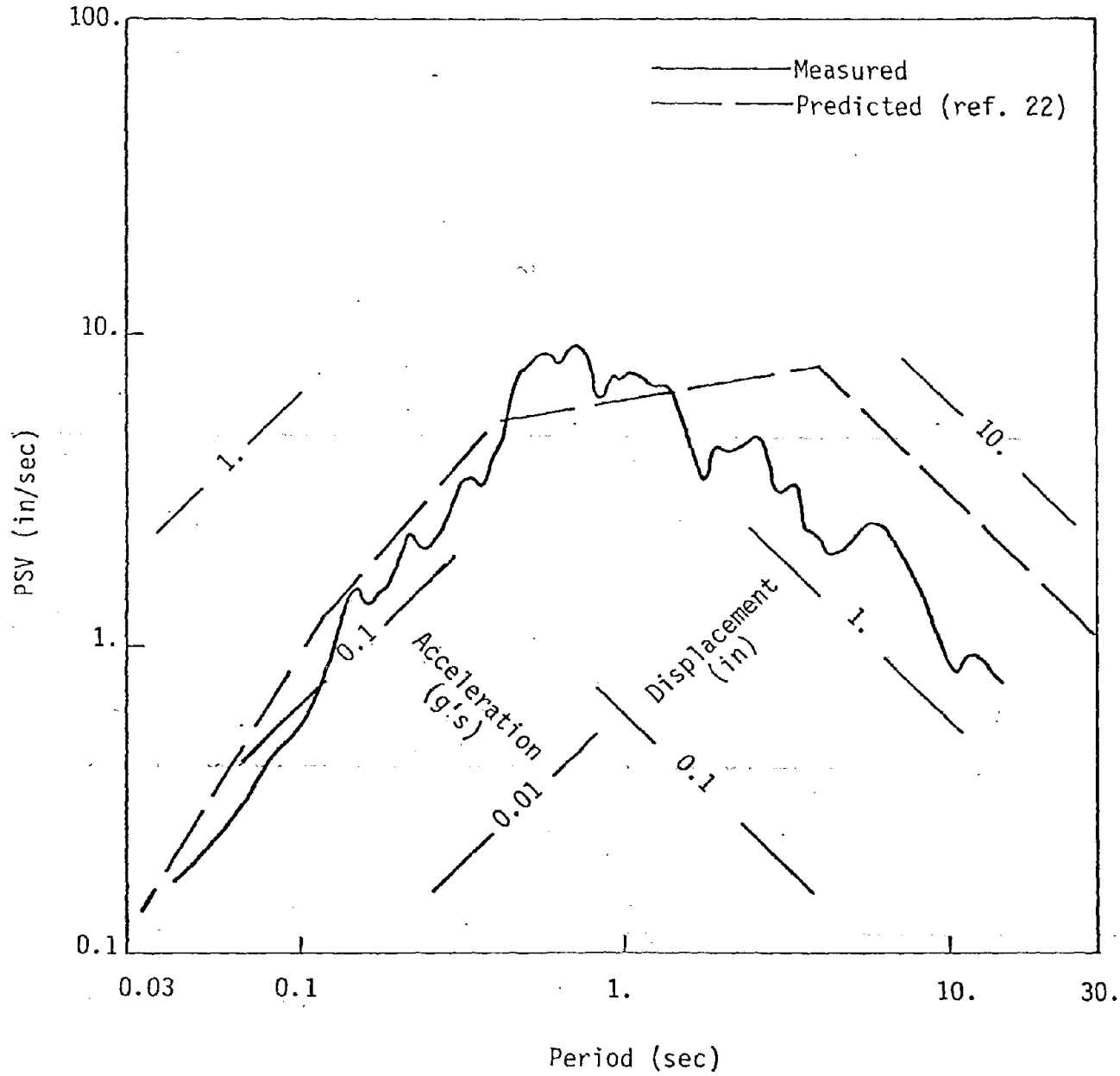

Figure 57. Comparison between response spectrum calculated for earthquake accelerogram III A018 S01W (ref. 24) and that predicted by method of reference 22.

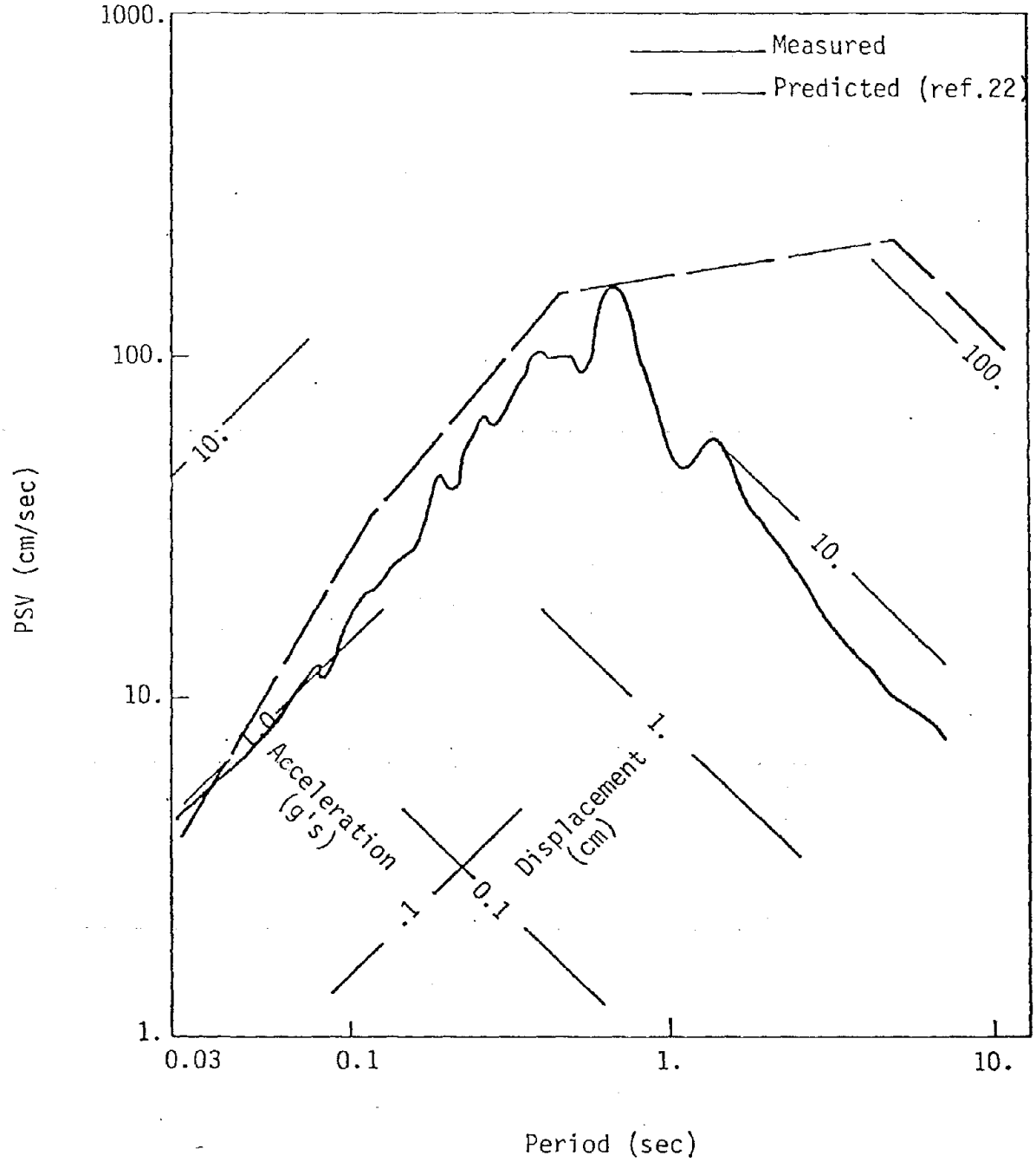

Figure 58. Comparison between response spectrum calculated for SQ II accelerometer AH38 at the 107 m range (ref. 8) and that predicted by method of reference 22.

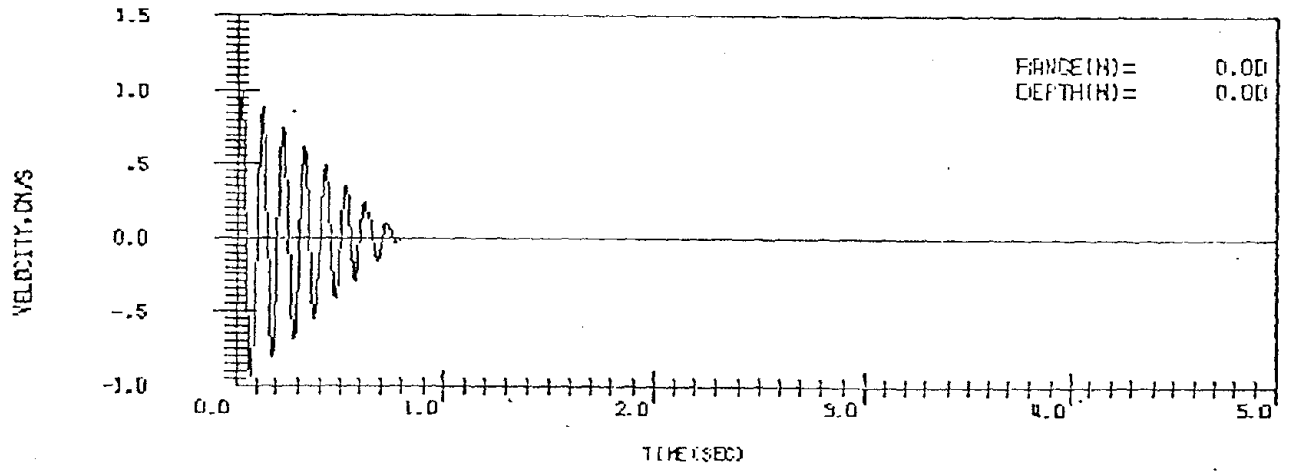

a) Linearly damped sinusoid; 8 cycles of motion.

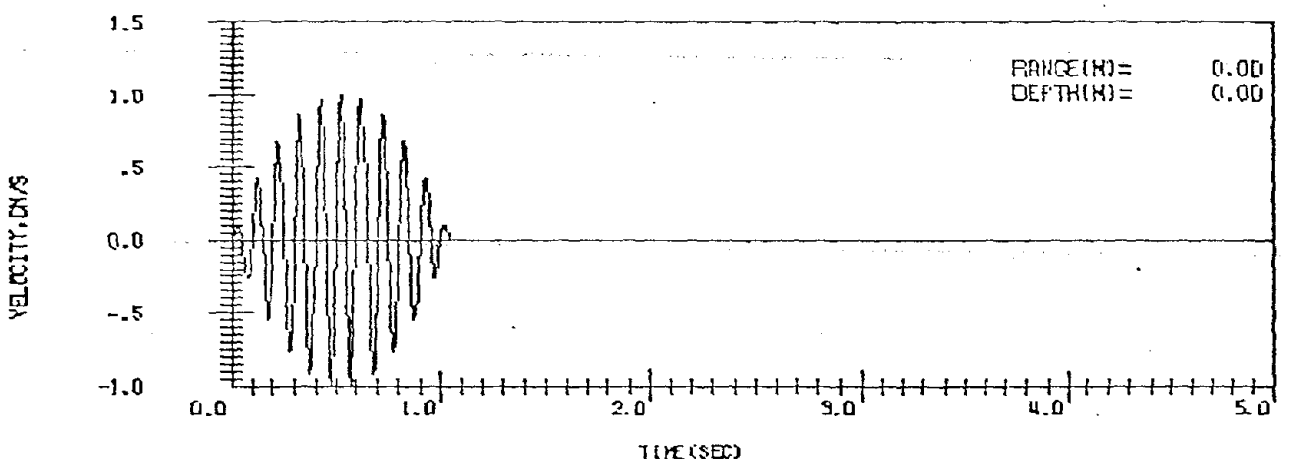

b) Parabolically modulated sinusoid; 10½ cycles of motion.

Figure 59. Response spectrum input velocity functions.

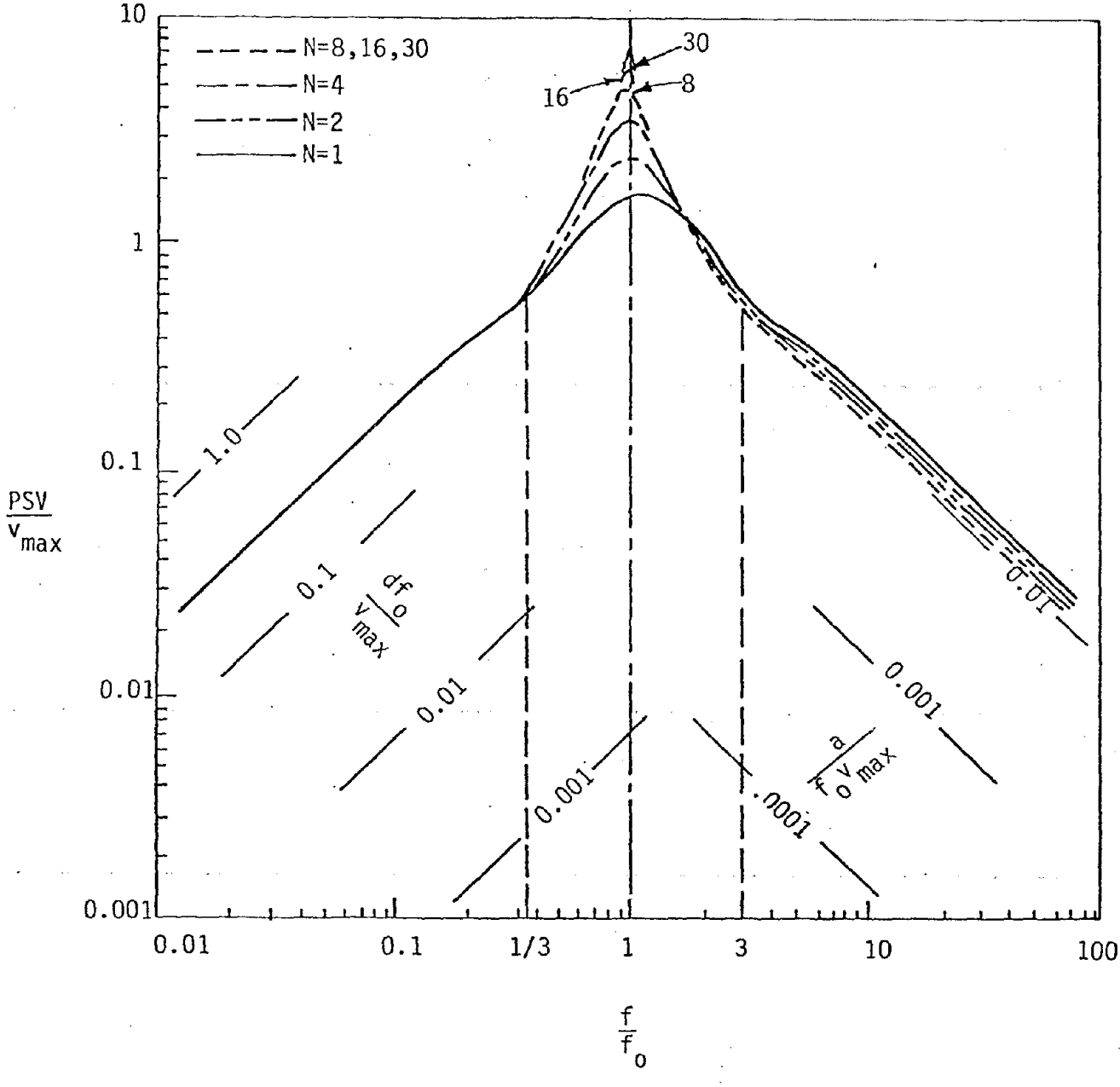

Figure 60. Normalized response spectra showing effect of number of cycles of a linearly damped sinusoid; β=5%, v_{max}=1cm/sec, f_o=10Hz.

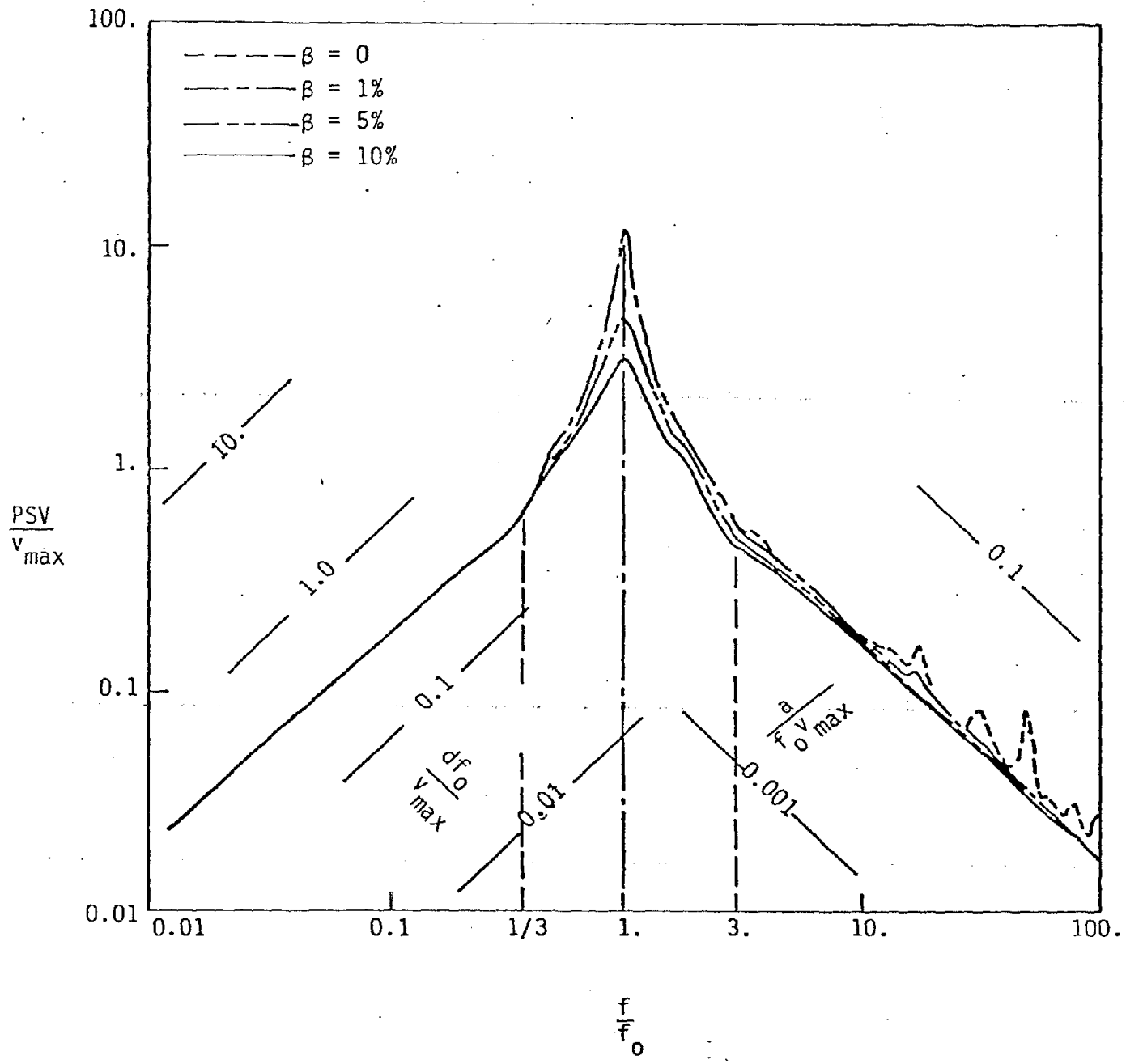

Figure 61. Normalized response spectra showing effect of damping for a linearly damped sinusoid; N=8, v_{max}=1cm/sec, f_o 10Hz.

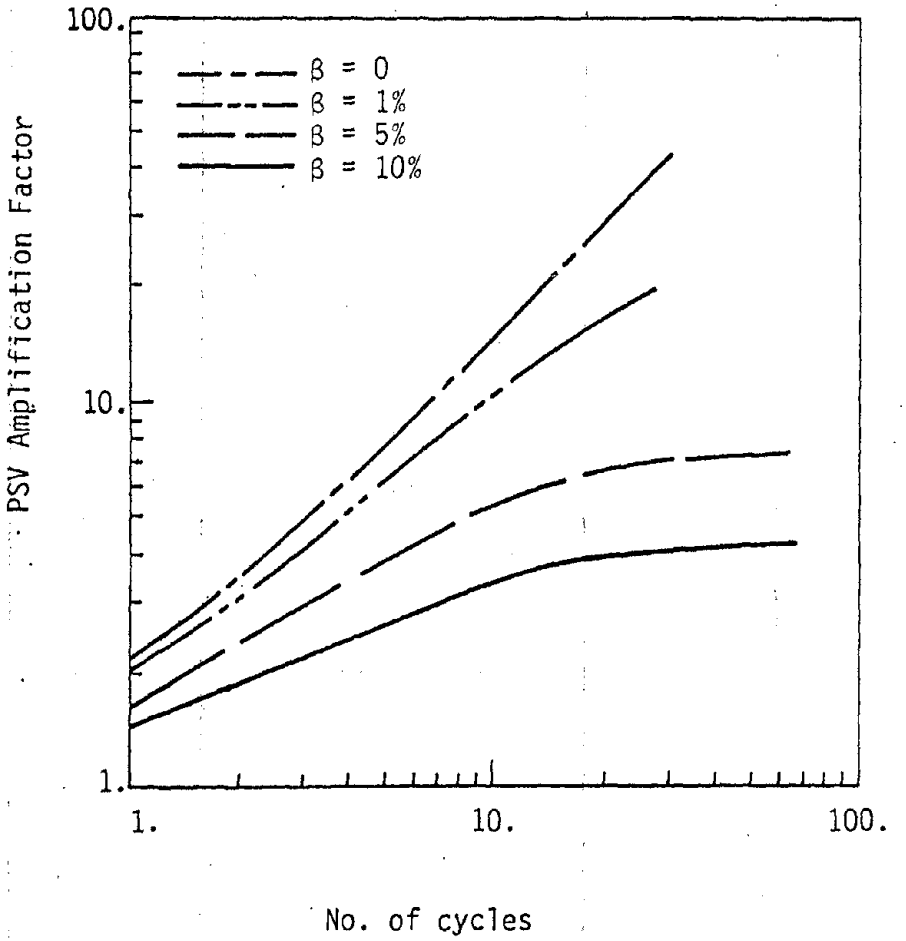

Figure 62. Pseudovelocity amplification factor as a function of damping and number of cycles of motion for linearly damped sinusoid.

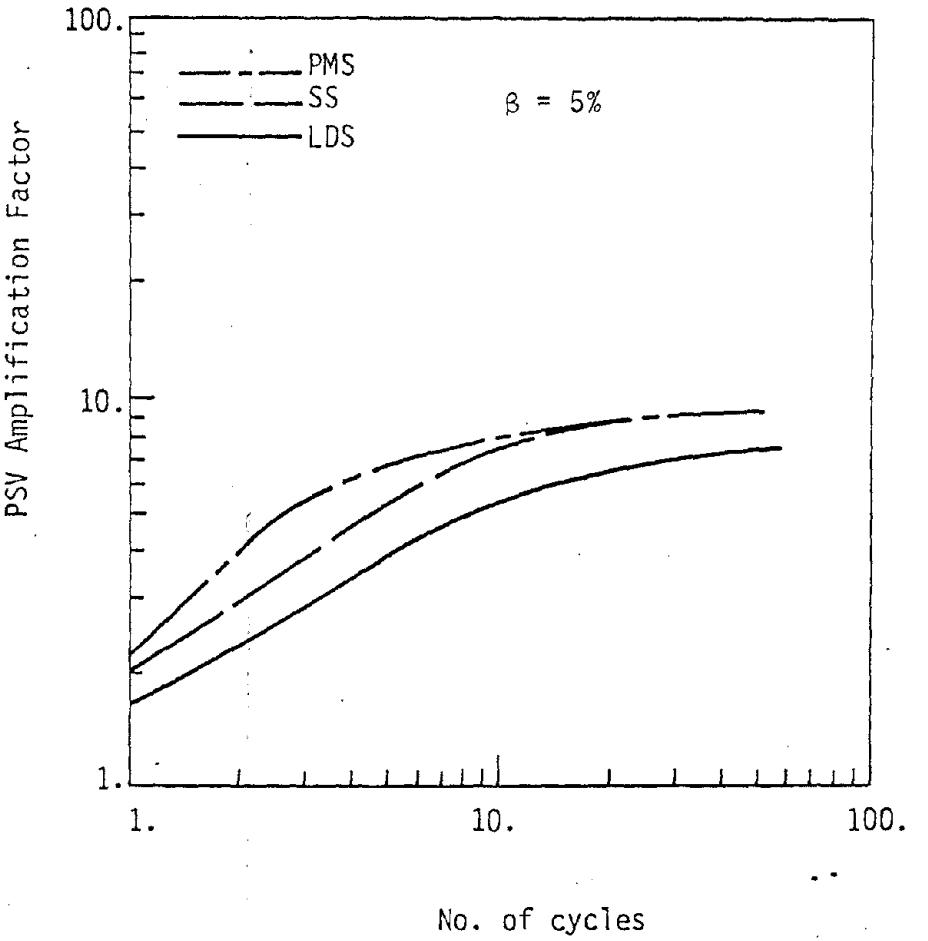

Figure 63. Pseudovelocity amplification factor for PMS, SS and LDS functions at 5% damping as a function of number of cycles of motion.

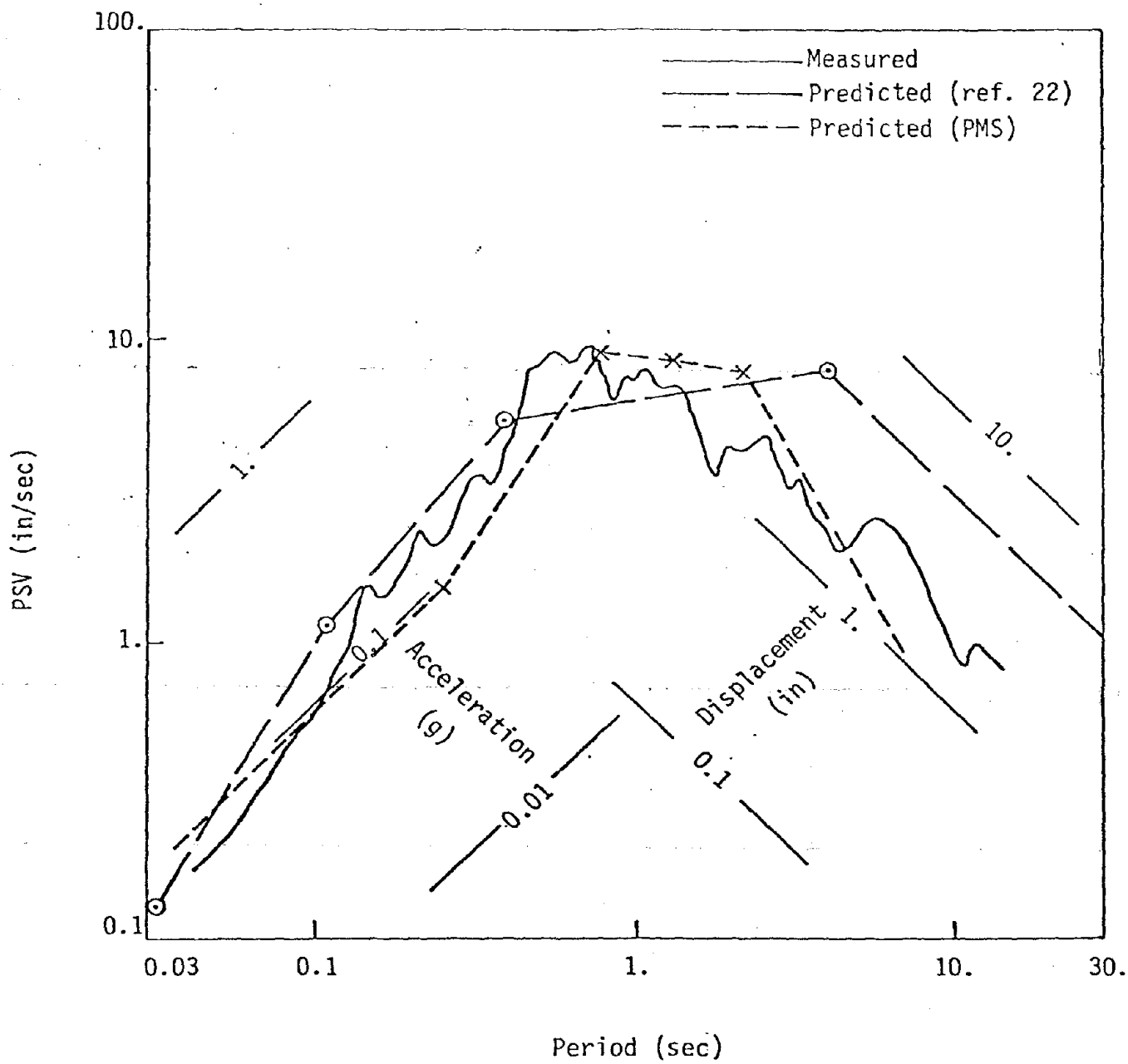

Figure 64. Comparison between response spectrum calculated for earthquake accelerogram III A018 S01W (ref. 24) and those predicted using the PMS function and the method of reference 22.

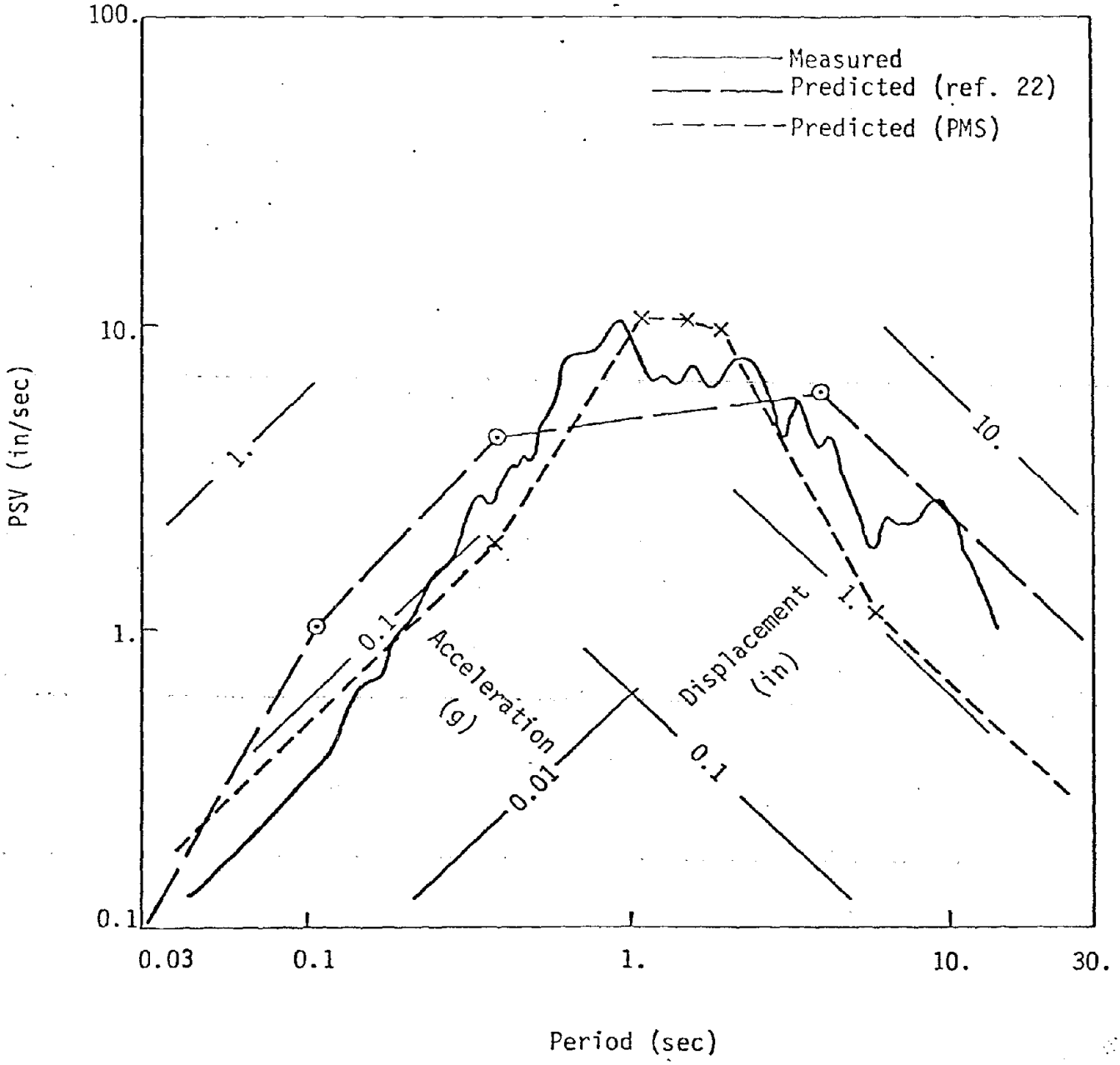

Figure 65. Comparison between response spectrum calculated for earthquake accelerogram III A003 S90W (ref. 24) and those predicted using the PMS function and the method of reference 22.

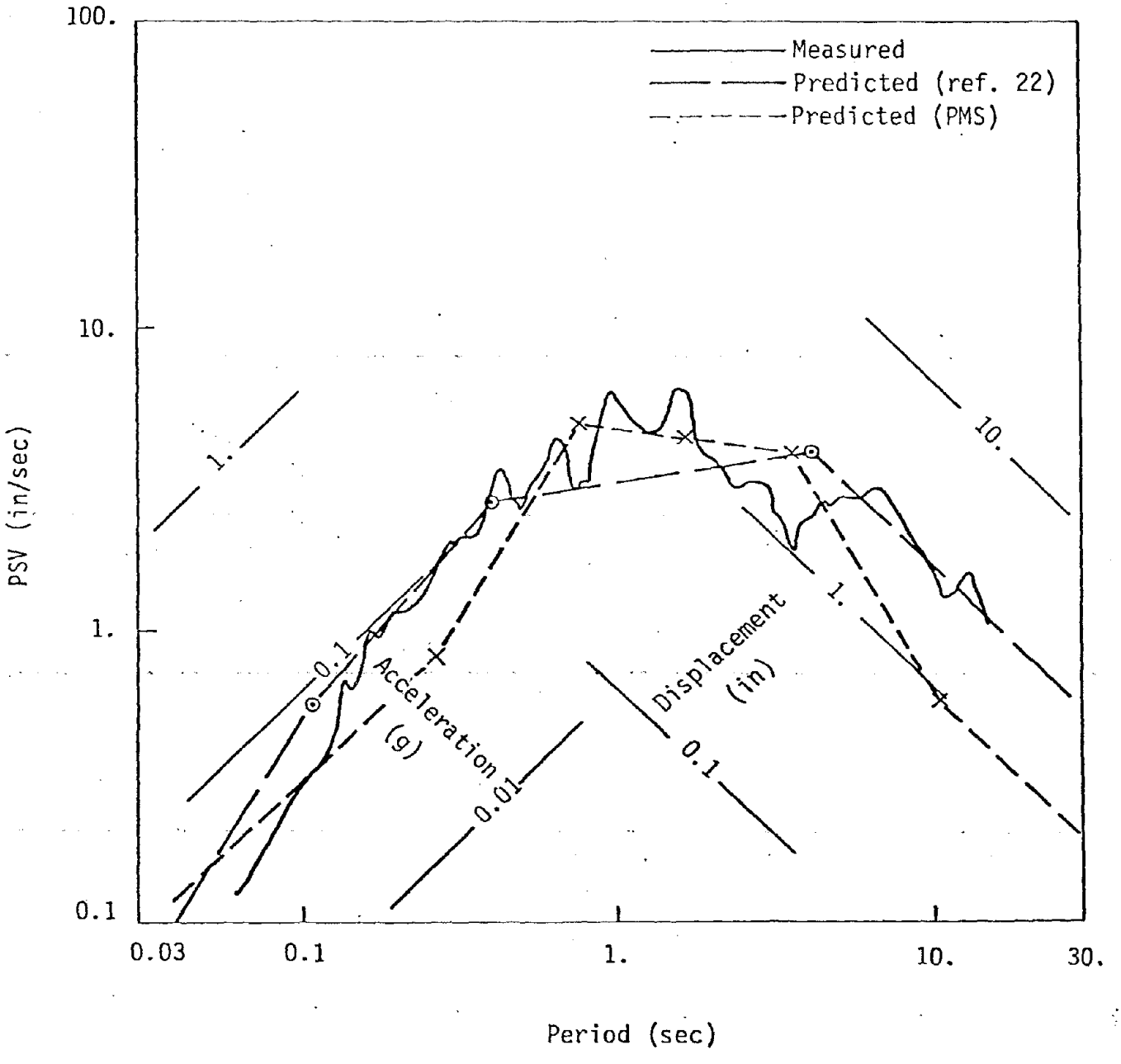

Figure 66. Comparison between response spectrum calculated from earthquake accelerogram III A011 S00W (ref. 24) and those predicted by the PMS function and the method of reference 22.

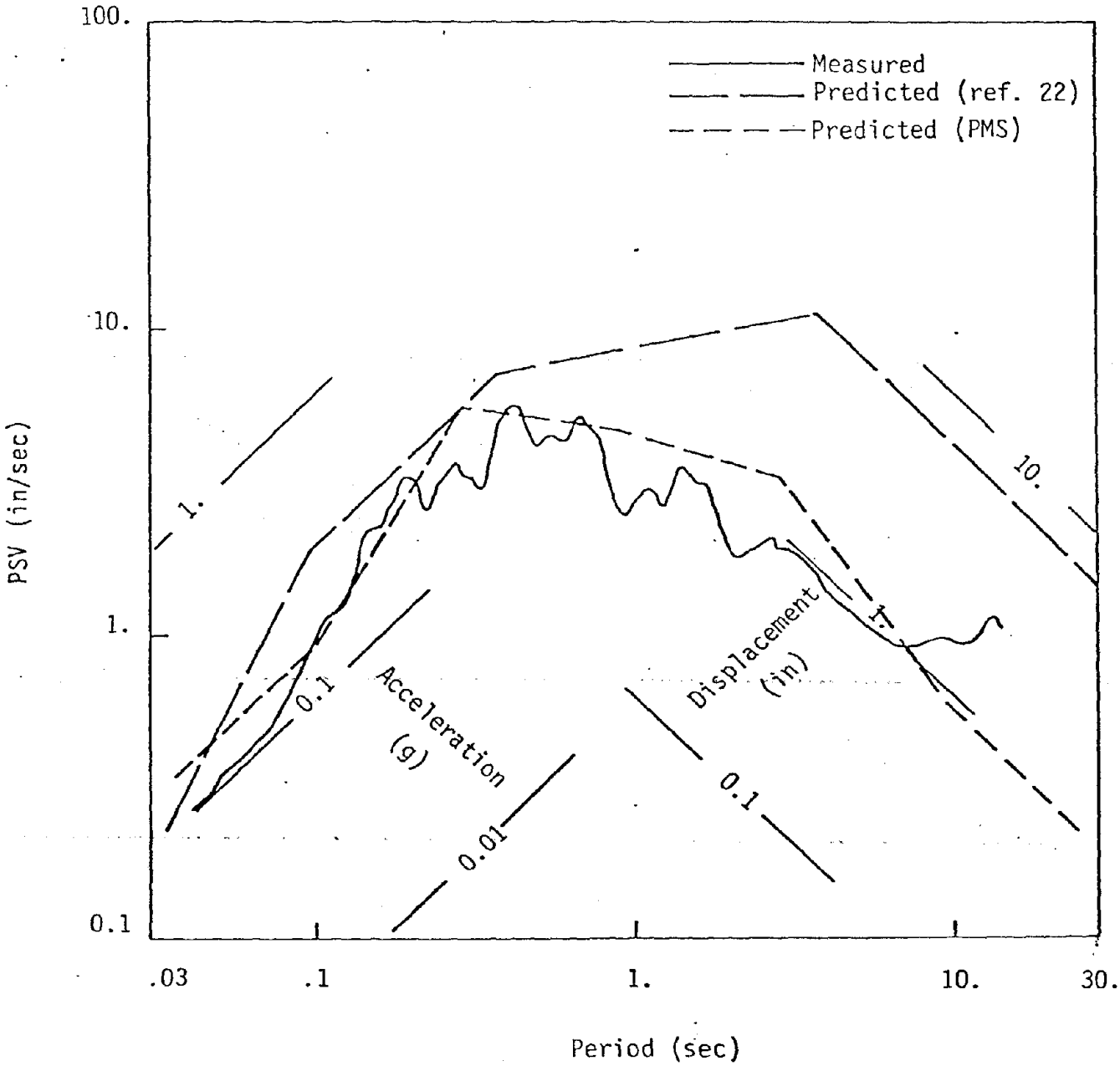

Figure 67. Comparison of response spectrum calculated for earthquake accelerogram III A002 S44W (ref. 24) and those predicted using the PMS function and the method of reference 22.

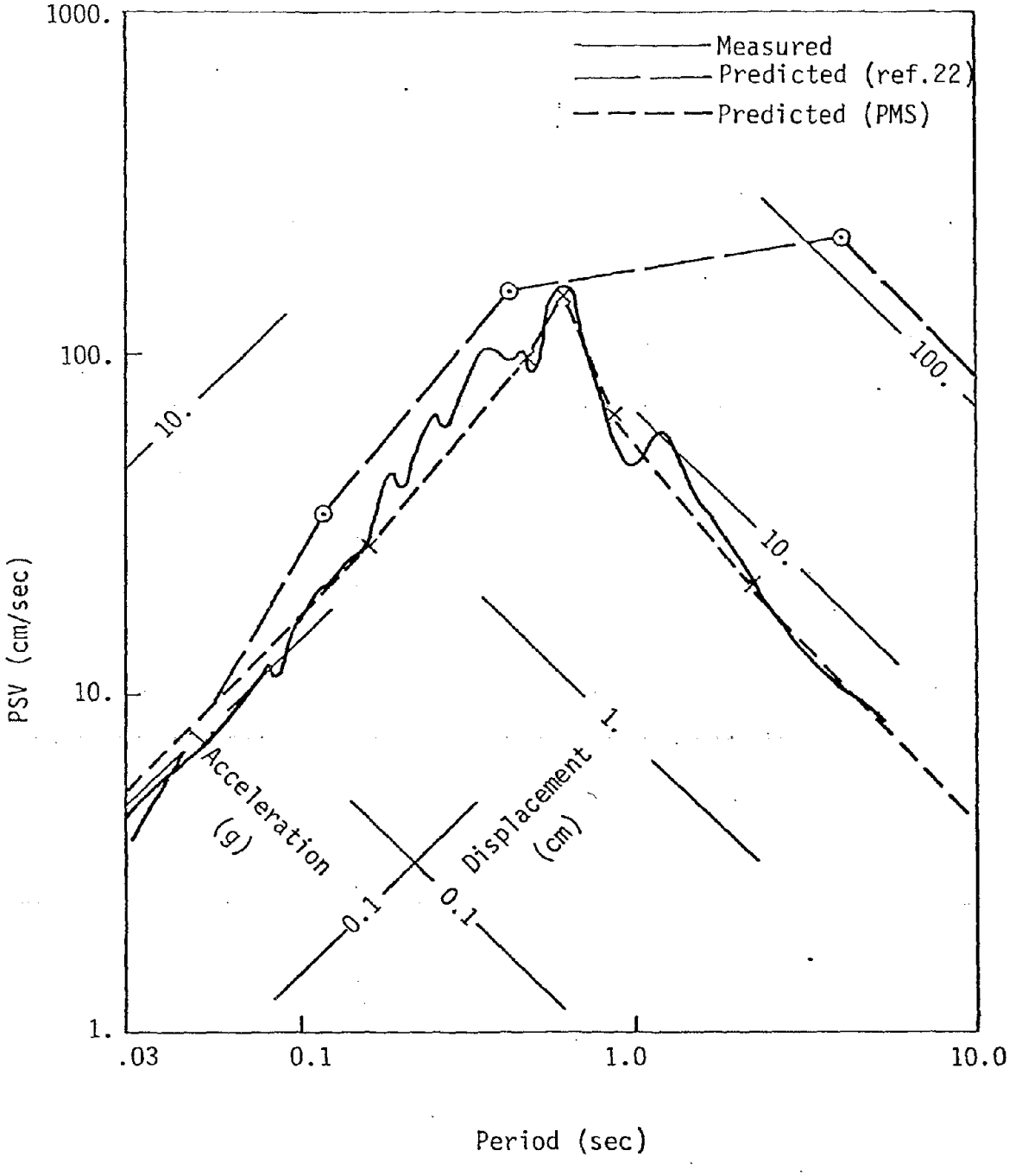

Figure 68. Comparison between response spectrum calculated for SIMQUAKE II measurement AH38, 107 m range, (ref. 8) and those predicted using the PMS function and the method of reference 22.

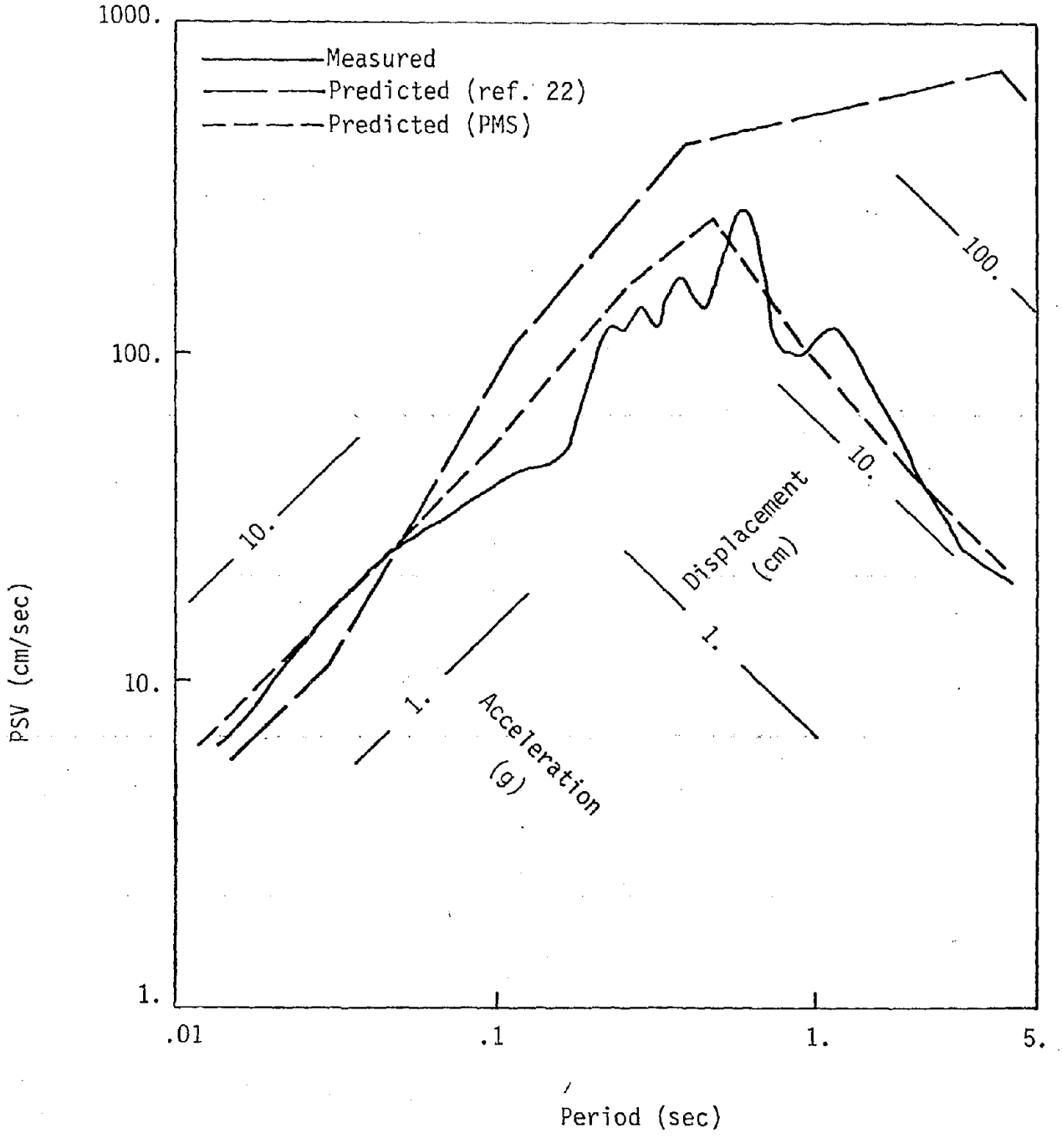

Figure 69. Comparison between response spectrum calculated for SIMQUAKE II measurement AH17, 61 m range, (ref. 8) and those predicted using the PMS function and the method of reference 22.

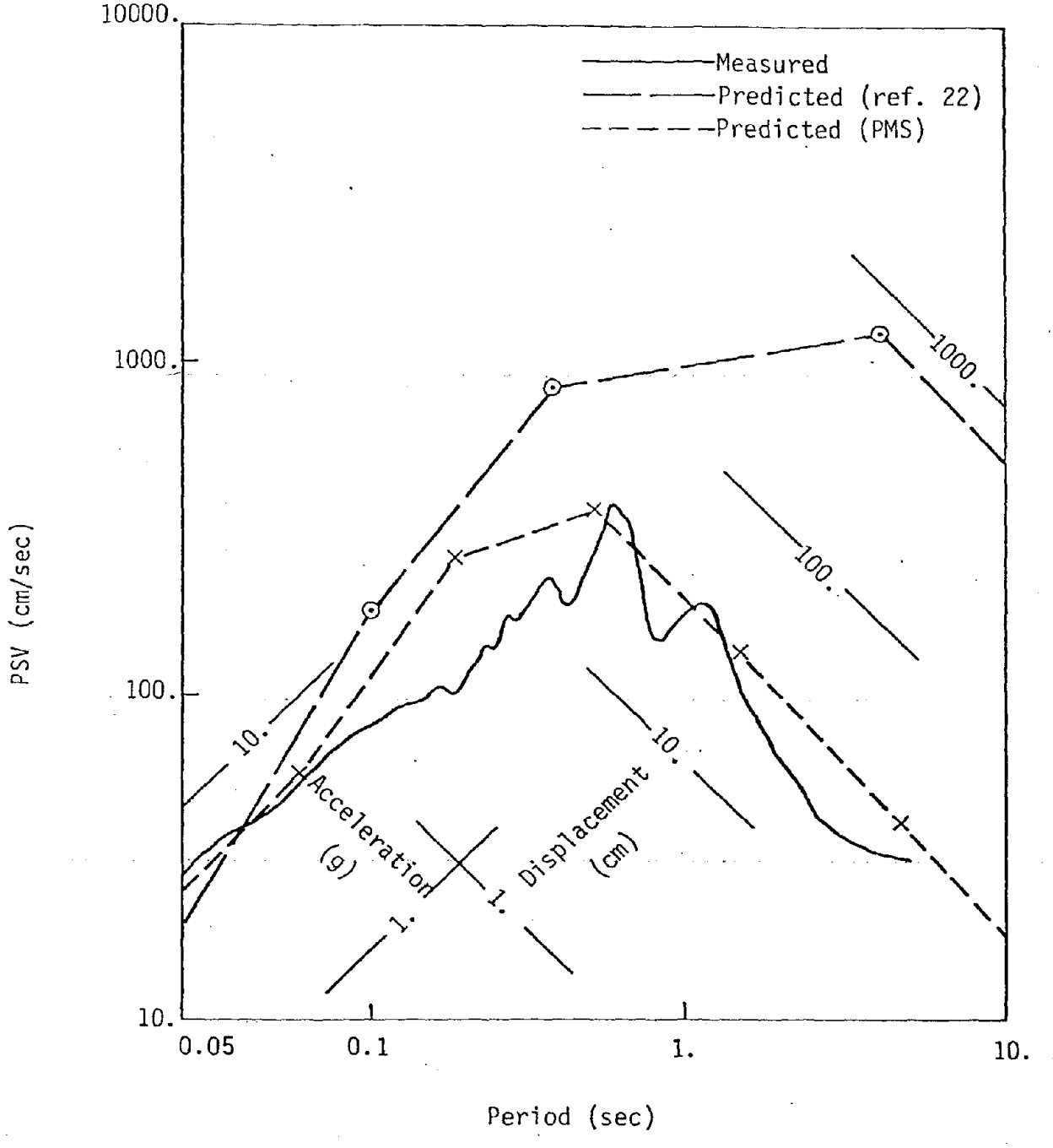

Figure 70. Comparison between response spectrum calculated for SIMQUAKE II measurement AH 05, 45.7 m range, (ref. 8) and those predicted by the PMS function and the method of reference 22.